

## **CHAPTER 4**

### **OBSERVATION, RESULT AND DISCUSSION**

It is understood that not only the process variables (rotational speed and traversing speed) are affecting the quality of weld, but few covert variables are also found playing an important role in the weld quality. The main covert variables are fixation, rigidity and machine variability. Fixation means the way in which plates (substrate) and tool being fitted and the interference introduced through the shoulder surface on the substrate. Rigidity means the compliance present due to dynamic forces generated during welding. Machine variability is the interference of machine characteristics and electrical controller in weld formation.

These factors predominantly effect the dynamic engagement of the BFSW tool with the substrate. The weld formation depends on the consequence of processes involved in grabbing and releasing the plasticized weld material, the stiffness of the mechanical system that hold the tool and the substrate and interaction of machine control system with dynamic response.

Mishra and Murray [12] showed welding force response towards clamping position which eventually impacted the weld quality. The importance of this variable was assumed to be the setup requirement in CFSW. However, the belief that the BFSW process is less stringent regarding fixation is not exactly true because the FSW process itself has factors that need to be controlled. This issue has been equally significant in CFSW and BFSW.

Tool features (or design), spindle and travel speed and its effect on weld quality have received overwhelming attention by previous researchers on CFSW as compare to BFSW. Although these factors play similar roles in both processes, the additional shoulder in BFSW and the full pin penetration create additional interactions. This is because for single shoulder tool pin, material is always available around the tool-substrate interface, but this is not the case in bobbin tools. The situation is even more acute when dealing with difficult-to-weld and thin materials. Besides that, although the

literature describes a variety of specifically designed tools, the details of the design including dimensions of the features, and the process responses have not yet been revealed, especially for BFSW and partly for CFSW.

In this context ‘Difficult-to-weld’ means that the presence of multi-parameters interactions in the process. This causes low repeatability (same process setting do not have consistent quality of weld), production of high variability of weld formation (weld quality changes within one run) and sensitivity to situational variables (covert variables that the users are not aware of). For the particular material under consideration AA6082-T6 there are additional welding difficulties due to low ductility compared to other aluminium alloys. This is not the case in AA6101 alloy due to higher ductility in the series. Other factors that contribute to welding problems are variability in hardness, inconsistency in thickness and surface finish.

In case of BFSW, interesting examples were found in Liu, et al. [141] who used featureless assembled tool (to weld 4mm thick AA6061-T6), while Colligan, et al. [142] implemented tool with loaded features (to weld 5mm thick Al 5083-H116) to achieve good weld. That welds could be achieved with such variety of tool features suggests that other variable, which identified above, are acting as covert variables.

The following are the illustrations on findings in this research project.

#### **4.1 CLAMPING OF SUBSTRATE**

In addition to a requirement of strong clamping, a rigid structure of the fixture is essential [68][142]. However, literature that quantifies the effect size of this factor is rare for friction stir welding in general and BFSW in particular. Although researchers [12][143][144] have shown the importance of fixture, this was in the CFSW realm where this is self-evident, and even then the overall rigidity of the welding apparatus was not explicitly considered. The present work sought to determine the fixation and rigidity requirements more explicitly.

Two totally different FSW processes were under the consideration namely CFSW and BFSW, one having single shoulder and the other having double shoulder tool for joining Al plates. The researcher developed two different clamping devices to provide clamping and rigidity to the substrate to be joined.

#### **4.1.1 Fixture for CFSW**

Initially the clamping of plates was done using workshop milling vice. In this case it was observed that the plates were lifted up due to compressive force applied on side. Then as per guideline narrated by TWI, UK, it was thought to design a special fixture for the experiment to be carried out. Many researchers used workshop equipment and clamping devices to clamp the plates. Since ever, there was no such design available for clamping the substrate; it was started with fundamental thinking about the clamping mechanism to fulfill the requirements. Different considerations were laid down to overcome limitations that were experienced during the development of fixture.

##### **4.1.1.1 Fixture with top clamping:**

The first fixture developed had clamping arrangement from the top. The problem of lifting of plates at center is now resolved due to pressure applied from top of the plates. But during welding and tool traversing another problem was observed. It was the horizontal shifting (displacement) of plates apart in butt region, which result in improper bonding. So the fixture modification was demanded.

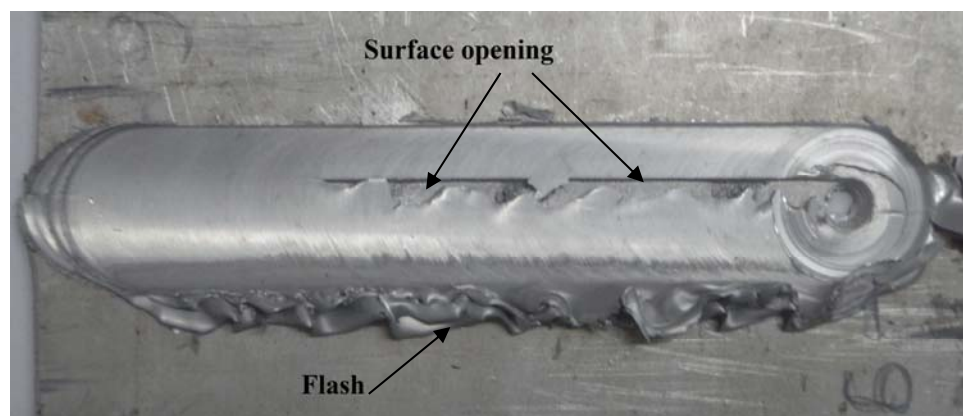


Fig 4.1: Sample welded with first fixture

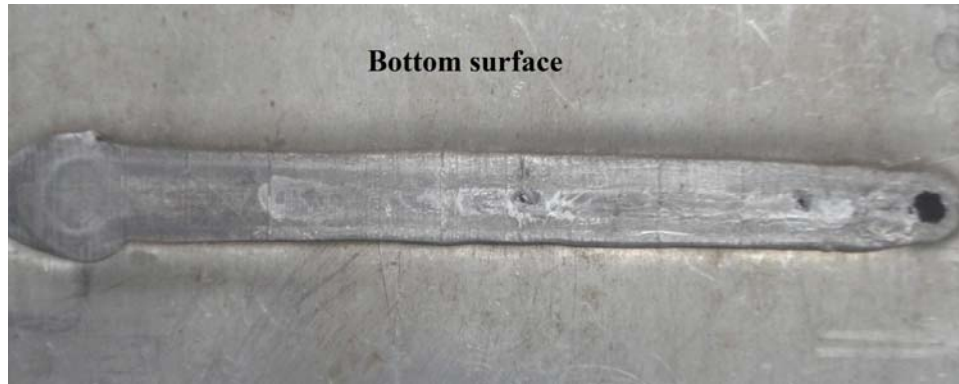


Figure 4.2: Bottom surface of the plates welded

Figure 4.1 and 4.2 show the visual inspection of the plates at the welding stage. It can be seen that most of the welds have noticeable grooves and smear (thin wisps) of flash. In addition, some plates have incomplete joint characteristics. A different observation was made in case of AA6101 alloy that it stick to the backing plate, resulting in tunnel beneath the bottom surface and also incomplete welding.

In the figure 4.1 and 4.2, the surface in the beginning of weld is very fine but after certain length of welding it shows surface opening or cutting. This is due to variations in the shoulder penetration in the substrate, resulted in defective surface.

#### **4.1.1.2 Fixture with top and side clamping:**

The second development was having clamping pressure applied from top and side both to overcome substrate displacement. This design was good enough at first instance, but again we found a typical drawback in this design. There was a sliding of plates during tool traversing along the weld line. This again resulted in poor welding.

#### **4.1.1.3 Jig type Fixture with flexible clamping:**

This time utmost care was taken and the fixture was designed such that, not only will it take care of plate sliding but also an additional provision was made to adjust the gap in the butted region of plates to be joined. A jig type fixture was developed which could facilitate easy loading and unloading of plates, saving the time of clamping. The fixture design was based on the principles of degrees of freedom followed in JIG design. The

fixture also has flexibility of clamping plates having different thickness. Referring the literature, the gap between the plates in butt region is tolerable up to 10% of thickness. So this gap should be controlled and in future it may be considered as one of the variable parameter defining weld quality.



AA 6101 T6 alloy



AA 6082 T6 alloy

Figure 4.3: Plates welded with new jig type fixture

This Jig type fixture assumed to be advantageous and used in this research work for CFSW. The figure 4.3 shows the surface quality of the sample welded using new jig type fixture.

#### **4.1.1.4 Material for fixture:**

The material having least heat transfer and high hardness was selected in manufacture of the fixture. Two materials were suggested for the application (i) high carbon steel and (ii) ferrite steel. Both the materials gave good results and served as backing plate sufficiently strong to resist the welding pressure, and also suitable to provide maximum heat for welding.

#### 4.1.2 Fixture for BFSW

CFSW has the detriment of requiring a strong clamping fixture, to resist both the parting force and plunge force. This requirement can be reduced when adopting the BFSW process as the plunge force is absent [26]. However, the reduction of the clamping requirement should not be taken for granted.

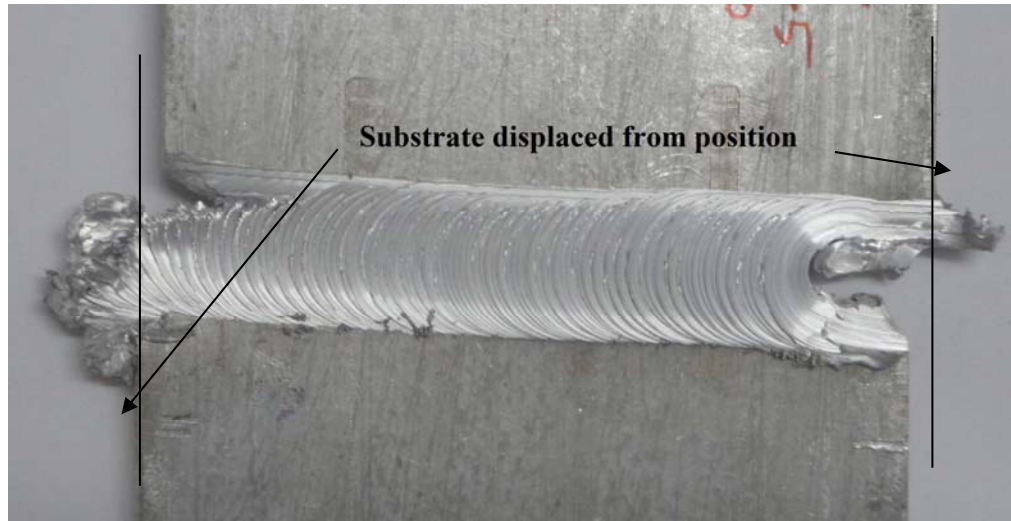


Figure 4.4: Welding of plates using workshop clamping

In the beginning a trial was taken using workshop clamps to hold the substrate for welding with bobbin tool. It was observed that there is a linear displacement of substrate in opposite direction; as seen in figure 4.4

From the above trial and experience gained from CFSW, a fixture need was felt in BFSW also and the author did not want to work without it. Hence a new fixture was devised considering the requirements laid down while developing the fixture for CFSW.

In this fixture also the movement was arrested sideways, sliding and vertical. The two horizontal movements were restricted by the supporting base and vertical lifting movement was arrested by top clamping. Sufficient space was kept below the substrate for easy movement of second shoulder beneath the plates. The fixture (figure 4.5) so designed is capable of accommodating different thickness; which saves the time and cost to develop separate fixture with change in substrate thickness for different experiments.

The fixture is also capable of gap setting so the further research on gap between the abutting regions can be considered as one of the variable parameter affecting the quality of weld.

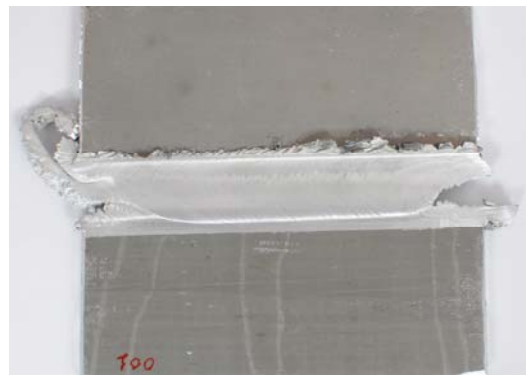


Figure 4.5: Fixture for bobbin friction stir welding (BFSW fixture)

The material used in manufacturing of fixture was carbon steel, which resulted into comfortable and convenient clamping in adapting BFSW process.



(a) Image of BFSW Top



(b) Image of BFSW Bottom

Figure 4.6: Image of sample welded with convex shoulder square pin bobbin tool with new BFSW fixture

The fixture developed for BFSW is found to be very useful tool for clamping the plates. Figure 4.6 Shows a sample welded with new BFSW fixture. The surface appearance is good. No internal flaws were found in this sample when tested for microstructure.

## **4.2 EFFECT OF PROCESS PARAMETERS (SPINDLE SPEED AND TRAVEL SPEED) ON WELD**

The spindle speed and feed (travel speed) provides the heat input for the FSW. Rotational speed directly affects the heat input through frictional mechanism, and the traversing speed provides the opposite effect via pressure mechanism. Both process parameters have significant effect on the mechanical properties of the welds. Zang and Zang [131] stated that heat generation and stirring effect will be improved by increasing tool rotational speed and decreasing traversing speed. However it is observed that at higher spindle rotation flash can be seen, which ultimately result into material swept from the weld region that means loss of material from the weld. In FSW there is no opportunity to add material just like filler material possible to be added in conventional welding processes. Any material ejected from FSW weld in the form of either flash, ribbon, skin, or chips means there is a net loss and converted into defects.

The optimization between spindle and travel speed and its effect on weld properties has been one of the major questions in CFSW. Some of the examples of this vast body of work can be found in the references [27][31][34][73][77][145][146]. However, despite the vast efforts that have been done in this area, the parameters used are diverse and still not established with confidence, even for CFSW and especially BFSW.

For both CFSW and BFSW the literature shows a diversity of process parameter settings, even in the same group of materials and same thickness. For example, to weld 6056 Al alloy 500-800 rpm and 40-56 mm/min has been used [146] and for welding 6082 Aluminium 1500 rpm at 115 mm/min [31]. These are very different settings and indicate the difficulties. The defects are dependent on the process settings which are affected by the heat input and material flow [77][147].

Previous works carried out by researchers in BFSW that included the variation of process parameters are found in [29][71][148]. In case of BFSW also, a wide range of spindle and welding speeds have been used to know the effect on weld [68][141][142]. Diversity in parameters and poor repeatability indicates that the travel and spindle speeds are on the only variables universally applicable, but they are specific to the situation and other covert situational variables are also applicable.

#### 4.2.1 Tensile test

##### 4.2.1.1 Tensile test of AA 6101 T6 using hexagonal pin tool

The tensile test of welded specimen was carried out on tensile testing machine according to ASTM-E8M04. The test results are shown in Table 4.1.

Table 4.1: Tensile test result of samples welded by CFSW

Experiment No	Tool rotation speed rpm	Welding speed mm/min	UTS MPa	% Elongation	Micro hardness (BHN) at Weld Centre
E1 A	545	50	88	10.92	47
E1	545	50	132	11.32	38
E2	545	78	130	24.24	39
E3	545	120	108	17.60	43
E4	765	50	139	12.08	44
E5	765	78	129	11.20	44
E6	765	120	144	21.88	43
E7	1070	50	109	17.40	47
E8	1070	78	108	11.32	42
E9	1070	120	123	13.60	43



Figure 4.7: The Tensile test specimen after test - welded by hexagonal tool pin profile

#### 4.2.1.2 Tensile test of AA 6101 T6 using square pin tool

The tensile test of welded specimen was carried out on tensile testing machine according to ASTM-E8M04. The test results are shown in Table 4.2.

Table 4.2: Tensile test result of samples welded by CFSW

Experiment No	Tool rotation speed rpm	Welding speed mm/min	UTS MPa	% Elongation	Micro hardness (BHN) at Weld Centre
E10	545	78	120	20.16	41
E11	765	78	125	25.56	50
E12	1070	78	128	20.84	42



Figure 4.8: The Tensile test specimen after test - welded by square tool pin profile

## 4.2.2 Face Bend Test of CFSW Samples

### 4.2.2.1 Face bend test for hexagonal pin and concave shoulder

The face bend test was carried out for all the samples welded by hexagonal pin and concave shoulder tool (Table 4.3). As seen from Figure 4.9, there were no openings or cracks observed after the test. The result was satisfactory.

Table 4.3: Result for Face Bend Test

Test parameters	E1	E2	E3	E4	E5	E6	E7	E8	E9
Bending diameter mm	4(T) - 24								
Bending angle	180 °								
Observations	No opening or cracks observed								
Result	Satisfactory as per ASME section IX								



a



b

Figure 4.9: Face Bend test specimen welded by hexagonal tool pin profile after Testing.

#### 4.2.2.2 Face bend test for square pin and flat shoulder

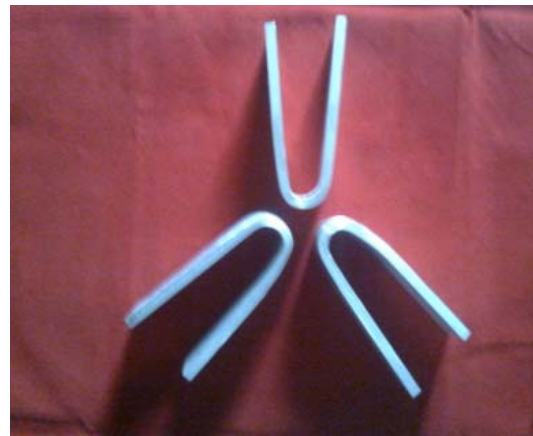
The face bed test was carried out for all the samples welded by square pin and flat shoulder tool (Table 4.4). As seen from Figure 4.10, there were no openings or cracks observed after the test. The result was satisfactory.

Table 4.4: Result for Face Bend Test

Test parameters	E10	E11	E12
Bending diameter mm	4(T) - 24		
Bending angle	180 °		
Observations	No opening or cracks observed		
Result	Satisfactory as per ASME section IX		



(a)



(b)

Figure 4.10: Face Bend test specimen welded by square tool pin profile after Testing

### 4.2.3 Brinell Hardness Test of CFSW Samples

#### 4.2.3.1 Brinell Hardness profile for sample E1A

Table 4.5: Brinell hardness for sample E1 A

Location	Hardness BHN
4A	65
3A	51
2A	49
1A	50
C	47
1R	49
2R	45
3R	47
4R	56
5R	62

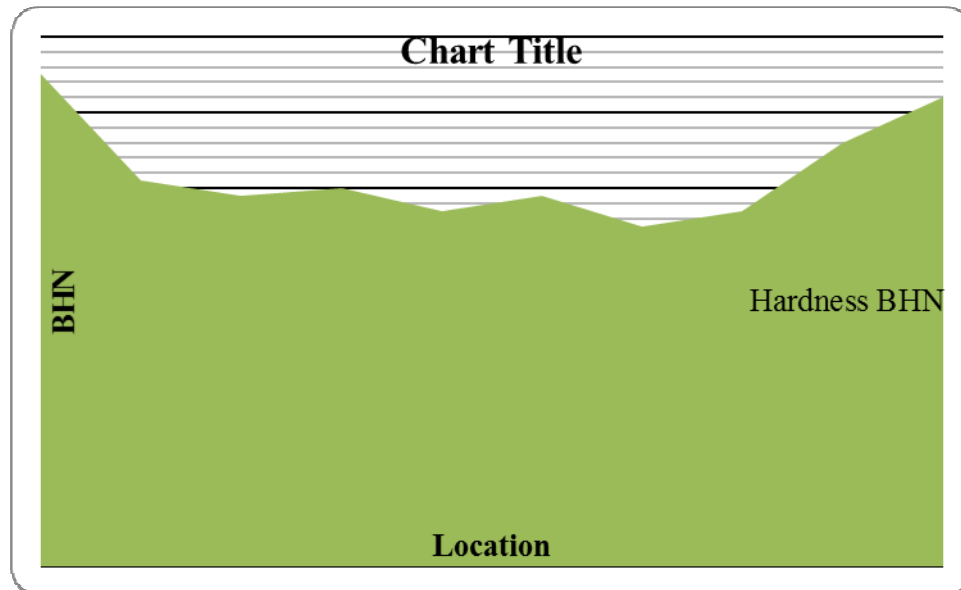


Figure 4.11: Brinell hardness profile for sample E1 A

### 4.2.3.2 Brinell Hardness profile for sample E1B

Table 4.6: Brinell hardness for sample E1 B

Location	Hardness BHN
5A	73
4A	56
3A	41
2A	61
1A	42
C	38
1R	41
2R	39
3R	40
4R	55
5R	52

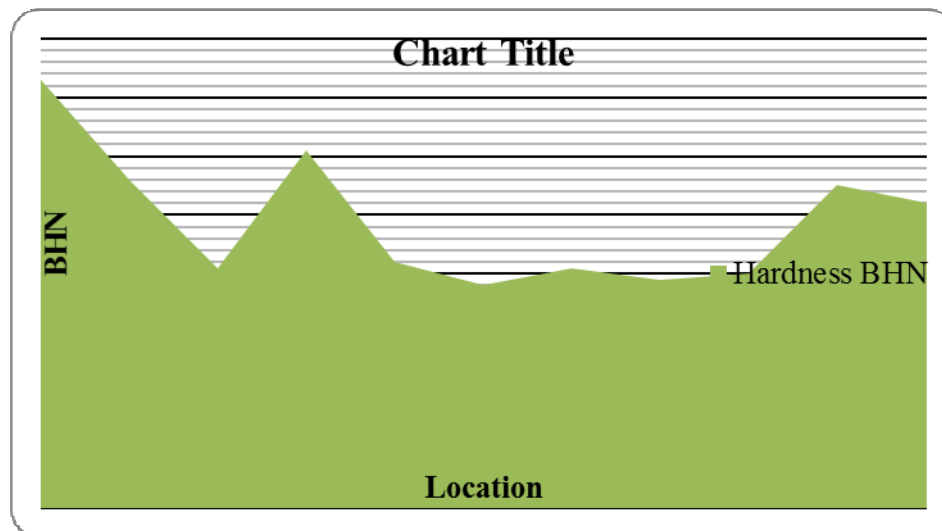


Figure 4.12: Brinell hardness profile for sample E1 B

### 4.2.3.3 Brinell Hardness profile for sample E2

Table 4.7: Brinell hardness for sample E2

Location	Hardness BHN
5A	59
4A	55
3A	45
2A	61
1A	40
C	39
1R	43
2R	64
3R	51
4R	62
5R	58

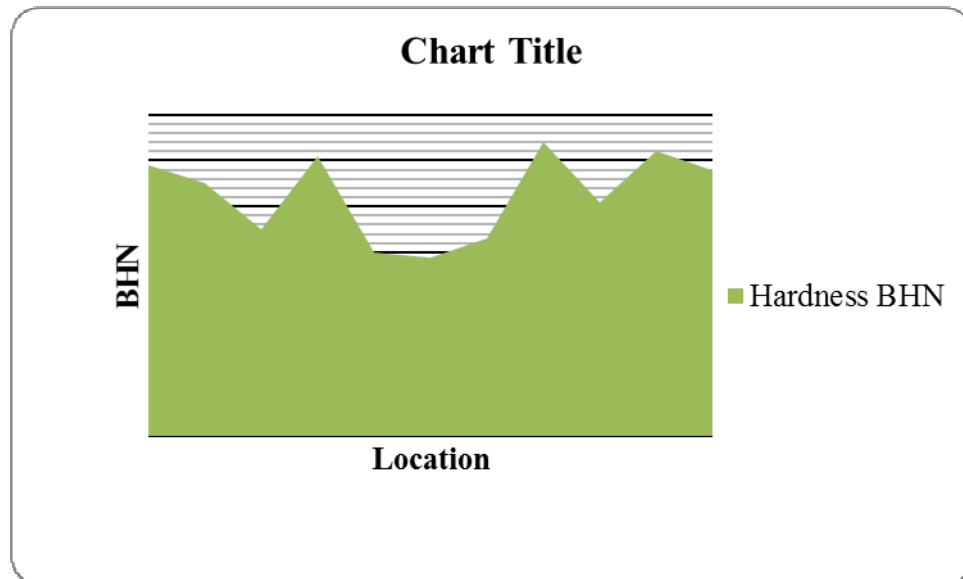


Figure 4.13: Brinell hardness profile for sample E2

#### 4.2.3.4 Brinell Hardness profile for sample E3

Table 4.8: Brinell hardness for sample E3

Location	Hardness BHN
5A	77
4A	44
3A	45
2A	42
1A	42
C	43
1R	45
2R	40
3R	46
4R	53
5R	64

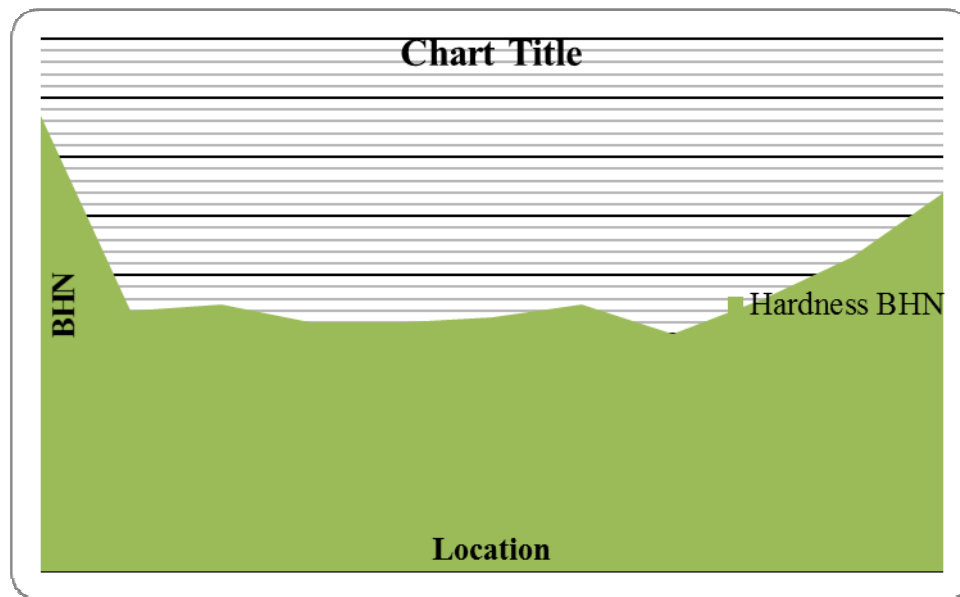


Figure 4.14: Brinell hardness profile for sample E3

#### 4.2.3.5 Brinell Hardness profile for sample E4

Table 4.9: Brinell hardness for sample E4

Location	Hardness BHN
7A	58
6A	70
5A	42
4A	40
3A	30.6
2A	44
1A	45
C	44
1R	46
2R	44
3R	40
4R	42
5R	65
6R	67
7R	67

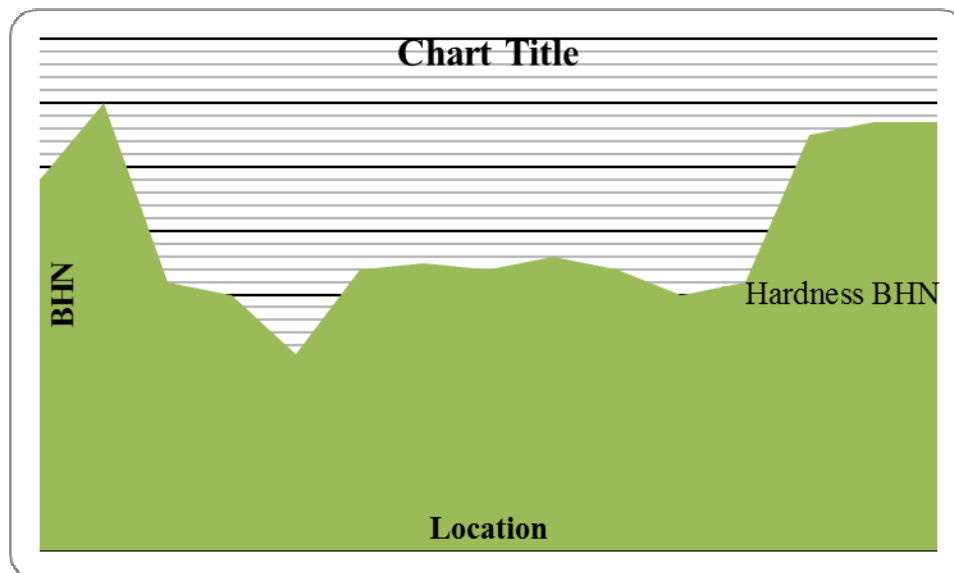


Figure 4.15: Brinell hardness profile for sample E4

#### 4.2.3.6 Brinell Hardness profile for sample E5

Table 4.10: Brinell hardness for sample E5

Location	Hardness BHN
7A	69
6A	69
5A	55
4A	55
3A	44
2A	44
1A	45
C	44
1R	42
2R	45
3R	44
4R	49
5R	65
6R	49
7R	69

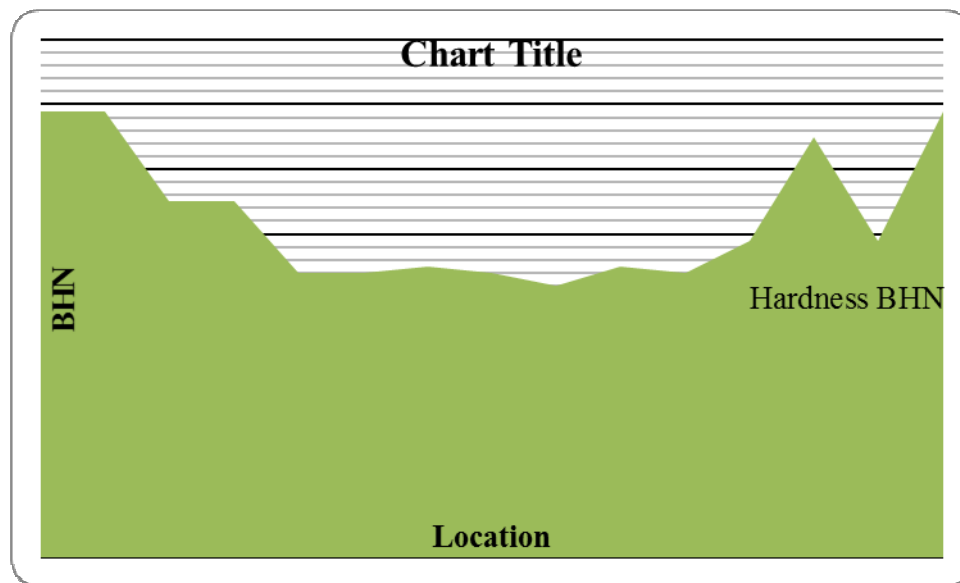


Figure 4.16: Brinell hardness profile for sample E5

#### 4.2.3.7 Brinell Hardness profile for sample E6

Table 4.11: Brinell hardness for sample E6

Location	Hardness BHN
7A	51
6A	65
5A	43
4A	25.9
3A	42
2A	42
1A	46
C	43
1R	45
2R	44
3R	47
4R	47
5R	53
6R	73
7R	71

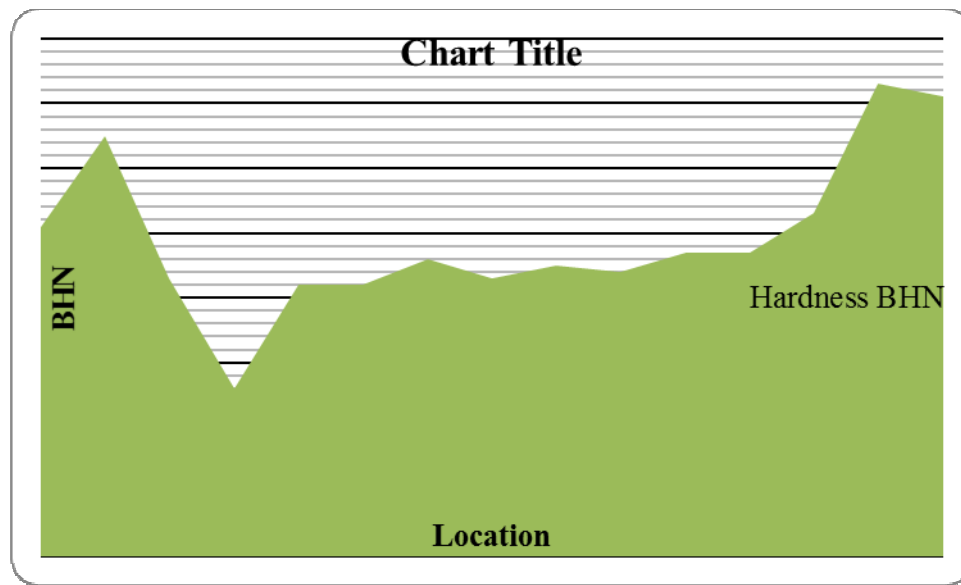


Figure 4.17: Brinell hardness profile for sample E6

#### 4.2.3.8 Brinell Hardness profile for sample E7

Table 4.12: Brinell hardness for sample E7

Location	Hardness BHN
7A	49
6A	44
5A	38
4A	38
3A	47
2A	49
1A	47
C	47
1R	45
2R	47
3R	50
4R	25.9
5R	46
6R	51
7R	50

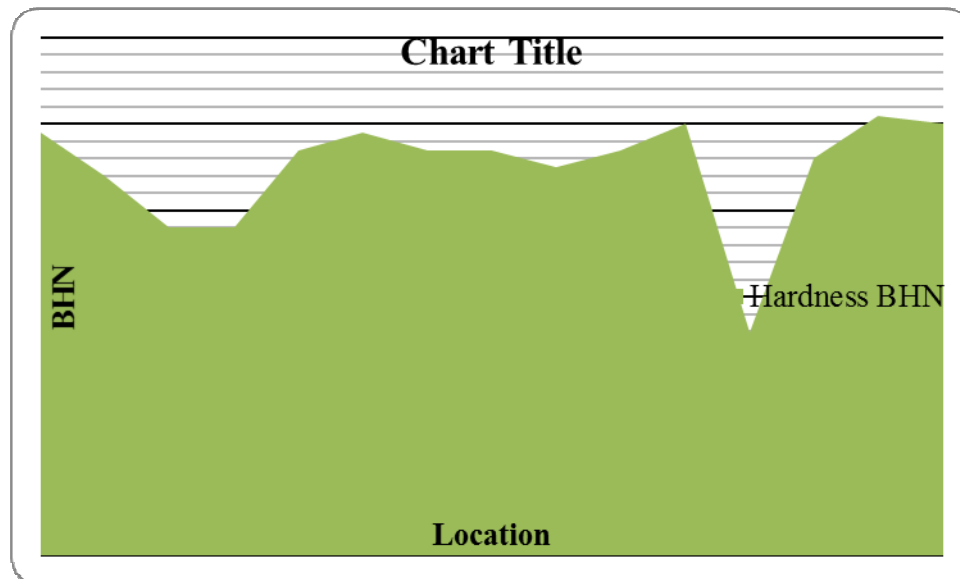


Figure 4.18: Brinell hardness profile for sample E7

### 4.2.3.9 Brinell Hardness profile for sample E8

Table 4.13: Brinell hardness for sample E8

Location	Hardness BHN
7A	53
6A	45
5A	44
4A	25.9
3A	31.2
2A	50
1A	47
C	42
1R	44
2R	45
3R	42
4R	38
5R	47
6R	53
7R	51

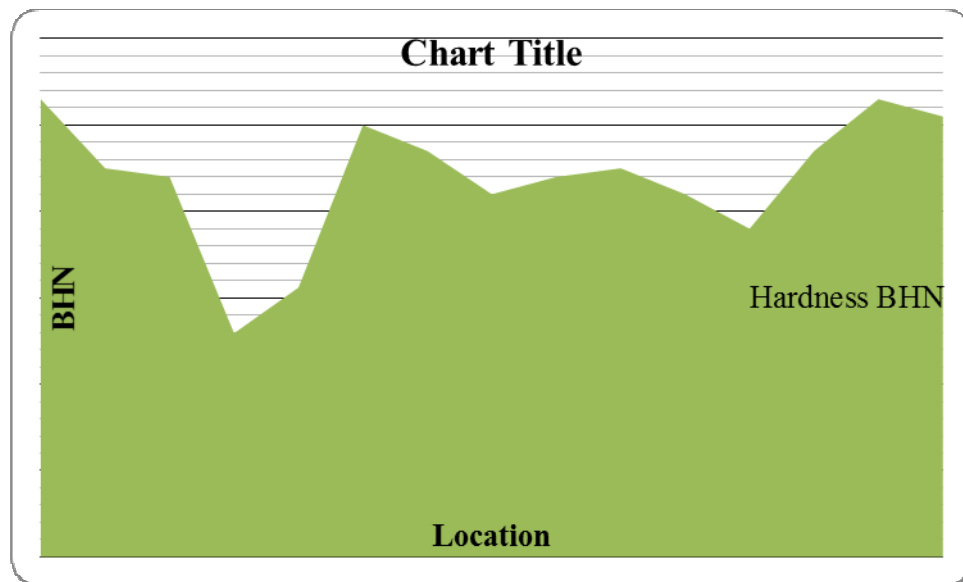


Figure 4.19: Brinell hardness profile for sample E8

#### 4.2.3.10 Brinell hardness profile for sample E9

Table 4.14: Brinell hardness for sample E9

location	Hardness BHN
7A	53
6A	53
5A	42
4A	34.4
3A	47
2A	49
1A	42
C	43
1R	46
2R	46
3R	46
4R	25.9
5R	41
6R	50
7R	53

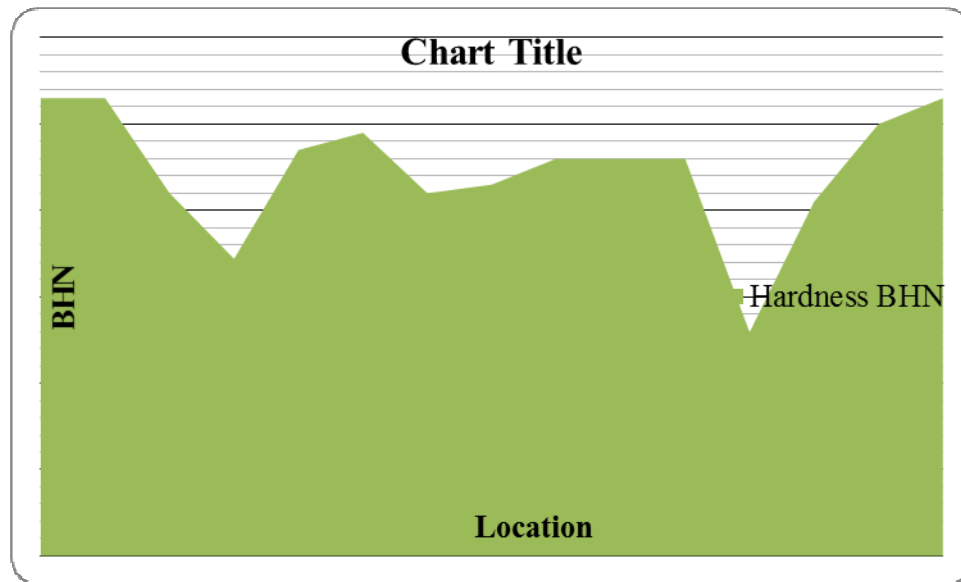


Figure 4.20: Brinell hardness profile for sample E9

#### 4.2.3.11 Brinell Hardness profile for sample E10

Table 4.15: Brinell hardness for sample E10

Location	Hardness BHN
7A	65
6A	61
5A	56
4A	41
3A	40
2A	40
1A	42
C	41
1R	41
2R	40
3R	38
4R	42
5R	52
6R	61
7R	64

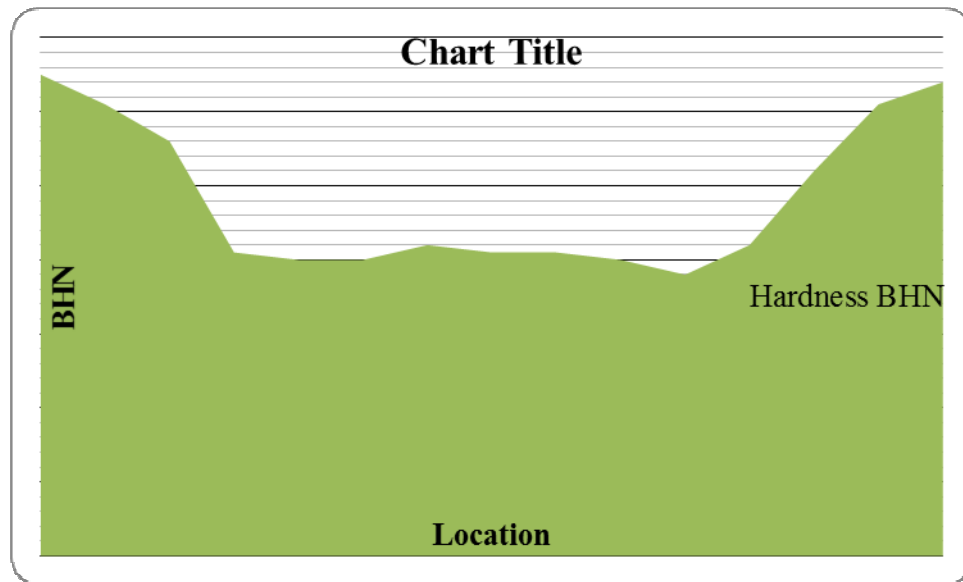


Figure 4.21: Brinell hardness profile for sample E10

#### 4.2.3.12 Brinell Hardness profile for sample E11

Table 4.16: Brinell hardness for sample E11

Location	Hardness BHN
7A	56
6A	46
5A	42
4A	38
3A	38
2A	44
1A	44
C	50
1R	41
2R	42
3R	34
4R	40
5R	41
6R	44
7R	53

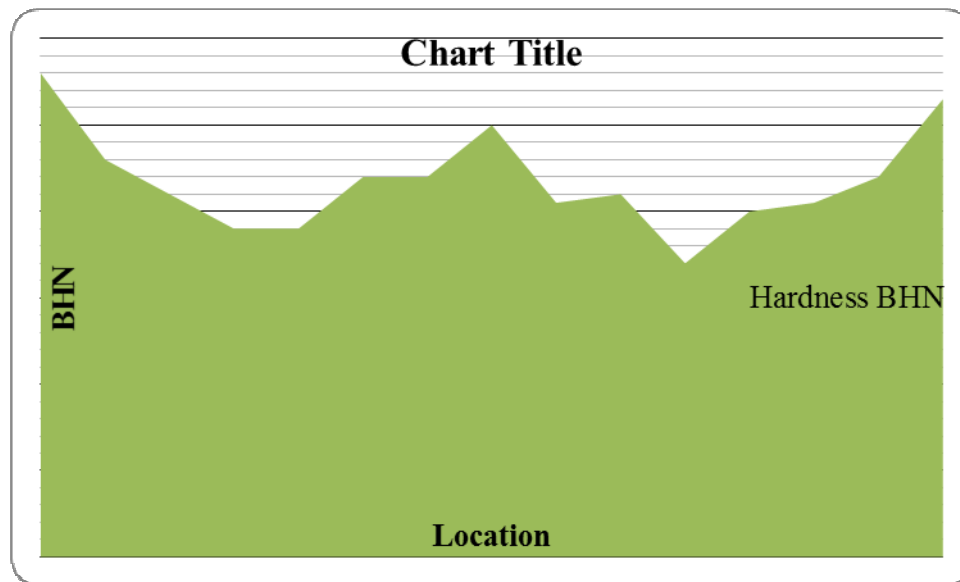


Fig 4.22: Brinell hardness profile for sample E11

#### 4.2.3.13 Brinell Hardness profile for sample E12

Table 4.17: Brinell hardness for sample E12

Location	Hardness BHN
7A	61
6A	58
5A	53
4A	42
3A	39
2A	46
1A	44
C	42
1R	42
2R	42
3R	41
4R	32
5R	41
6R	46
7R	53

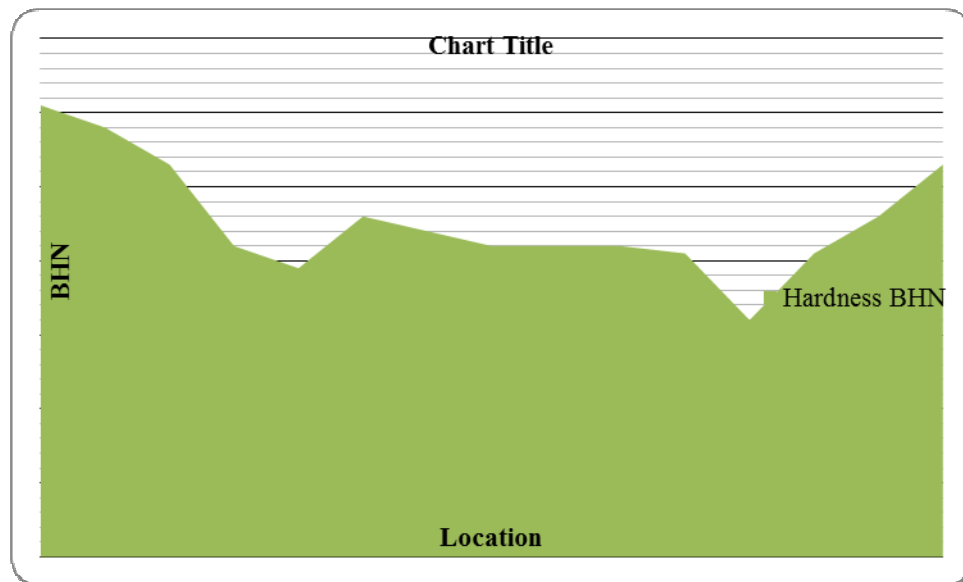


Figure 4.23: Brinell hardness profile for sample E12

### **4.3 EFFECT OF TOOL DESIGN ON WELD**

It is observed from the literature that there is no universal tool used in CFSW or BFSW. It is a need of time to disclose the facts and factual design be made available globally for the use in industries. Guidelines drawn from the CFSW literatures are contrary to the approaches followed for BFSW research experiments. For example, the shoulder diameter is taken three times the substrate thickness and the pin diameter should be similar to the thickness of the material to be welded [45][56]. But different proportions are used in BFSW. The work of Liu, et al. [141] using featureless bobbin tools is contradictory to other researchers [29][71][142] who felt it essential to have at least threads on the pin.

#### **4.3.1 Effect of tool features**

In the present research work different tools were developed with the pin and shoulder features e.g. plain cylindrical, threaded and flat on pin, and shoulder have features like flat, concave and concentric semicircular ring at edge. Out of the range and series of experiments four flat pin (square) was found to better compare to hexagonal and plain cylindrical pin. While flat shoulder gave better results compare to other two.

Similarly for BFSW also different tools were fabricated and welding was done.

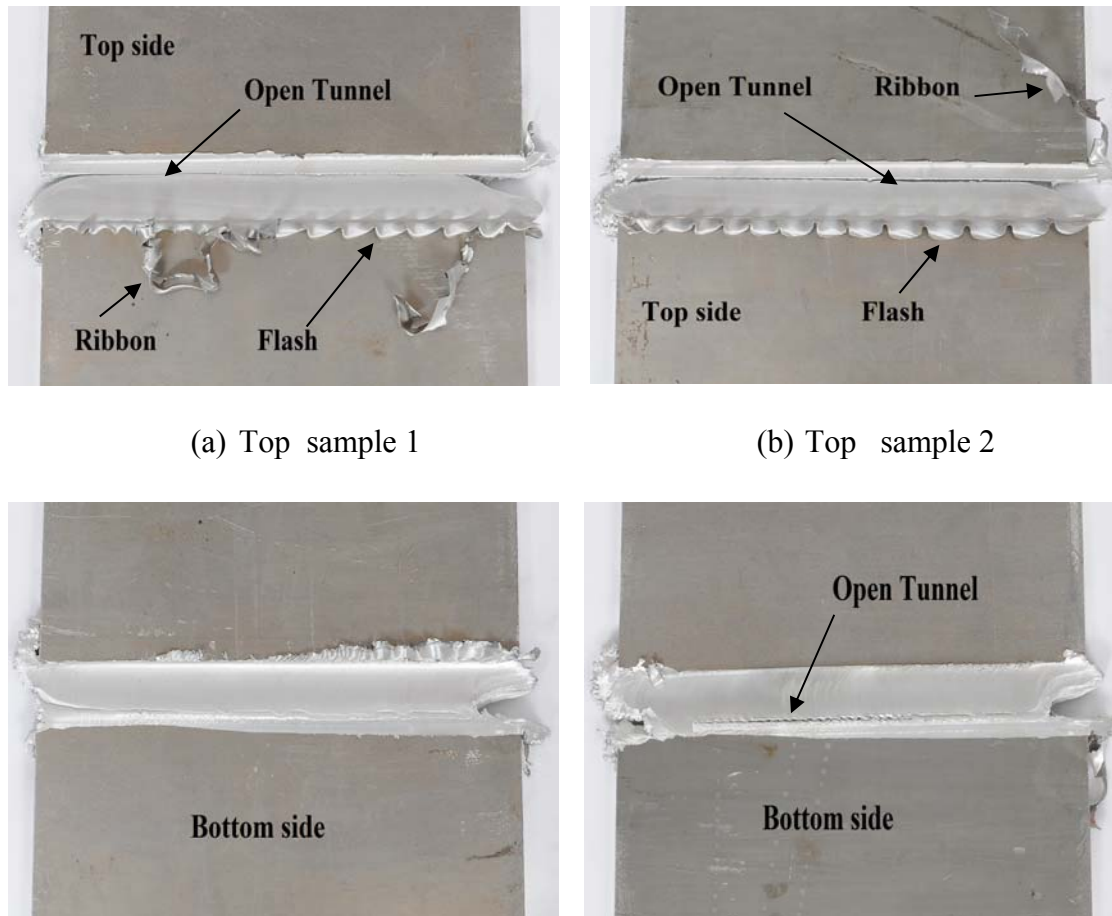
### **4.4 SUBSTRATES WELDED BY FIXED GAP BOBBIN TOOL**

A fixed gap bobbin tool with cylindrical pin was manufactured and tested for the weld trials. The tool dimensions were taken as per CFSW tool design. During the weld trials the tool failed as shown in figure 4.24. It is because of the small pin diameter and weaker section to resist temperature generated from two shoulders. Ultimately a new design was demanded having better pin features and larger pin cross section.



Figure 4.24: Failure of cylindrical bobbin tool during welding

**4.4.1 Results obtained for welding of AA 6082 T6 Al alloy using Bobbin tool with square pin tool with concave (top) and convex (bottom) shoulder. BT1**



(c) Bottom sample 1 (800rpm)

(d) Bottom sample 2 (600rpm)

Figure 4.25: Top and bottom surface of sample, welded at 800rpm and 600rpm tool rotational speed and 48mm/min traversing speed with bobbin tool BT1

Surface tunnel defect (figure 4.25) is observed on the top and bottom side of plates. The plates were welded at two different rotational speeds 600 and 800 rpm and 48 mm/min welding speed. It may be due to insufficient heat generated out of tool shoulder compression, as in this case concave and convex shoulder profile is selected. Flash is sufficiently high at top side than at bottom side. Also flash in the form of thin skin observed, is due to additional compression between the shoulders and the surface oxides.

#### 4.4.2 Results obtained for welding of AA 6082 T6 Al alloy using Bobbin tool with square pin tool and convex shoulder. BT2

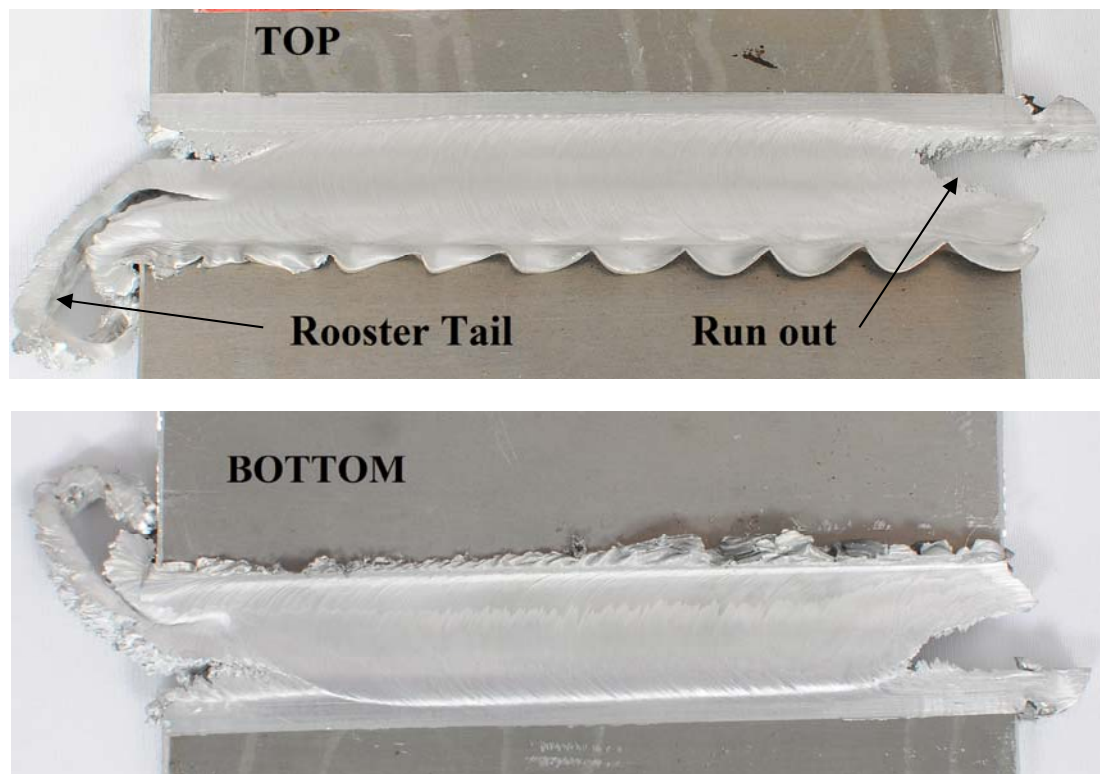


Figure 4.26: Plates welded with convex shoulder, square pin bobbin tool BT2 at 1000 rpm rotational speed and 24 mm/min traversing speed.

The AA6082 T6 alloy was welded at 1000 rpm and 800 rpm rotational speed and 24mm/min traversing speed as shown in figure 4.26 and 4.27. A rooster tail in the beginning of weld and run out at the end of weld is seen in the figure 4.26 and 4.27. Very less amount of material wastage is observed in the beginning and at the end of weld. K. J. Colligan et al. [142] explained the phenomenon of Weld Initiation Failure and factors

responsible for it. Which is found here in less percentage showing the performance of the tool, tool design. A bulging or surface overlay is visible at the bottom side is due to the higher shoulder compression at the top side of the substrate which can be corrected by proper tool alignment with the plate faces. Looking to the surface, it seems to be good compare to previous welds carried out by BT1 tool.

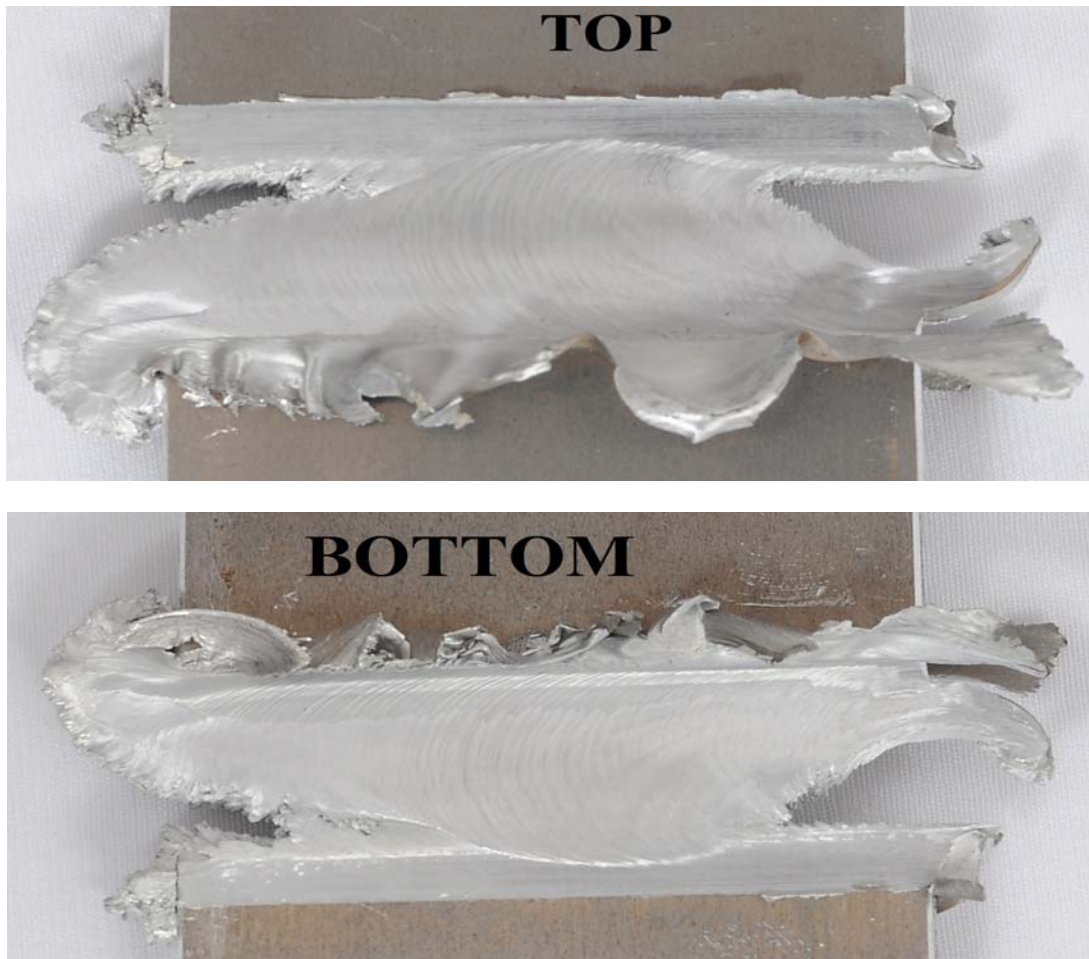


Figure 4.27: Plates welded with convex shoulder, square pin bobbin tool BT2 at 800rpm rotational speed and 24mm/min traversing speed.

The plates shown in figure 4.27 were welded at 800 rpm spindle speed and 24 mm/min welding speed. The joints found to be satisfactory with no tunnel or lack of penetration problem. The samples were tested for metallography and SEM analysis was also carried out to know the joint details.

From the above welds it is understood that the convex tool design is more suitable in case of bobbin tool. The design of tool also have additional benefit to accommodate variations in the plate thickness. It was found that the raw material in the form of sheet received is not having a constant thickness throughout the surface. The author measured the plate thickness at different places before and after cutting to size, and found variations more than 0.15 to 0.5 mm.

## 4.5 MICROSTRUCTURE ANALYSIS

### 4.5.1a Microstructure Analysis of sample E1 A, 100x

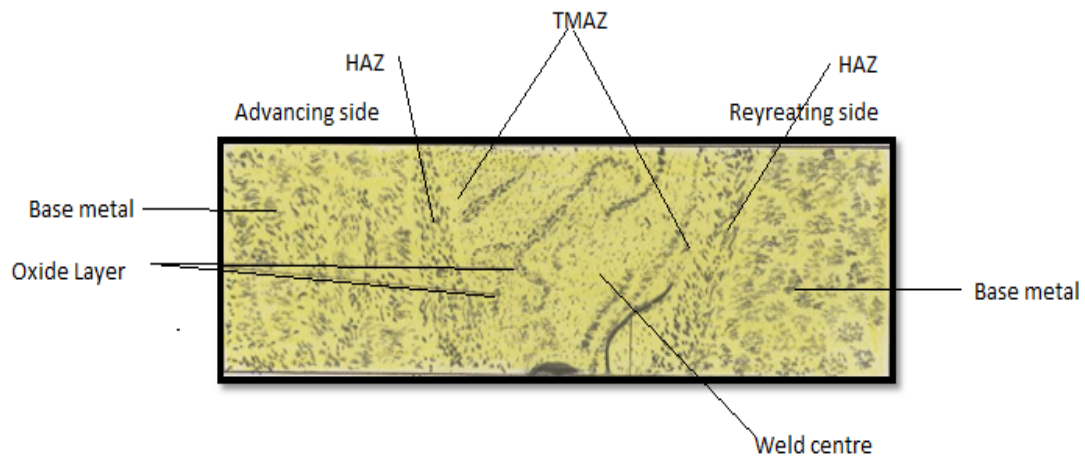
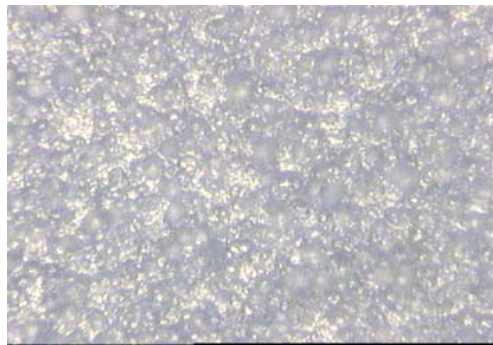
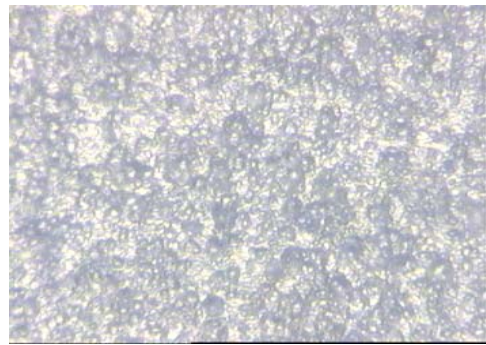


Figure 4.28: Microstructure of sample E1 A

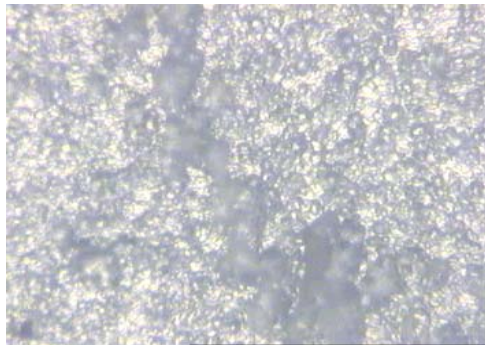
**4.5.1b Microstructure analysis of sample E1 A, 250x**



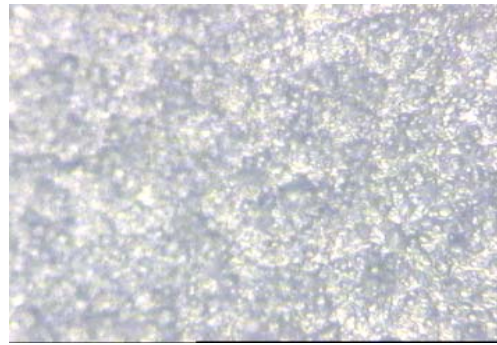
(a) HAZ at AS



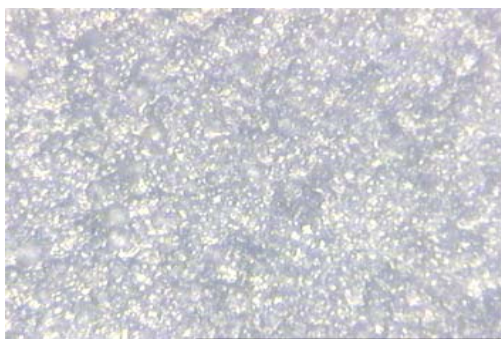
(b) TMAZ at AS



(c) Nugget



(d) Weld Centre



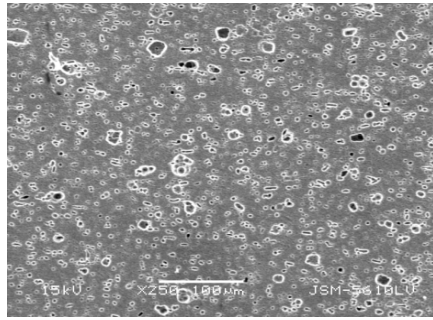
(e) TMAZ at RS



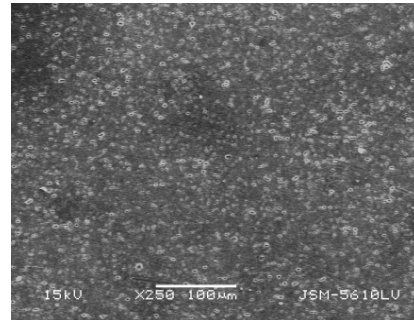
(f) HAZ at RS

Figure 4.29: Microstructure of sample E1 A at 250x using Neophot (a) HAZ at AS (b) TMZ at AS (c) Nugget (d) Weld Centre (e) TMAZ at RS (f) HAZ at RS

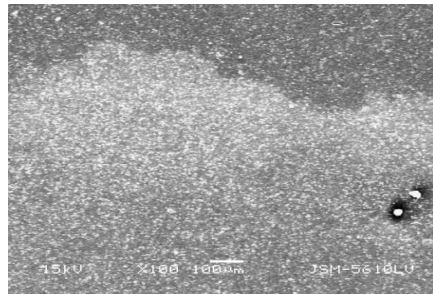
4.5.1c SEM Analysis of sample E1 A, 250x



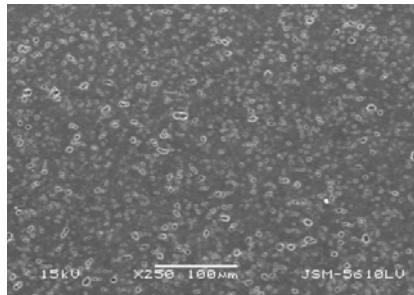
(a) HAZ at AS



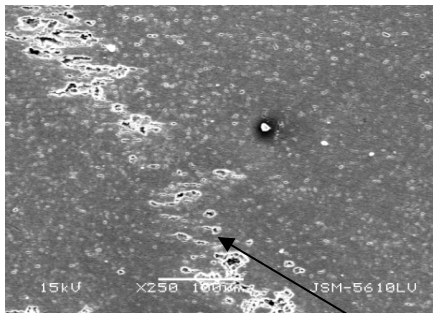
(b) TMAZ at AS



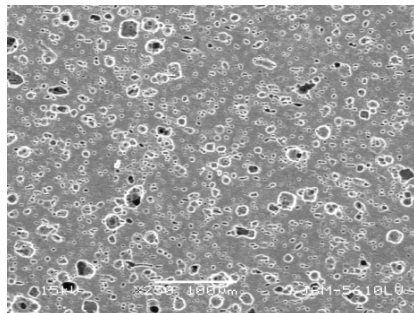
(c) Nugget



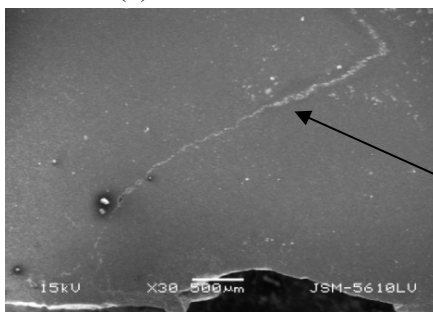
(d) Weld Centre



(e) TMAZ at RS



(f) HAZ at RS



(g) JLR at 50x

Oxide formation

Joint Line Remnant

Figure 4.30: SEM analysis of sample E1 A at 250 x (a) HAZ at AS (b) TMZ at AS (c) Nugget (d) Weld Centre (e) TMAZ at RS (f) HAZ at RS (g) JLR 50x

#### **4.5.1d Observation of sample E1 A**

The weld center is subjected to severe plastic deformation combined with the physical flow of the material around tool pin stirring and substantial increase of temperature. The welding of this sample was carried out with hexagonal pin with concave shoulder. The tool rotation speed was 545 rpm with 50 mm/min feed rate. The welding was carried out parallel to rolling direction.

The Figure 4.28 and 4.29 shows the microstructure of sample E1 A at 100x and 250x magnification while Figure 4.30 shows the SEM analysis for the sample E1 A

The microstructures of the weld center consist of the coarse grain structure. It consists of the coarse grains of Al with precipitates of  $Mg_2Si$ .

In the HAZ at Advancing side and Retreating side, the microstructure consist of the coarse grains of Al with precipitates of  $Mg_2Si$  there is also formation of precipitates free zone along grain boundary.

In the TMAZ, the microstructure consist of the ripen precipitates of  $Mg_2Si$ . And also there is presence of the precipitates free zones appears the grains are fine compare to the base metal and HAZ of the both side, advancing as well as retreating side.

In the nugget region, the microstructure consists of fine equiaxed recrystallized grains comprised with the dark bands. The  $Mg_2Si$  precipitates in the nugget zone possess high particle density.

**4.5.2a Microstructure Analysis of sample E1 B, 100x**

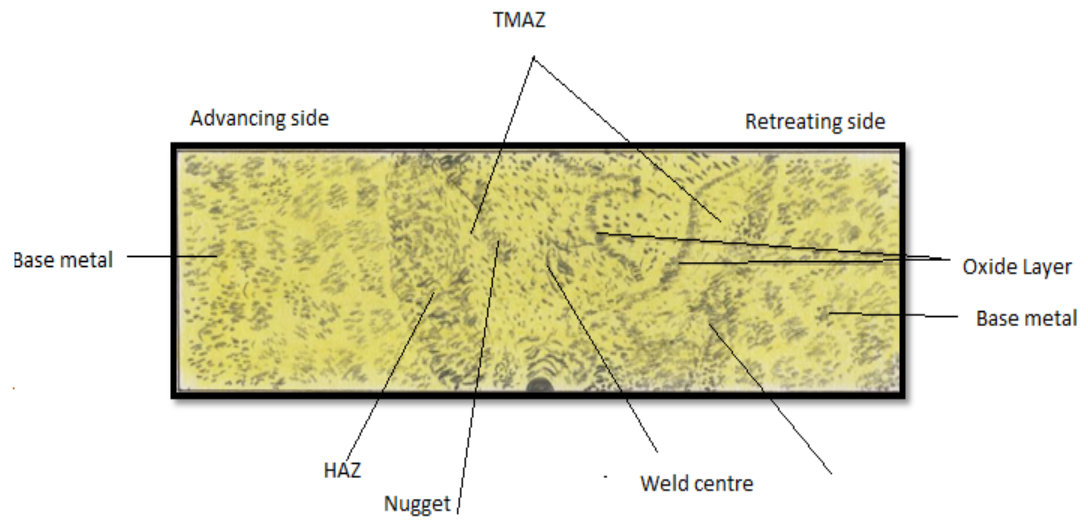
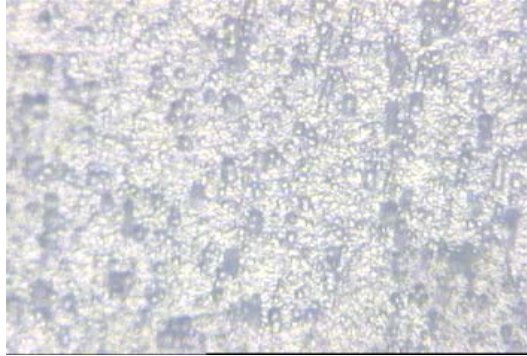
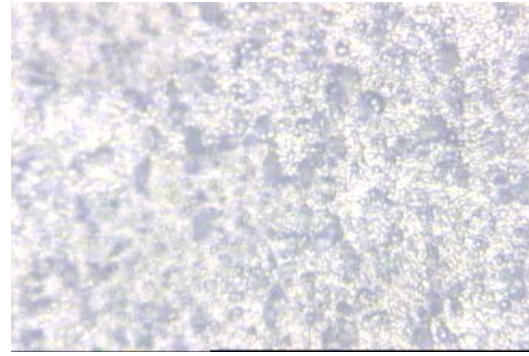


Figure 4.31: Microstructure of Sample E1

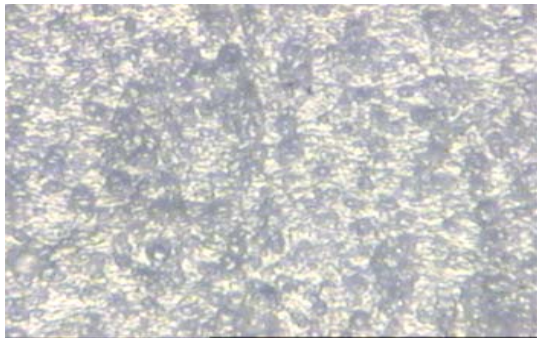
**4.5.2b**      **Microstructure analysis of sample E1 B, 250x**



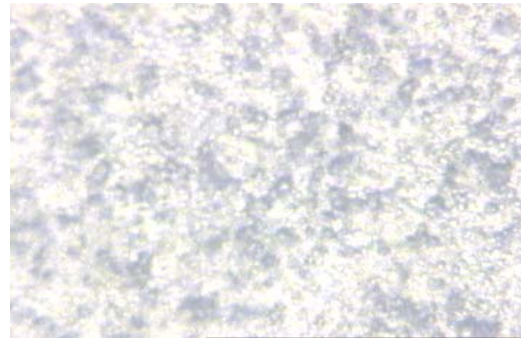
(a) HAZ at AS



(b) HAZ at RS



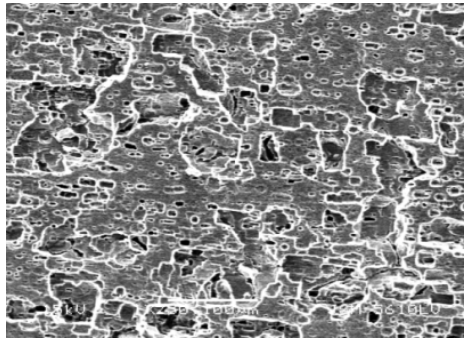
(c) Boundary between TMAZ & Nugget



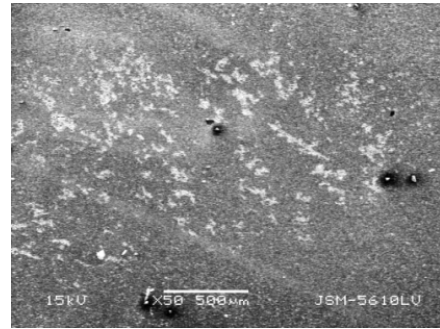
(d) TMAZ/weld centre,

Figure 4.32: Microstructure Analysis of sample E1B with Neophot at 250x; (a) HAZ at AS (b) HAZ at RS  
(c) Boundary between TMAZ & Nugget (d) TMAZ weld centre

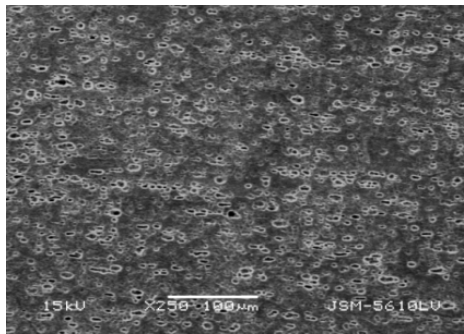
4.5.2c SEM Analysis of sample E1 B, 250x



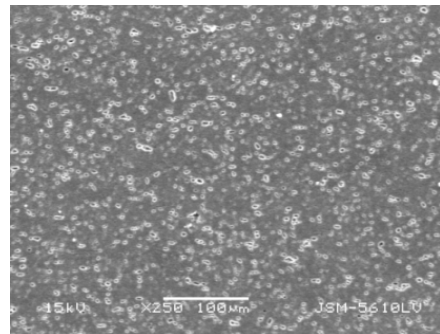
(a) Base metal



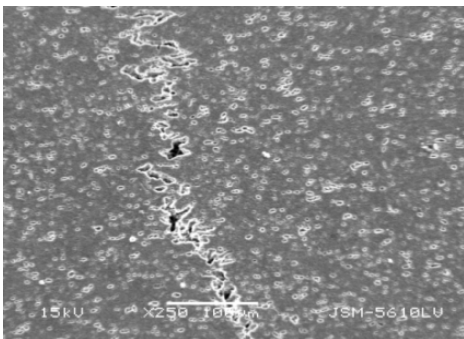
(b) Nugget



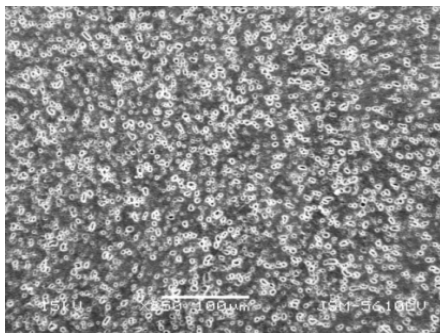
(c) HAZ at AS



(d) HAZ at RS



(e) TMAZ - Weld center



(f) TMAZ - HAZ bottom RS

Figure 4.33: SEM analysis of sample E1 B at 250x (a) Base metal (c) Nugget (c) HAZ at AS (d) HAZ at RS (e) TMAZ -Weld center (f) TMAZ - HAZ bottom RS.

#### **4.5.2d Observation of sample E1 B**

The Figure 4.31 and 4.32 shows the microstructure of sample E1 B at 100x and 250x magnification while Figure 4.33 shows the SEM analysis for the sample E1 B

In the Thermo mechanically affected zone, the microstructure consist of fine grains of Al compare to Base metal & the ripen precipitates of  $Mg_2Si$ .there is also presence of precipitates free zones in the TMAZ.

The weld center is subjected to severe plastic deformation combined with physical flow of the material around tool pin stirring and substantial increase of temperature. The micro structure consist of the destroyed hardening precipitates of  $Mg_2Si$ .Due to high temperature there was dissolution of the precipitates take place & there was breaking of the coherent precipitates by gliding of the dislocation was occurred.

There was dynamic recrystallization as well as Re-precipitation of the  $Mg_2Si$  take place in the weld center forming microstructure comprising of fine, equiaxed grains and large precipitates. At center of top region of weld, there is presence of the oxide layer. It may be the aluminum oxide. At boundary between the TMAZ & HAZ, there was formation of nugget it consist of the onion ring structure. The microstructure consist of fine, equiaxed grains with higher density precipitates with dark bands & coarse grains with lower precipitates with light bands.

The microstructure of HAZ at advancing side consist of the fine grains of Al with smaller size of  $Mg_2Si$  precipitates compare to HAZ at Retreating side. The HAZ at retreating side consist of the coarse grains of Al with precipitates of  $Mg_2Si$ . There is also presence of the precipitates free zones in the HAZ at the both side.

**4.5.3a Microstructure Analysis of sample E2, 100x**

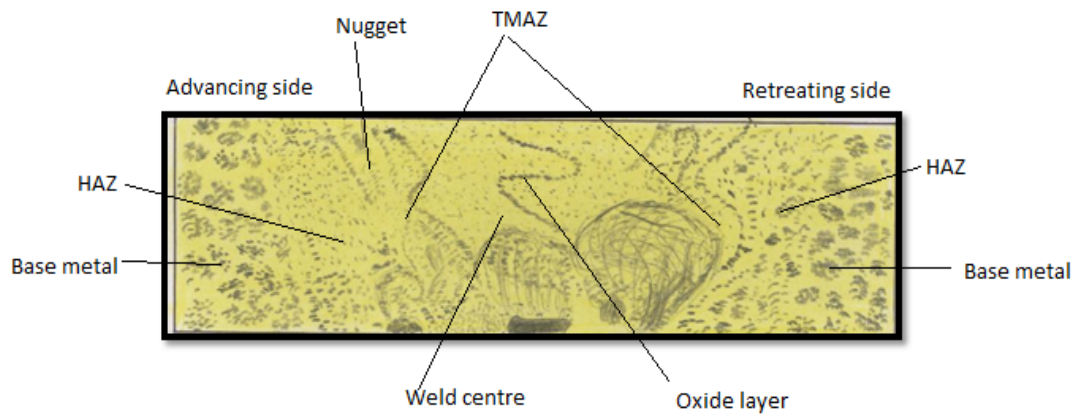


Figure 4.34: Microstructure of sample E2

**4.5.3b Microstructure analysis of sample E2, 250x**

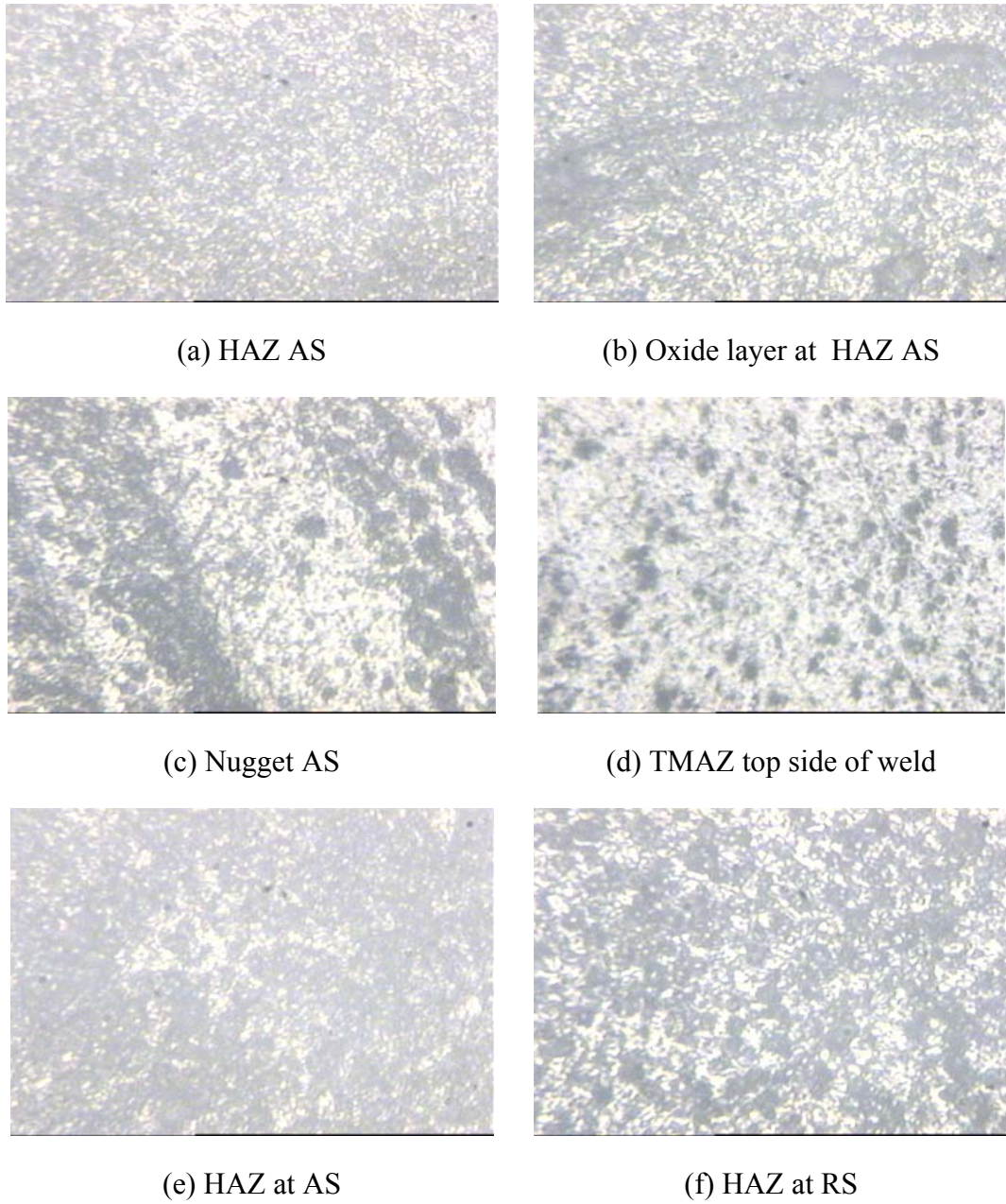
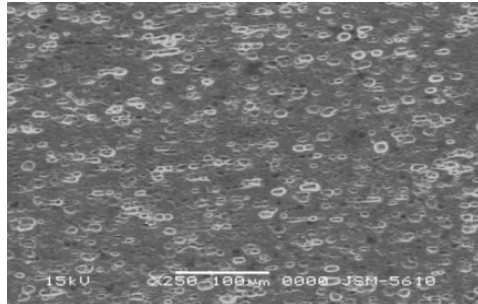
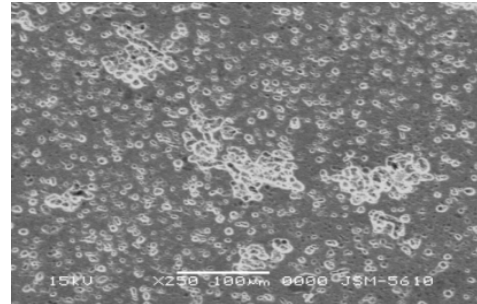


Figure 4.35: Microstructure analysis of sample E2 with Neophot 250x; (a) HAZ AS (b) Oxide layer at HAZ AS (c) Nugget AS (d) TMAZ top side of weld (e) HAZ at AS (f) HAZ at RS.

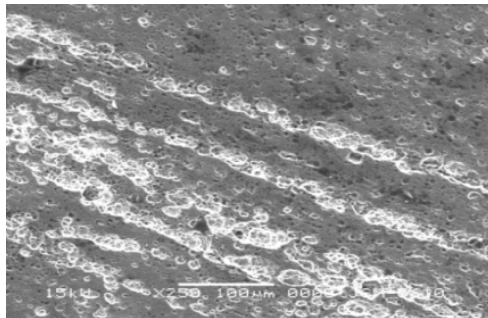
**4.5.3c SEM Analysis of sample E2, 250x**



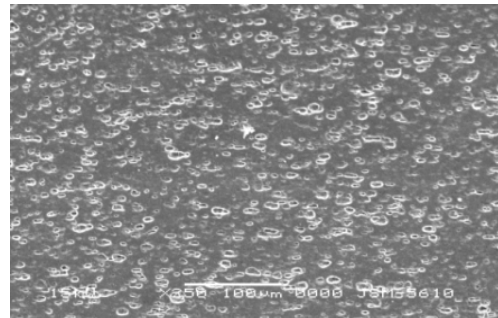
(a) HAZ at AS



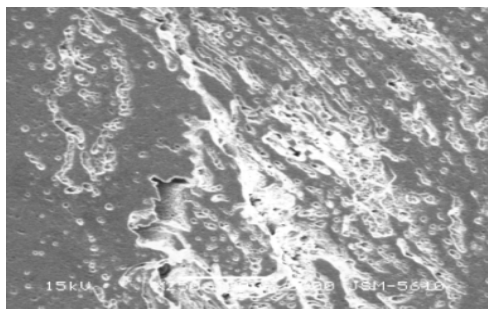
(b) TMAZ at AS



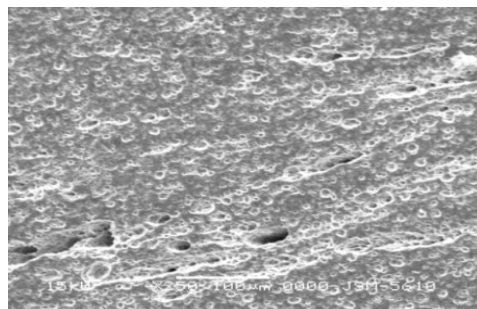
(e) Nugget zone



(f) Weld centre



(c) TMAZ-Weld center



(d) TMAZ at RS

Figure 4.36: SEM analysis of sample E2 at 250x. (a) HAZ at AS (b) TMAZ at AS (c) TMAZ- Weld center (d) Nugget zone (e) TMAZ at RS (f) Weld center

#### **4.5.3d Observation of sample E2**

The Figure 4.34 and 4.35 shows the microstructure of sample E2 at 100x and 250x magnification while figure 4.36 shows the SEM analysis for the sample E2

The weld center is subjected to severe plastic deformation combined with physical flow of material around the tool pin stirring and substantial increase in the temperature.

The microstructure consist of the destroyed phase  $Mg_2Si$ . Due to high temperature, there was thermal dissolution of the precipitates take place & there was breaking of the coherent precipitates by gliding of the dislocation was occurred. There was dynamic recrystallization as well as reprecipitation of the  $Mg_2Si$  take place. In the weld center formation of fine equiaxed grains & large precipitates are present.

In the TMAZ the microstructure consist of the fine grains of aluminum compare to the base metal and ripen precipitates of  $Mg_2Si$ . In this case there is more precipitates free zone appears in the TMAZ. At boundary near the TMAZ and HAZ at advancing side and retreating side there is formation of oxide layer.

The Nugget form at the advancing side ,the microstructure consist of the onion ring structure with fine, equiaxed grains with dark bands & coarse grains with lighter bands with precipitates of  $Mg_2Si$ .

The HAZ at advancing side consist of the fine grains of Al with precipitates of  $Mg_2Si$  compare to the HAZ at retreating side in the HAZ at Advancing side there is more precipitates free zones compare to HAZ at Retreating side. At boundary between the TMAZ and HAZ, there is formation of an oxide layer.

**4.5.4a Microstructure Analysis of sample E3, 100x**

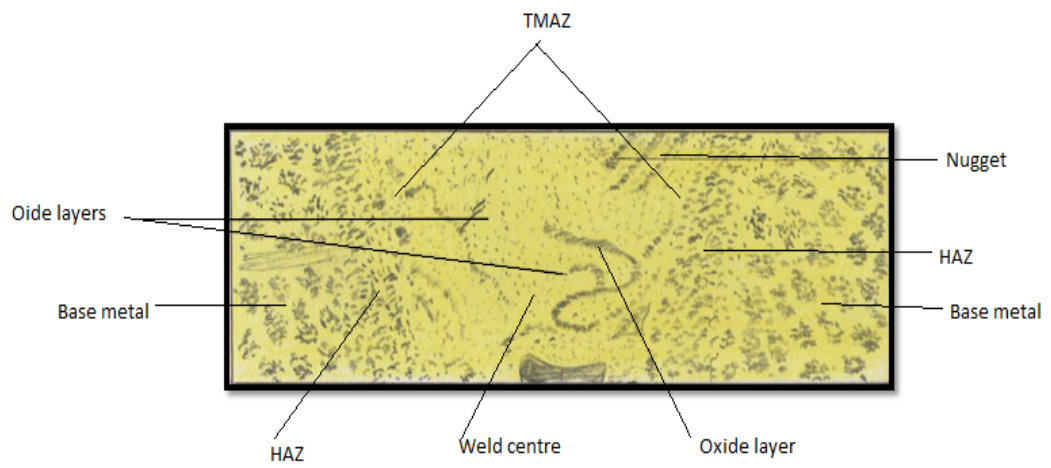
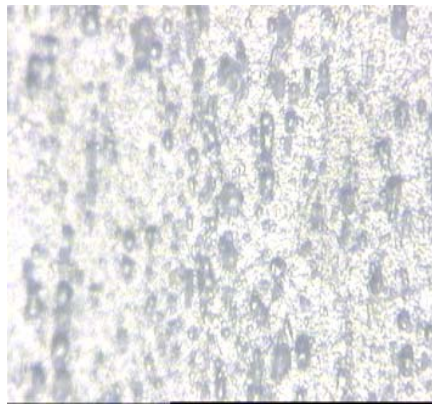


Figure 4.37: Microstructure of sample E3

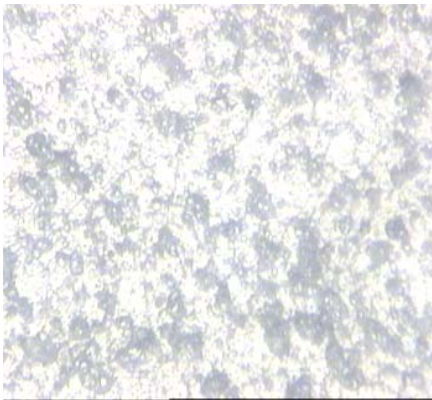
**4.5.4b Microstructure analysis of sample E3, 250x**



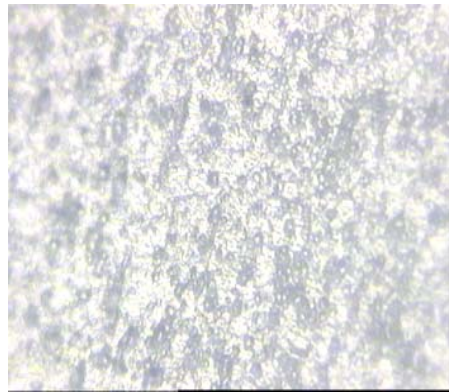
(a) HAZ at AS



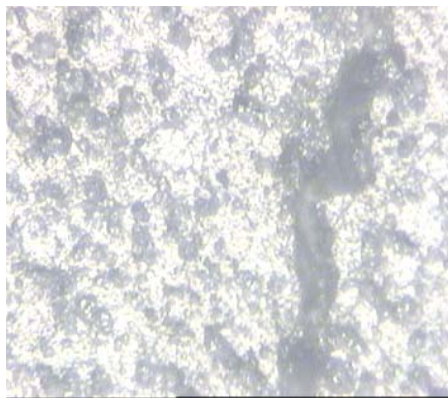
(c) TMAZ at AS



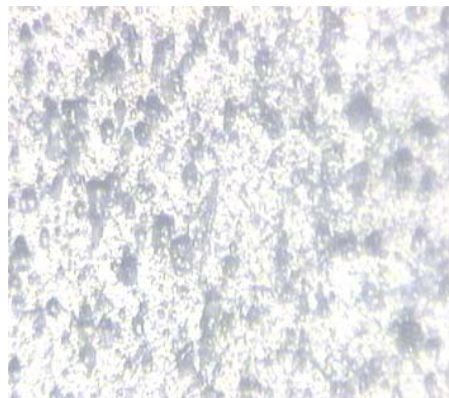
(e) Weld center



(f) TMAZ-Nugget



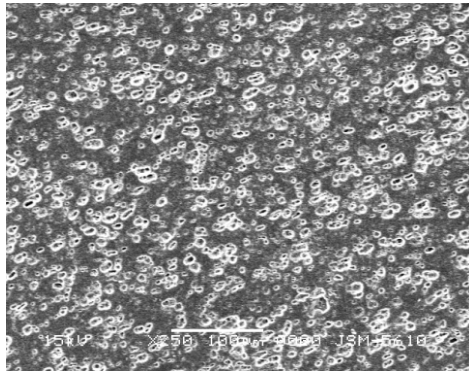
(d) TMAZ at RS



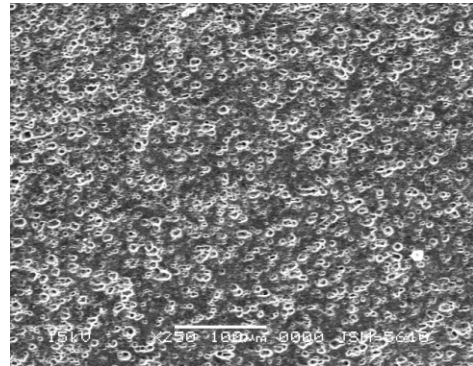
(b) HAZ at RS

Figure 4.38: Microstructure of sample E3 at 250x using Neophot (a) HAZ at AS (b) TMAZ at AS (c) Weld center (d) Nugget (e) TMAZ at RS (f) HAZ at RS

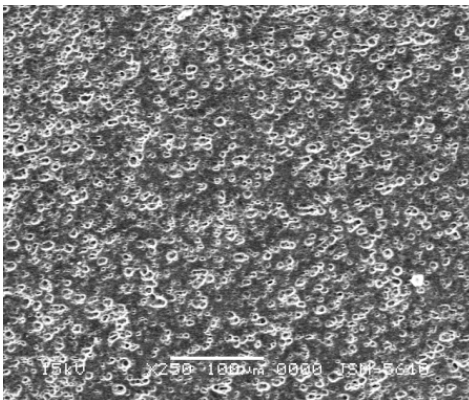
4.5.4c SEM Analysis of sample E3, 250x



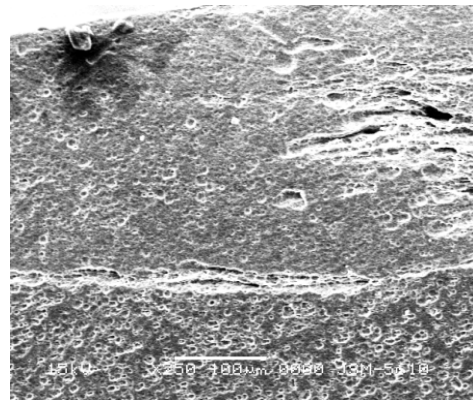
(a) HAZ at AS



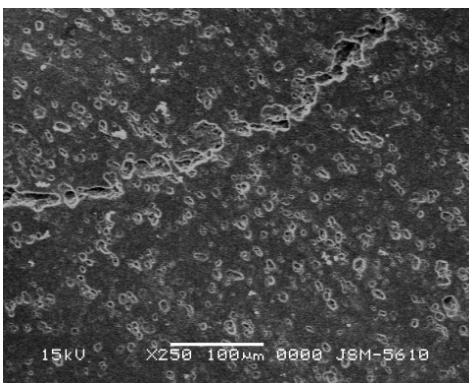
(b) TMAZ at AS



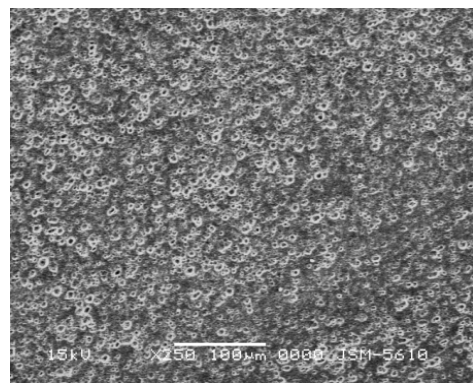
(c) Weld center



(d) Nugget



(e) TMAZ at RS



(f) HAZ at RS

Figure 4.39: SEM analysis of sample E3 at 250X (a) HAZ at AS (b) TMAZ at AS (c) Weld center (d) Nugget (e) TMAZ at RS (f) HAZ at RS

#### **4.5.4d Observation of sample E3**

The Figure 4.37 and 4.38 shows the microstructure of sample E3 at 100x and 250x magnification while Figure 4.39 shows the SEM analysis for the sample E3.

The weld center consists of the fine recrystallized grains of Al with breaking of the Mg<sub>2</sub>Si precipitates. There was a dynamic recrystallization was observed and also re precipitation occurred.

In the TMAZ the microstructure consist of the fine grains of Al compare to base metal with the precipitates of Mg<sub>2</sub>Si. There is formation of more precipitates free zone. At boundary between the TMAZ and HAZ at retreating side there is formation of the oxide layer. It may be the oxide of aluminum.

In the Nugget region the microstructure consist of the onion ring structure or say to be the banded structure. the microstructure consist of fine and equiaxed grains with dark bans having higher particle density and the coarse grains with lighter bands with low particle density.

The HAZ at advancing side consist of the coarse grains of Al with the Mg<sub>2</sub>Si precipitates. The distribution of Mg<sub>2</sub>Si precipitates is uniform. The HAZ at retreating side consist of the coarse grains of Al with more crowding of Mg<sub>2</sub>Si precipitates so the precipitates free zone are less at the retreating side compare to the HAZ at advancing side. At boundary between the HAZ and TMAZ there is formation of oxide layers.

#### 4.5.5a Microstructure Analysis of sample E4, 100x

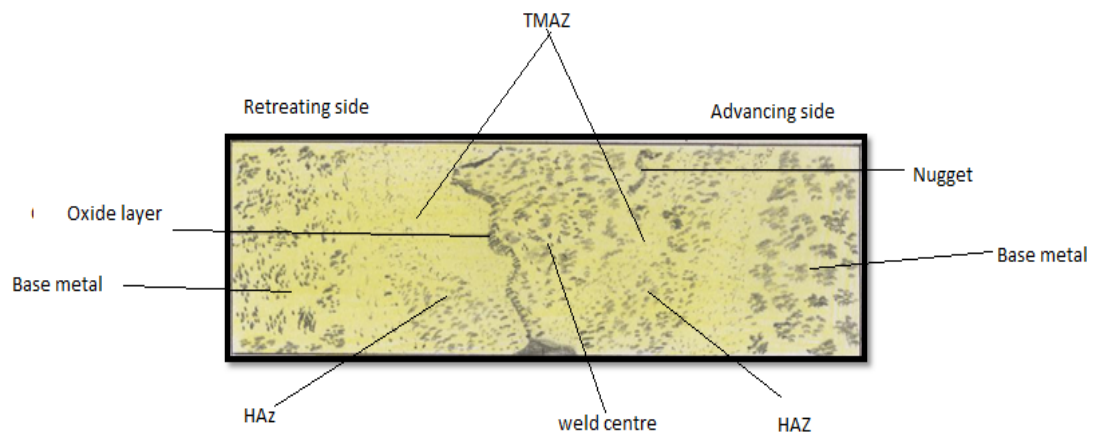
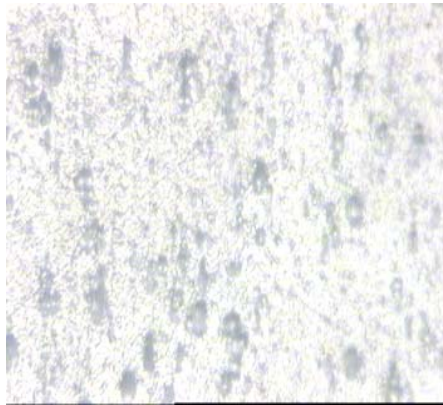
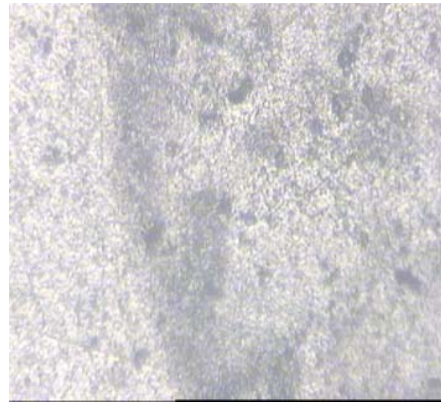


Figure 4.40: Microstructure of sample E4

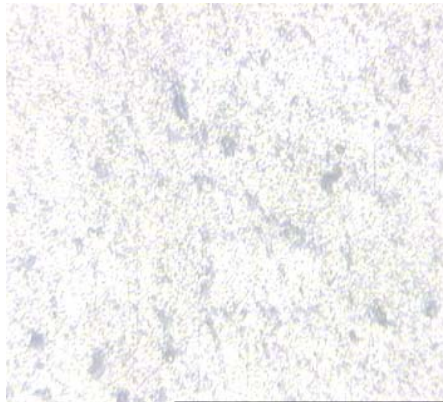
**4.5.5b Microstructure analysis of sample E4, 250x**



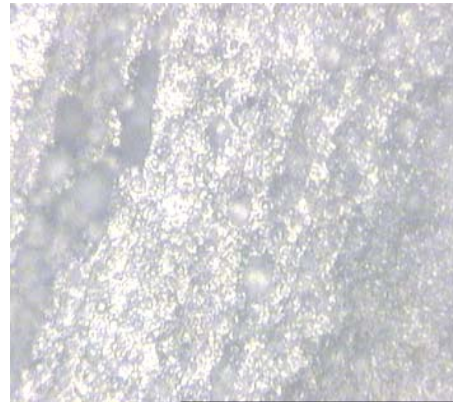
(a) HAZ at AS



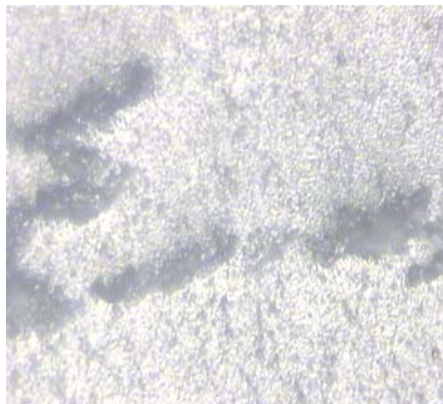
(b) TMAZ - Weld centre



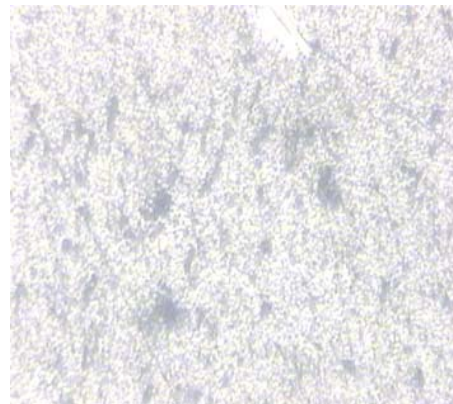
(c) Weld center



(d) Nugget



(e) TMAZ at RS

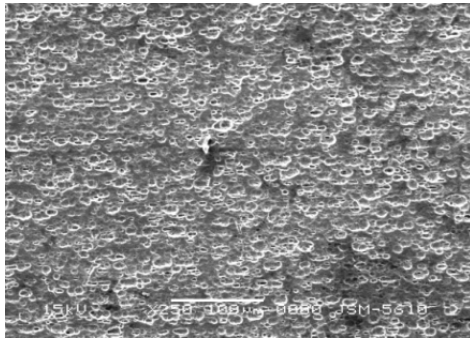


(f) HAZ at RS

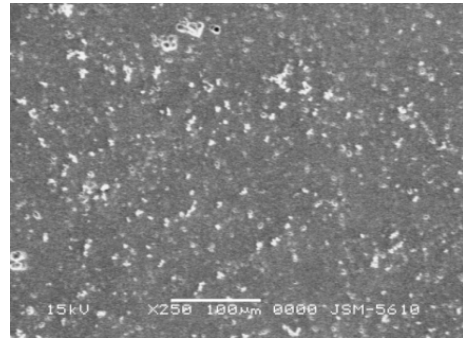
Figure 4.41: Microstructure analysis of sample E4 using Neophot, at 250x (a) HAZ at AS (b) TMAZ at AS (c) Weld center (d) Nugget, (e) TMAZ at RS, (f) HAZ at RS

#### 4.5.5

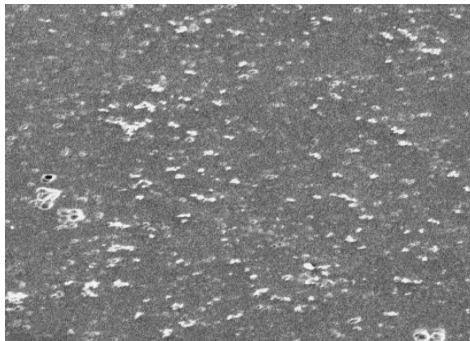
#### SEM Analysis of sample E4, 250x



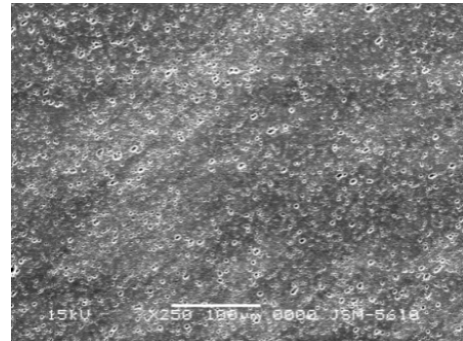
(a) HAZ at AS



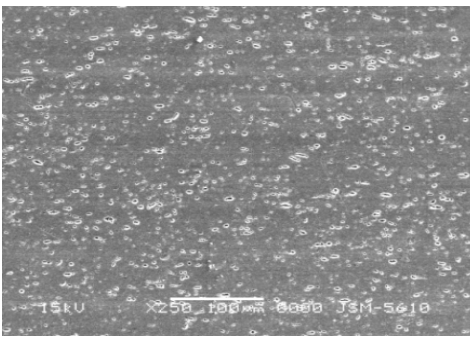
(b) TMAZ at AS



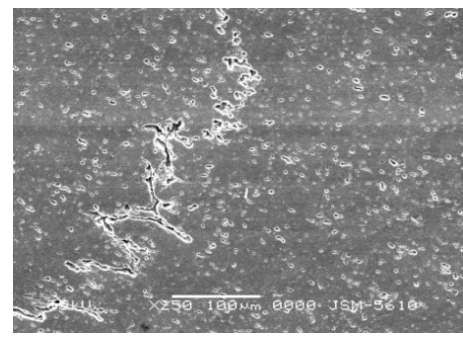
(c) Weld center



(d) Nugget



(e) TMAZ at RS



(f) HAZ at RS

Figure 4.42: SEM analysis of sample E4 at 250x (a) HAZ at AS, (b) TMAZ at AS, (c) Weld center, (d) Nugget, (e) TMAZ at RS, (f) HAZ at RS

#### **4.5.5d Observation of sample E4**

The Figure 4.40 and 4.41 shows the microstructure of sample E4 at 100x and 250x magnification while Figure 4.42 shows the SEM analysis for the sample E4

The weld center consists of the extremely fine and recrystallized grains of Al with breaking of coherent  $Mg_2Si$  precipitates. There is dynamically recrystallized grains are observed. The distribution of the precipitates is uniform throughout the weld center. At boundary between the weld center and TMAZ there is formation of oxide layer starting from bottom to top region of the weld.

In the TMAZ , the microstructure comprised of extremely fine grains of aluminum with extremely fine size precipitates of the  $Mg_2Si$ . In this case there are more precipitates free zones appears.

At boundary between the TMAZ and HAZ at the advancing side there is a formation of the nugget region.

The Nugget region consist of the fine, equiaxed grains with dark bands having higher density precipitates and the coarse grains of Al with light and low density  $Mg_2Si$  precipitates. Here the amount of the lighter band with lower density  $Mg_2Si$  precipitates is more.

The HAZ consist of the coarse grains of Al with precipitates of  $Mg_2Si$ . Here the precipitates free zones are more at both the side of HAZ but the HAZ at advancing side, the precipitates are near to each other compare to the retreating side.

4.5.6a Microstructure Analysis of sample E5, 100x

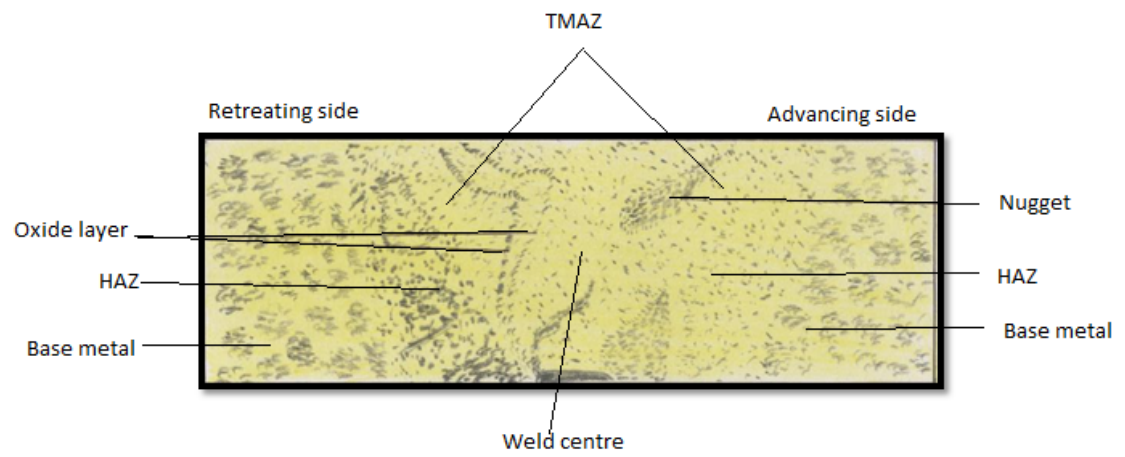


Figure 4.43: Microstructure of sample E5

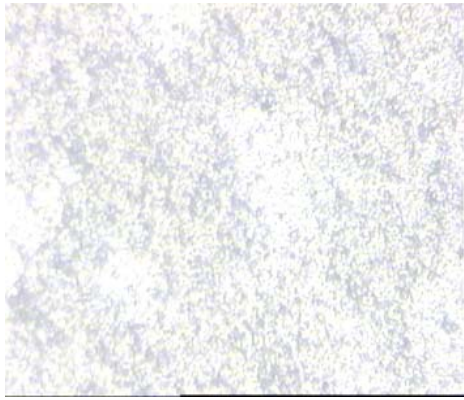
**4.5.6b Microstructure analysis of sample E5, 250x**



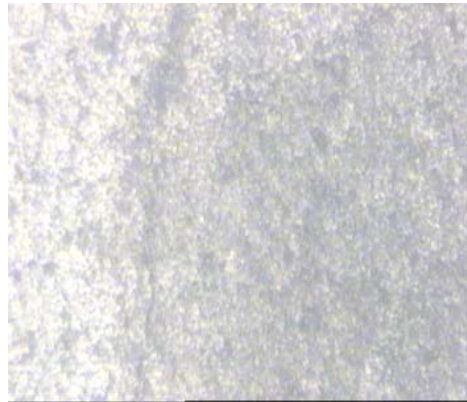
(a) HAZ at AS



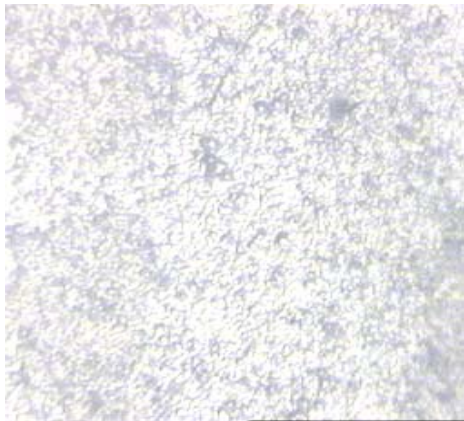
(b) TMAZ at AS



(c) Weld center



(d) Nugget



(e) TMAZ at RS

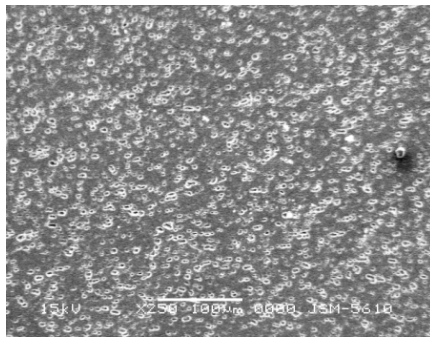


(f) HAZ at RS

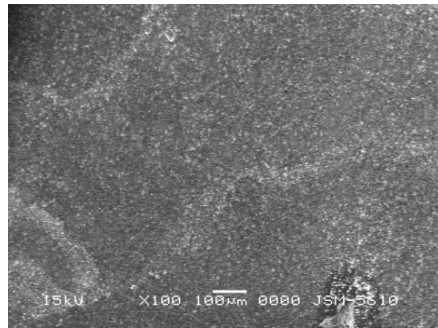
Figure 4.44: Microstructure analysis of sample E5 using Neophot at 250X (a) HAZ at AS, (b) TMAZ at AS, (c) Weld center, (d) Nugget, (e) TMAZ at RS, (f) HAZ at RS

4.5.6c

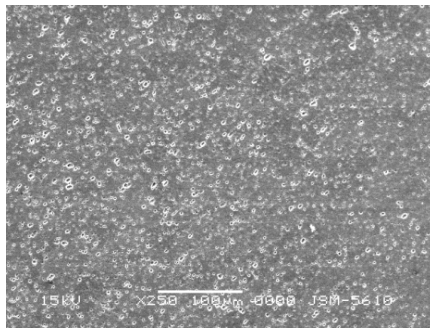
SEM Analysis of sample E5, 250x



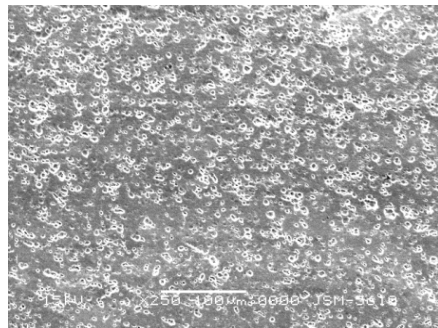
(a) HAZ at AS



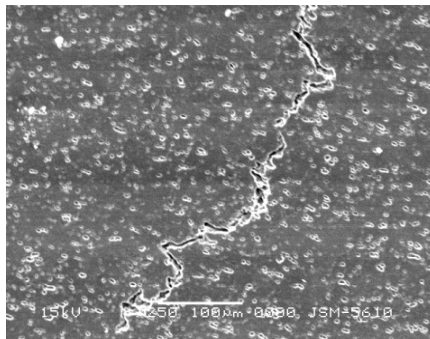
(b) TMAZ at AS



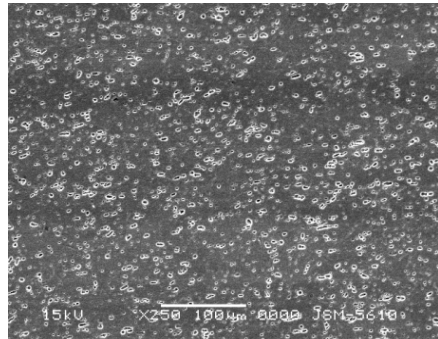
(c) Weld center



(d) Nugget



(e) TMAZ at RS



(f) HAZ at RS

Figure 4.45: SEM analysis of sample E5 at 250x (a) HAZ at AS, (b) TMAZ at AS, (c) Weld center, (d) Nugget, (e) TMAZ at RS, (f) HAZ at RS

#### **4.5.6d Observation of sample E5**

The Figure 4.43 and 4.44 shows the microstructure of sample E5 at 100x and 250x magnification while Figure 4.45 shows the SEM analysis for the sample E5.

The weld center consist of extremely fine recrystallized grains of Al with the breaking of the coherent precipitates of  $Mg_2Si$ .the size of the precipitates are extremely finer compare to the other zone of the weld. The distribution of the precipitates is uniform throughout the weld center region.

In the TMAZ, the microstructure consists of extremely fine grains of the Al with fine size of the precipitates of  $Mg_2Si$ . In this case there are presences of more precipitates free zones. At boundary near the TMAZ and weld center, there is formation of an oxide layer.

The nugget region consist of the extremely fine, equiaxed grains with dark bands with heavy density precipitates and the coarse grains of Al with light bands with low precipitates density of  $Mg_2Si$ . In this case the nugget consists of very least lighter bands than that of the dark bands. The size of the nugget is big, which may be due to the higher heat input.

The microstructure of HAZ at advancing side consist of the fine grains of Al with fine size of precipitates of  $Mg_2Si$ .the reason behind the fine grain structure may be the advancing side of the weld cool faster than the retreating side. In the HAZ at retreating side, the microstructure consists of the coarse grains of al with coarse precipitates of  $Mg_2Si$ . The grain growth was observed and the precipitates free zones are also presence in the both side of HAZ.

**4.5.7a Microstructure Analysis of sample E6, 100x**

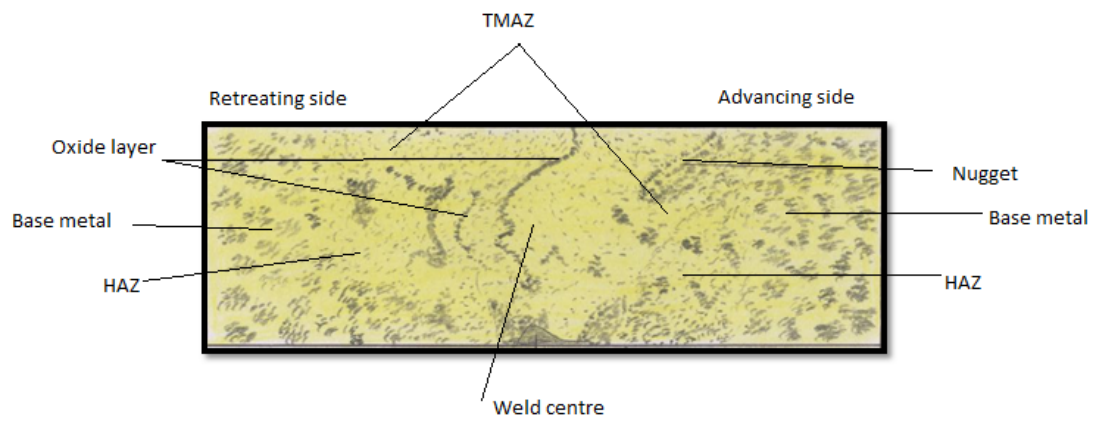
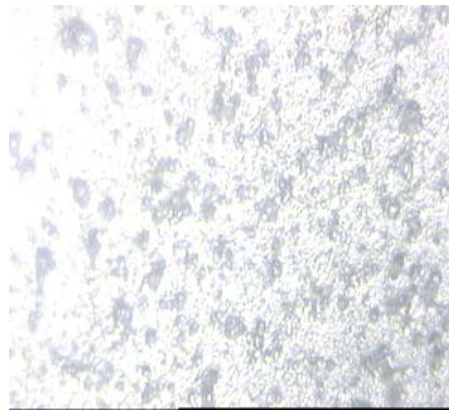


Figure 4.46: Microstructure of sample E6

**4.5.7b Microstructure analysis of sample E6, 250x**



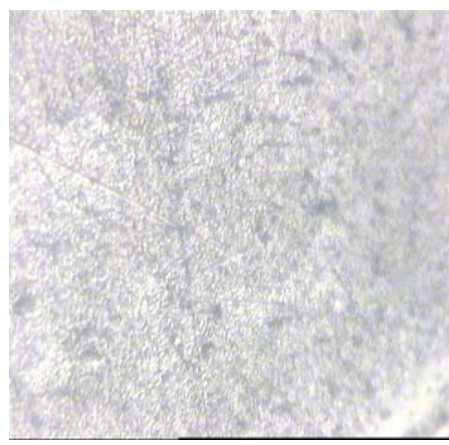
(a) HAZ at AS bottom



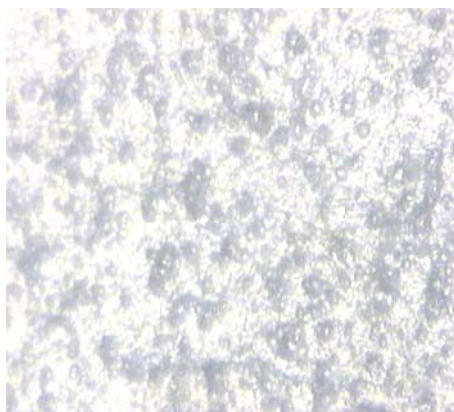
(b) TMAZ at AS



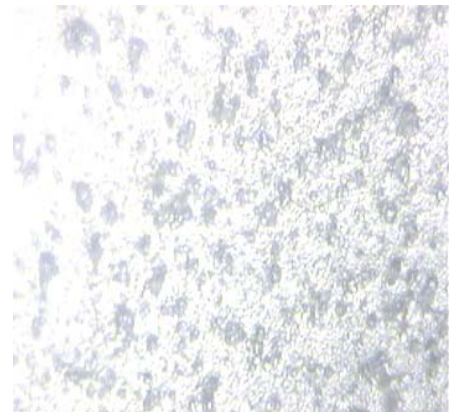
(c) Nugget



(d) Weld center



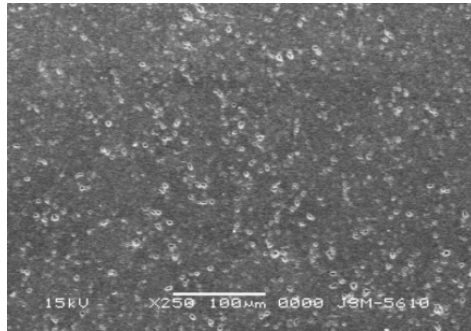
(e) HAZ at RS bottom



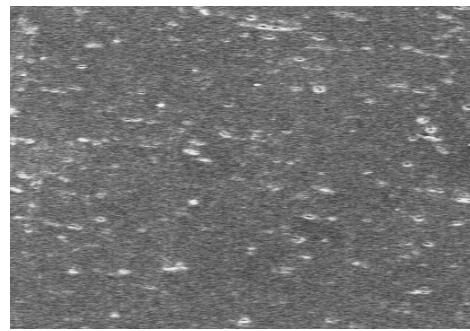
(f) TMAZ at RS

Figure 4.47: Microstructure analysis of sample E6 using Neophot at 250x. (a) HAZ at AS, (b) TMAZ at AS, (c) Nugget, (d) Weld center, (e) HAZ at RS, (f) TMAZ at RS

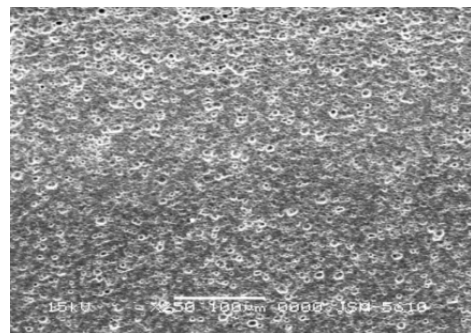
**4.5.7c SEM Analysis of sample E6, 250x**



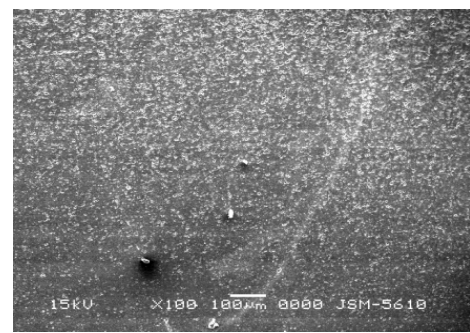
(a) HAZ at AS



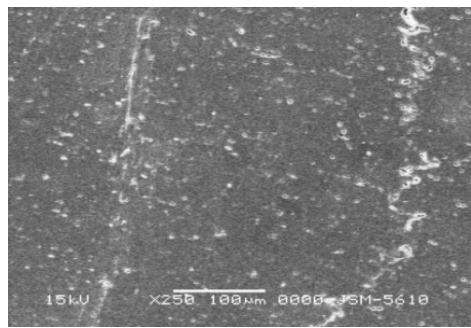
(b) TMAZ at AS



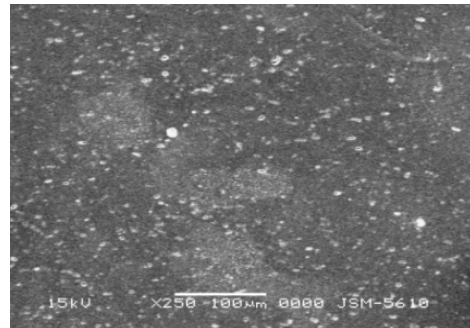
(d) Nugget



(c) Weld center



(e) TMAZ at RS



(f) HAZ at RS

Figure 4.48: SEM analysis of sample E6 at 250x. (a) HAZ at AS, (b) TMAZ at AS, (c) Weld center, (d) Nugget, (e) TMAZ at RS, (f) HAZ at RS

#### **4.5.7d Observation of sample E6**

The Figure 4.46 and 4.47 shows the microstructure of sample E6 at 100x and 250x magnification while Figure 4.48 shows the SEM analysis for the sample E6.

The weld center consists of extremely fine grain structure of Al with extremely fine size of broken  $Mg_2Si$  precipitates. The dynamic recrystallization was observed. In the center of weld, due to the stirring action of the tool, the breaking of the precipitates was occurred and it was distributed evenly in the weld center region.

The TMAZ consist of the fine grains of the Al with ripen precipitates of  $Mg_2Si$ . there is also formation of the precipitates free zones, the precipitates are near to each other.

In the nugget region the microstructure consist of the fine, equiaxed grains of Al with high density precipitates of the  $Mg_2Si$ , which was indicated by the dark bands. & the coarse grains of Al with lower density of precipitate indicated by the lighter bands. The structure say to be the onion ring structure. The size of the nugget was big.

The microstructures of HAZ at the bottom of advancing side comprised of the coarse grains of Al with enrich precipitates of the  $Mg_2Si$ . The microstructures become finer with moving towards the top of the HAZ the precipitates free zone are less.

The HAZ at retreating side comprised of the coarse grains of Al with enrich precipitates of  $Mg_2Si$  and it becomes finer with moving towards the top surface of the HAZ. In the top region, there is more precipitates free zones are present.

**4.5.8a Microstructure Analysis of sample E7, 100x**

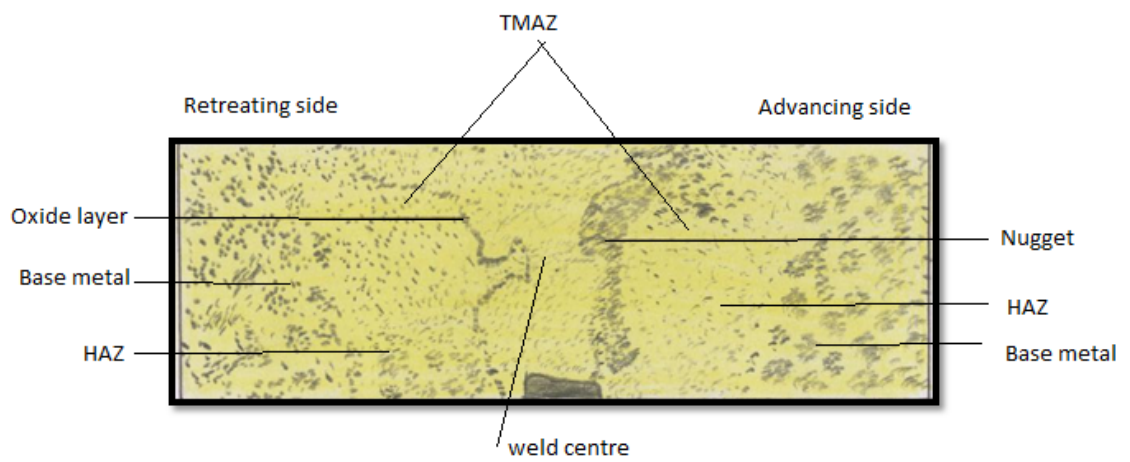
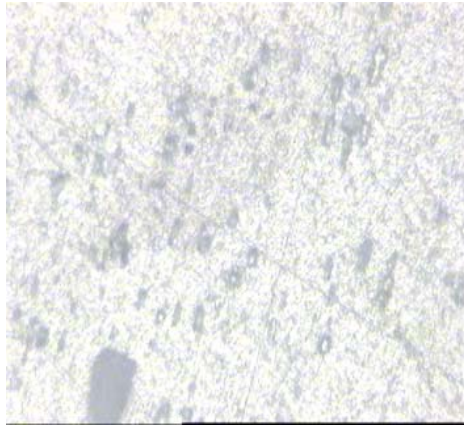
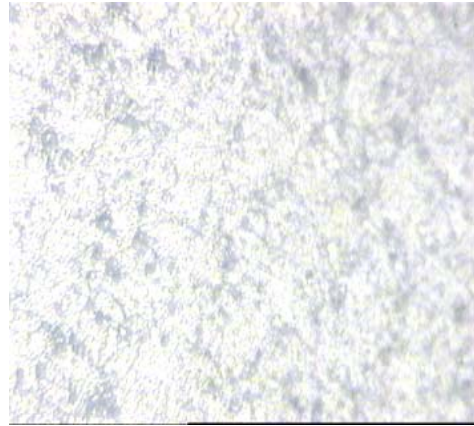


Figure 4.49: Microstructure of sample E7

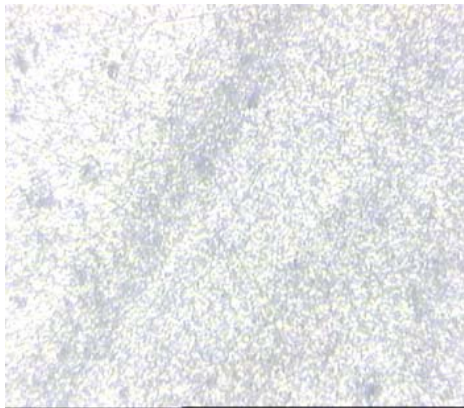
**4.5.8b Microstructure analysis of sample E7, 250x**



(a) HAZ at AS



(b) TMAZ at AS



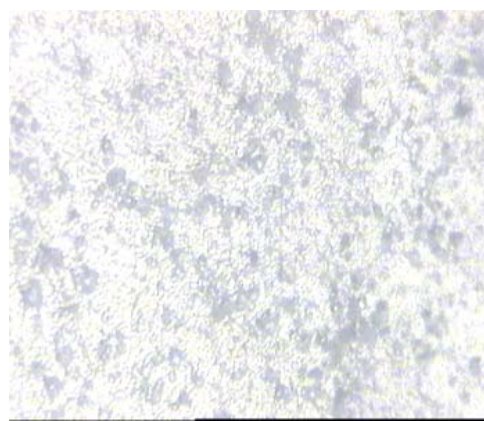
(d) Nugget



(c) Weld center



(e) TMAZ at RS

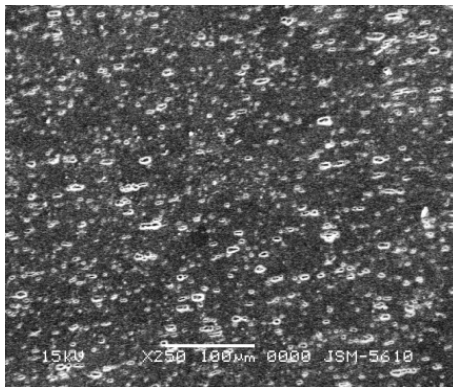


(f) HAZ at RS

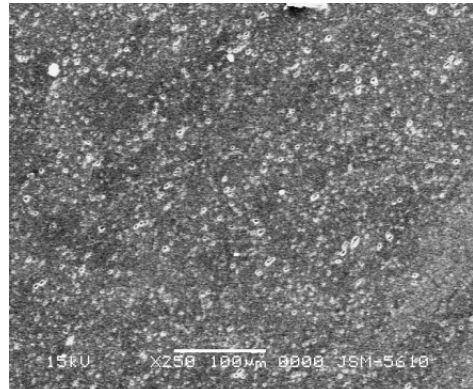
Figure 4.50: Microstructure analysis of sample E7 using Neophot at 250X. (a) HAZ at AS, (b) TMAZ at AS, (c) Weld center, (d) Nugget, (e) TMAZ at RS, (f) HAZ at RS

4.5.8c

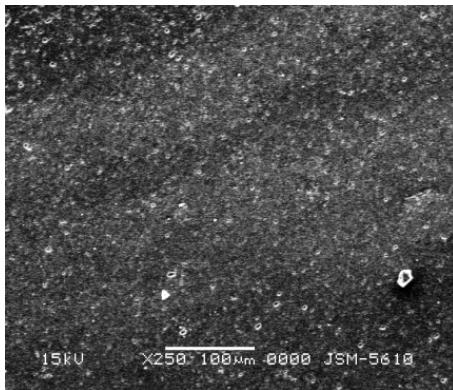
SEM Analysis of sample E7, 250x



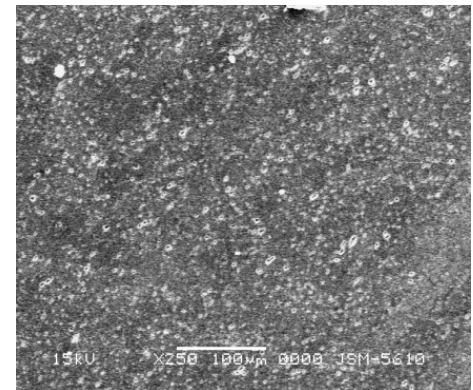
(a) HAZ at AS



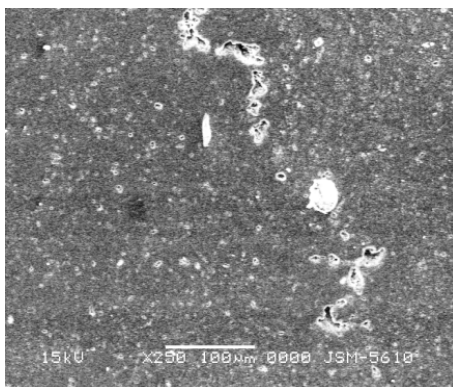
(b) TMAZ at AS



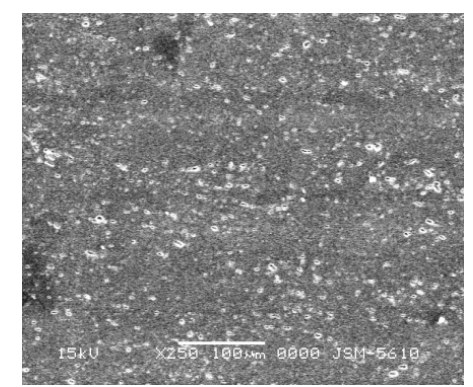
(d) Nugget



(c) Weld center



(e) TMAZ at RS



(f) HAZ at RS

Figure 4.51: SEM analysis of sample E7 at 250x. (a) HAZ at AS, (b) TMAZ at AS, (c) Weld center, (d) Nugget, (e) TMAZ at RS, (f) HAZ at RS

#### **4.5.8d            Observation of sample E7**

The Figure 4.49 and 4.50 shows the microstructure of sample E7 at 100x and 250x magnification while Figure 4.51 shows the SEM analysis for the sample E7.

In The weld center, the microstructure consists of the extremely fine and dynamically recrystallized grains with broken  $Mg_2Si$  precipitates. The reprecipitation also observed the precipitates are distributed evenly throughout the weld center region.

In the TMAZ, the microstructure consists of fine grains of Al with extremely fine precipitates of  $Mg_2Si$ . There is also formation of the precipitates free zone in the TMAZ.

At boundary between the HAZ and TMAZ there is formation of oxide layer. It may be the oxide of aluminum.

The nugget region consist of the extremely fine, equiaxed grains with the precipitates of the higher density with dark bands and coarse grains with precipitates of lower density indicated by lighter bands. There is sharp boundary between the nugget and its surrounding region. The size of the nugget was big.

The HAZ at advancing side consist of the fine grains of Al with precipitates of  $Mg_2Si$  compare to the HAZ of Retreating side of the weld. At retreating side, there is presence of enrich precipitates of  $Mg_2Si$ .

**4.5.9a Microstructure Analysis of sample E8, 100x**

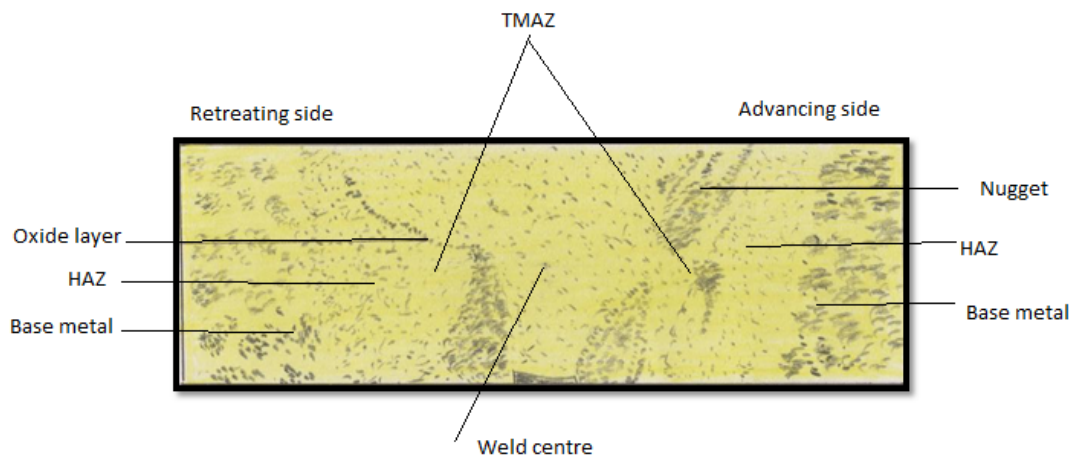
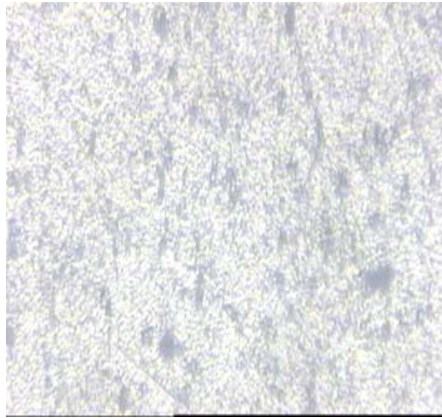
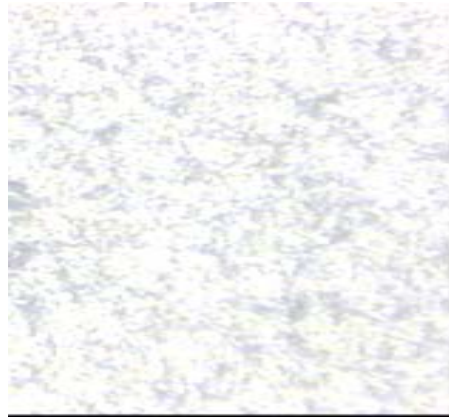


Figure 4.52: Microstructure of sample E8

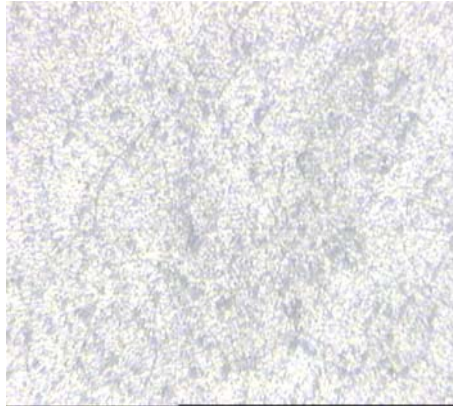
**4.5.9b Microstructure analysis of sample E8, 250x**



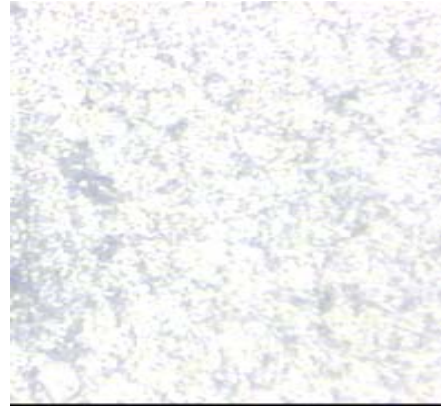
(a) HAZ at AS



(b) TMAZ at AS



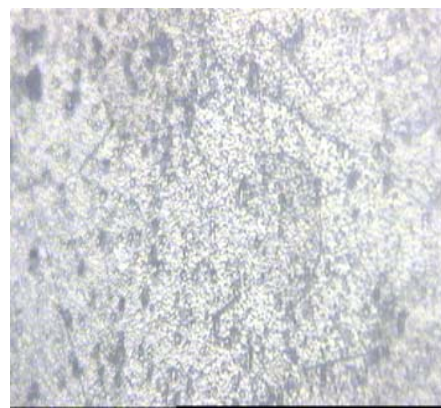
(d) Nugget



(c) Weld center



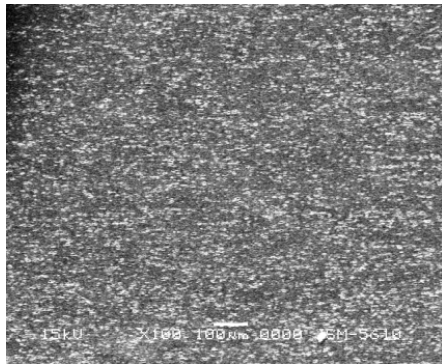
(e) TMAZ at RS



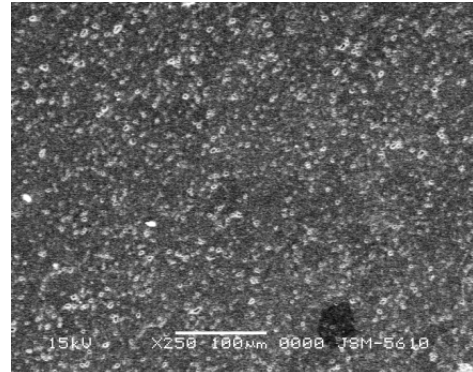
(f) HAZ at RS

Figure 4.53: Microstructure analysis of sample E8 using Neophot at 250X. (a) HAZ at AS, (b) TMAZ at AS, (c) Weld center, (d) Nugget, (e) TMAZ at RS, (f) HAZ at RS

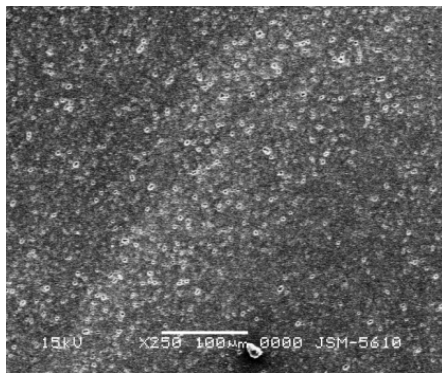
**4.5.9c SEM Analysis of sample E8, 250x**



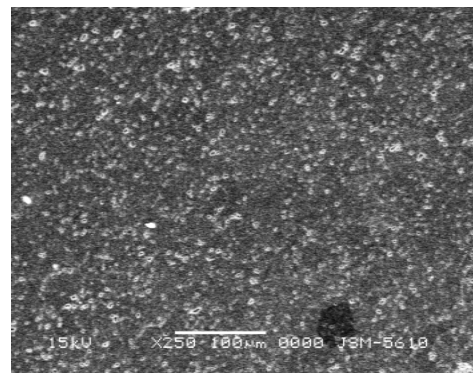
(a) HAZ at AS



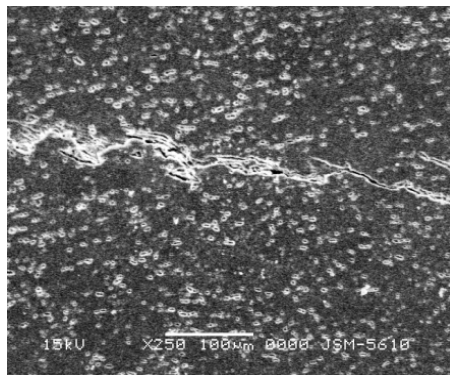
(b) TMAZ at AS



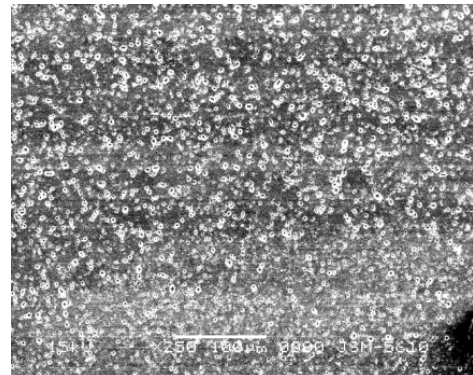
(d) Nugget



(c) Weld center



(e) TMAZ at RS



(f) HAZ at RS

Figure 4.54: SEM analysis of sample E8 at 250x. (a) HAZ at AS, (b) TMAZ at AS, (c) Weld center, (d) Nugget, (e) TMAZ at RS, (f) HAZ at RS

#### **4.5.9d Observation of sample E8**

The Figure 4.52 and 4.53 shows the microstructure of sample E8 at 100x and 250x magnification while Figure 4.54 shows the SEM analysis for the sample E8.

In the weld center, the thermal dissolution of precipitates takes place due to the heat generation during stirring action of the tool. There is also re precipitation occurred .The microstructure consist of the extremely fine recrystallized grains of Al with broken coherent precipitates of  $Mg_2Si$ . The distribution of the broken precipitates is even throughout the weld center.

In TMAZ the microstructure consist of the fine grains with extremely fine size of precipitates of the  $Mg_2Si$ . In this case there was no presence of the ripen precipitates. There is also presence of the precipitates free zones.

In the nugget region the microstructure consist of the onion ring structure with fine, equiaxed grains with dark bands of higher density precipitates of  $Mg_2Si$  and the coarse grains with lower precipitates density of  $Mg_2Si$  with lighter bands.

There is sharp boundary observed between the Nugget and surrounding region.

The HAZ at advancing and retreating side consist of the fine grains of Al with large precipitates of  $Mg_2Si$  compare to TMAZ. The distribution of precipitates is even throughout the HAZ region.

**4.5.10a      Microstructure Analysis of sample E9, 100x**

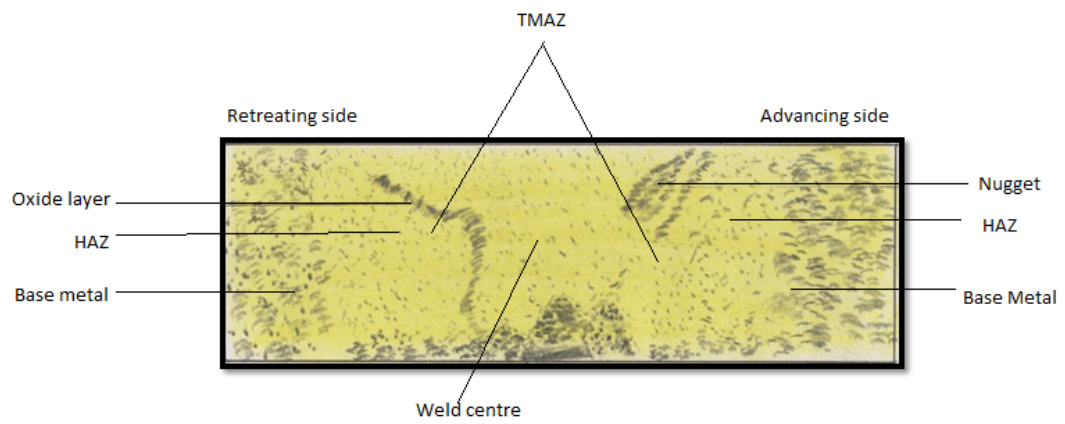
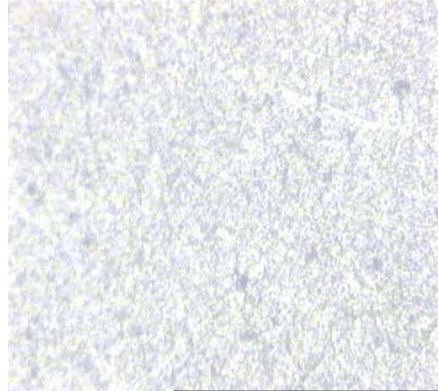


Figure 4.55: Microstructure of sample E9

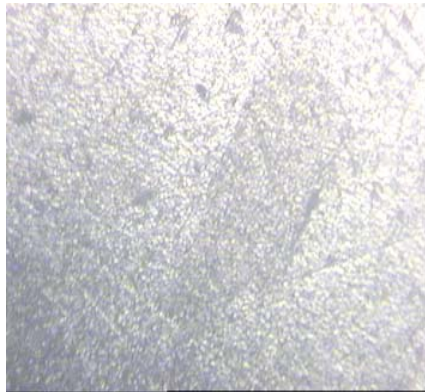
**4.5.10b Microstructure analysis of sample E9, 250x**



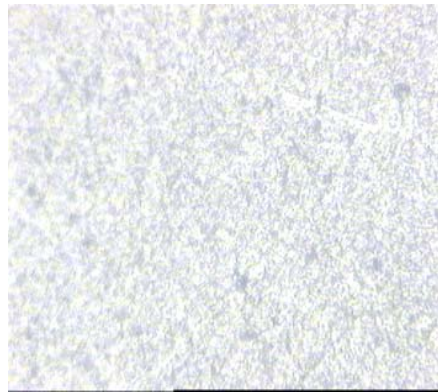
(a) HAZ at AS



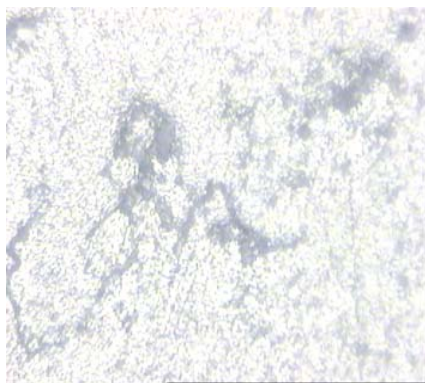
(b) TMAZ at AS



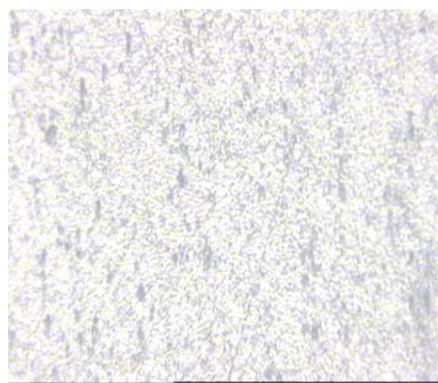
(c) Nugget



(d) Weld center



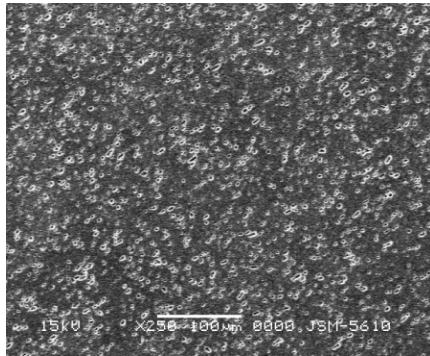
(e) TMAZ at RS



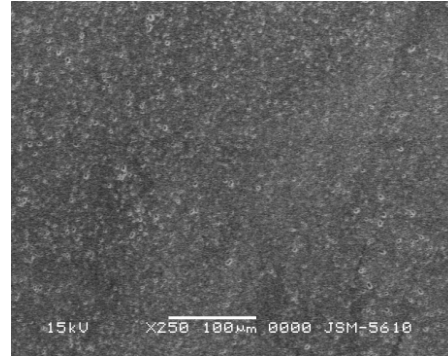
(f) HAZ at RS

Figure 4.56: Microstructure analysis of sample E9 using Neophot at 250x. (a) HAZ at AS, (b) TMAZ at AS, (c) Nugget, (d) Weld center, (e) TMAZ at RS, (f) HAZ at RS

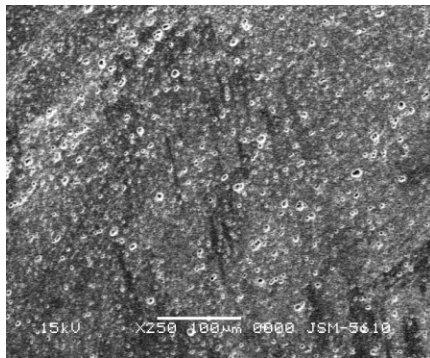
**4.5.10c SEM Analysis of sample E9, 250x**



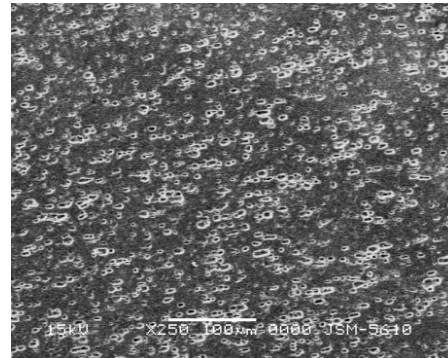
(a) HAZ at AS



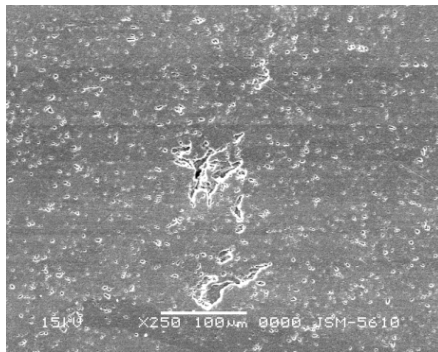
(b) TMAZ at AS



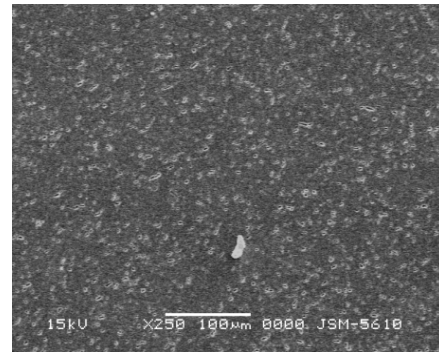
(c) Nugget



(d) Weld center



(e) TMAZ at RS



(f) HAZ at RS

Figure 4.57: SEM analysis of sample E9 at 250x. (a) HAZ at AS, (b) TMAZ at AS, (c) Nugget, (d) Weld center, (e) TMAZ at RS, (f) HAZ at RS

#### **4.5.10d Observation of sample E9**

The figure 4.55 and 4.56 shows the microstructure of sample E9 at 100x and 250x magnification while figure 4.57 shows the SEM analysis for the sample E9.

In the weld center, due to the stirring action of the tool, plastic deformation was taken place and there is generation of heat due to the friction which lead to the thermal dissolution of the  $Mg_2Si$  precipitates. There is also re precipitation take place. The microstructure consist of the fine, equiaxed recrystallized grains of Al with the broken precipitates of the  $Mg_2Si$ . It was distributed evenly throughout the weld center region.

In the TMAZ the microstructure consist of the fine grains of Al with fine size precipitates of  $Mg_2Si$ . There is also formation of precipitates free zones in the TMAZ.

The nugget comprise of fine, equiaxed grains of Al with the dark bands of the high density precipitates and coarse grains of the lower precipitates density with light bands. The structure is said to be the onion ring structure or say banded structure.

The HAZ at advancing side consist of the fine grains of Al with fine and coarse precipitates of  $Mg_2Si$ . In the HAZ at retreating side, the microstructure consists of the fine grains of Al with fine precipitates of  $Mg_2Si$ . There is also formation of precipitates free zone.

**4.5.11a      Microstructure Analysis of sample E10, 100x**

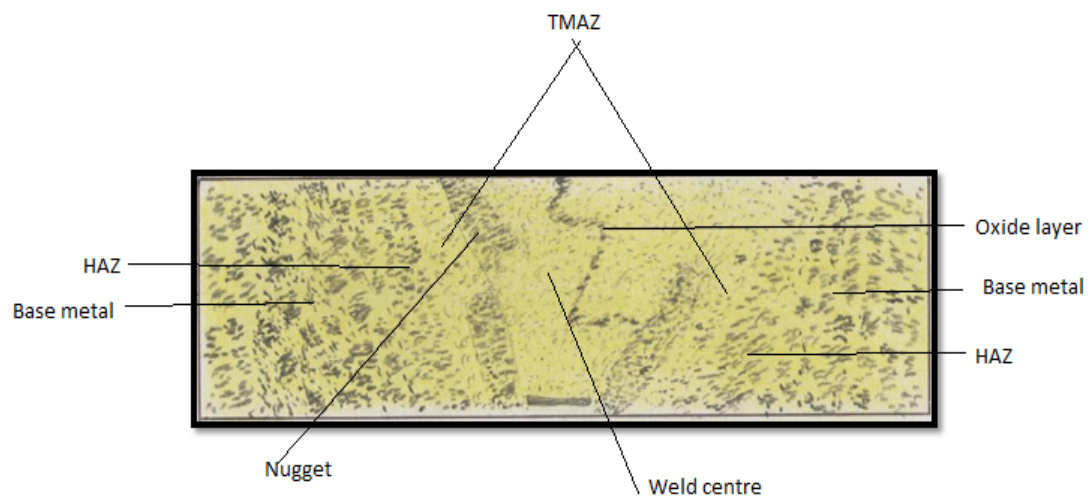
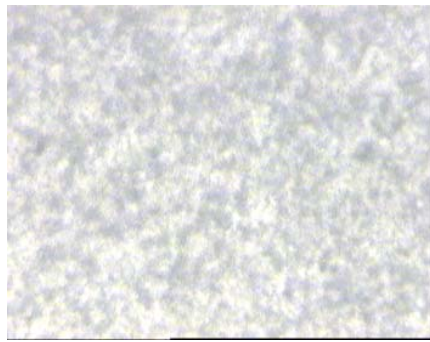
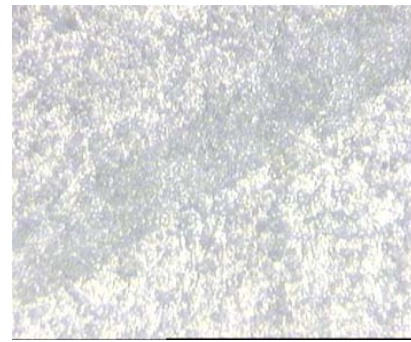


Figure 4.58: Microstructure of sample E10

**4.5.11b      Microstructure analysis of sample E10, 250x**



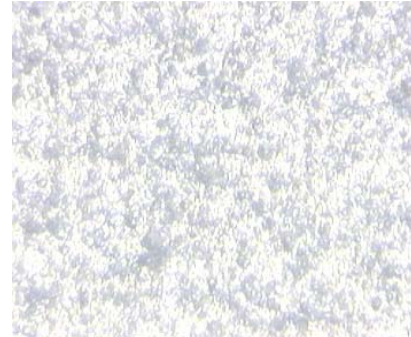
(a) HAZ at AS



(b) HAZ -TMAZ at AS



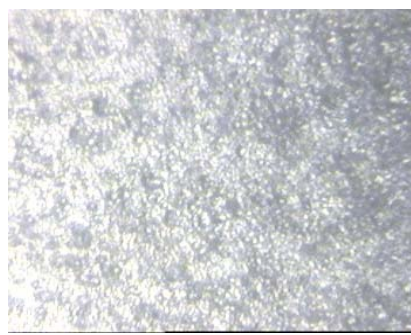
(c) Nugget



(d) Weld center



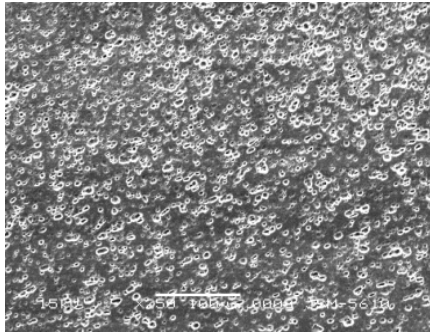
(e) TMAZ at RS



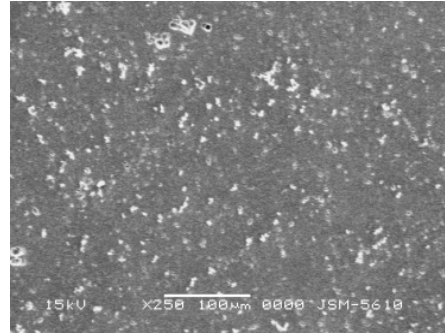
(f) HAZ at RS

Figure 4.59: Microstructure analysis of sample E10. (a) HAZ at AS, (b) HAZ -TMAZ at AS, (c) Nugget, (d) Weld center, (e) TMAZ at RS, (f) HAZ at RS

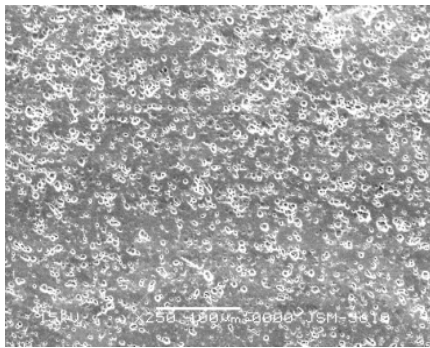
**4.5.11c SEM Analysis of sample E10, 250x**



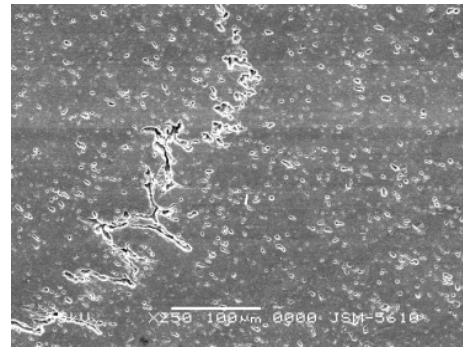
(a) HAZ at AS



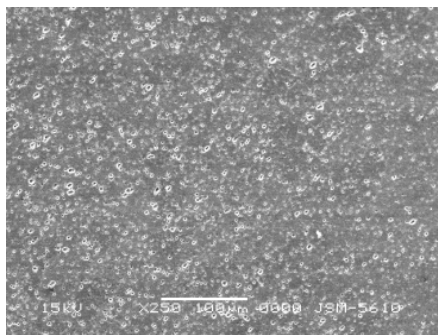
(b) TMAZ at AS



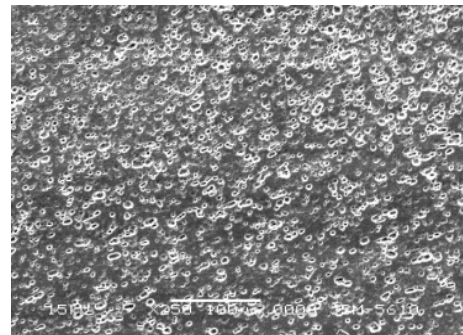
(c) Nugget



(d) Weld center



(e) TMAZ at RS



(f) HAZ at RS

Figure 4.60: SEM analysis of sample E10. (a) HAZ at AS, (b) TMAZ at AS, (c) Nugget, (d) Weld center, (e) TMAZ at RS, (f) HAZ at RS

#### **4.5.11d          Observation of sample E10**

The figure 4.58 and 4.59 shows the microstructure of sample E10 at 100x and 250x magnification while figure 4.60 shows the SEM analysis for the sample E10

In the weld center region ,the microstructure consist of the fine, recrystallized grains of Al with presence of broken precipitates of  $Mg_2Si$ .the thermal dissolution of the precipitates and reprecipitation was also observed.

There was also formation of oxide layer in the weld center region. It may be the oxide of aluminum.

In the TMAZ the microstructure comprised of fine grains with ripen precipitates of  $Mg_2Si$ .there is also formation of the precipitates free zone.

In the nugget region the microstructure consist of the banded structure. The dark band indicates the fine grain structure with heavy density if precipitates and coarse grains with low precipitate density by lighter bands. The amounts of dark bands are higher than the lighter bands.

The HAZ at both side advancing as well as retreating side consist of the coarse grains of Al with presence of the  $Mg_2Si$  precipitates. The formation of precipitates free zone is less.

4.5.12a Microstructure Analysis of sample E11, 100x

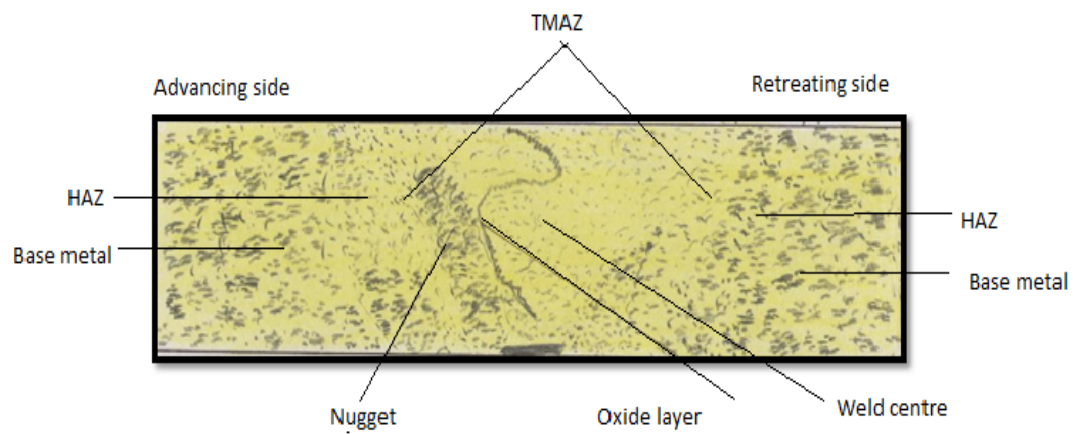
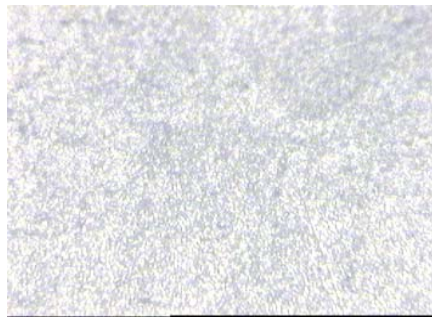
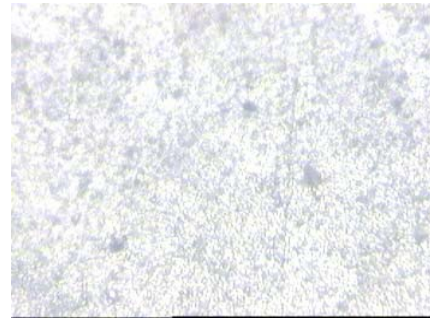


Figure 4.61: Microstructure of sample E11

**4.5.12b      Microstructure analysis of sample E11, 250x**



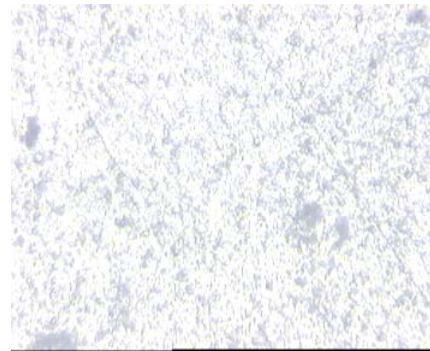
(a) HAZ at AS



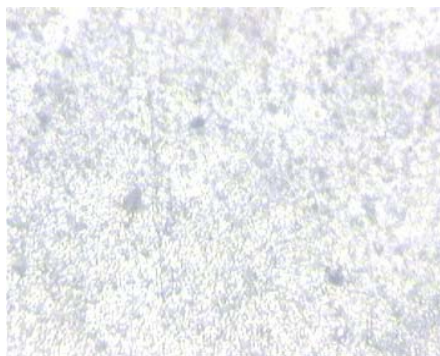
(b) TMAZ at AS



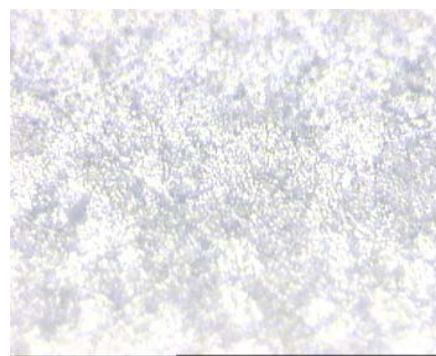
(c) Nugget



(d) Weld center



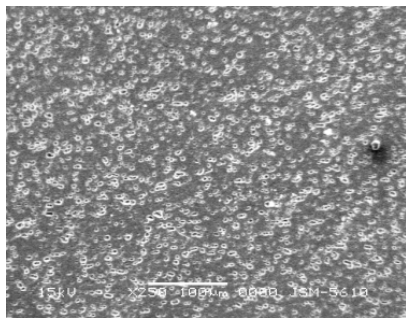
(e) TMAZ at RS



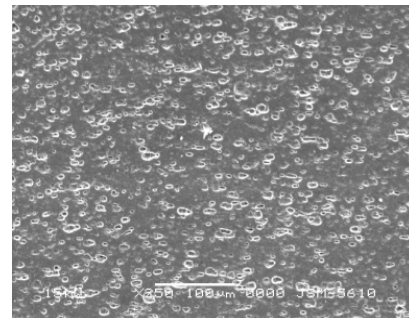
(f) HAZ at RS

Figure 4.62: Microstructure analysis of sample E11 (a) HAZ at AS, (b) TMAZ at AS, (c) Nugget, (d) Weld center, (e) TMAZ at RS, (f) HAZ at RS

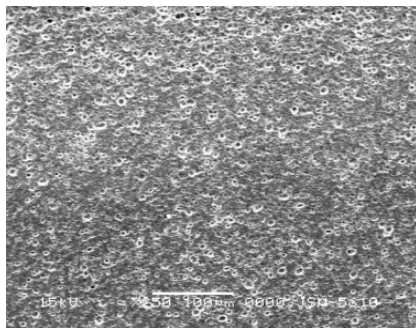
**4.5.12c SEM Analysis of sample E11, 250x**



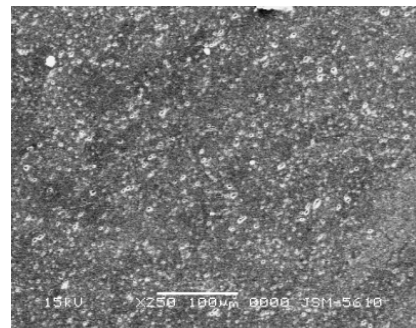
(a) HAZ at AS



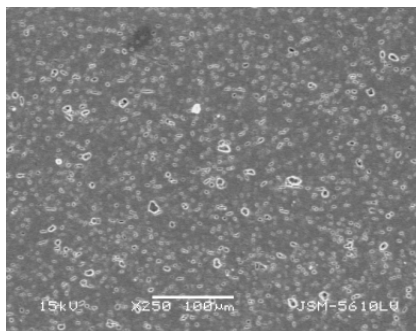
(b) TMAZ at AS



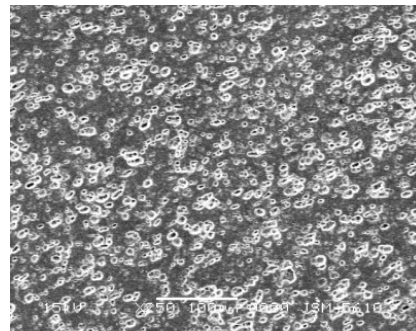
(c) Nugget



(d) Weld center



(e) TMAZ at RS



(f) HAZ at RS

Figure 4.63: SEM analysis of sample E11 (a) HAZ at AS, (b) TMAZ at AS, (c) Nugget, (d) Weld center, (e) TMAZ at RS, (f) HAZ at RS

#### **4.5.12d Observation of sample E11**

The figure 4.61 and 4.62 shows the microstructure of sample E11 at 100x and 250x magnification while figure 4.63 shows the SEM analysis for the sample E11.

In the weld center region ,the microstructure consist of the fine, recrystallized grains of Al with presence of broken precipitates of  $Mg_2Si$ .the thermal dissolution of the precipitates and reprecipitation was also observed.

There is also formation of oxide layer starting from bottom center of weld to top end of the weld. It may be the oxide of the aluminum.

In the TMAZ, microstructure consists of the fine grains with presence of the  $Mg_2Si$  precipitates there is also presence of the precipitates free zones.

The nugget consists of the alternate layers of the fine and coarse grains. The dark bands indicated the fine and equiaxed grains of aluminum with the heavy density of precipitates while lighter band indicates the coarse grains with the lower precipitates density. The amounts of dark bands are higher than that of the lighter bands

In the HAZ, at the advancing side, the microstructure possess the coarse grain structure at the bottom region while fine grain structure at the top portion with presence of  $Mg_2Si$  precipitates. The microstructure at retreating side possess the fine grains of Al with presence of finer precipitates.

4.5.13a Microstructure Analysis of sample E12, 100x

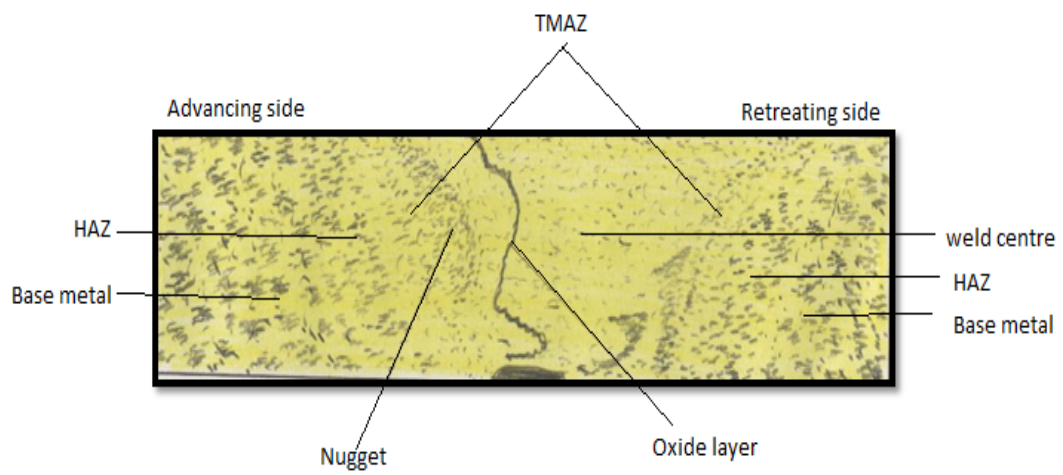
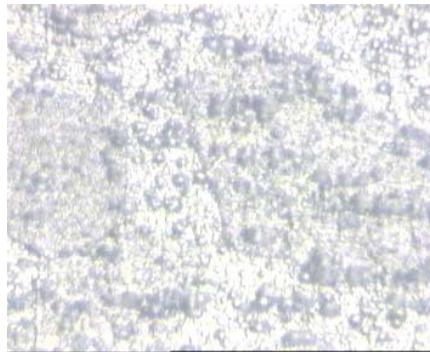
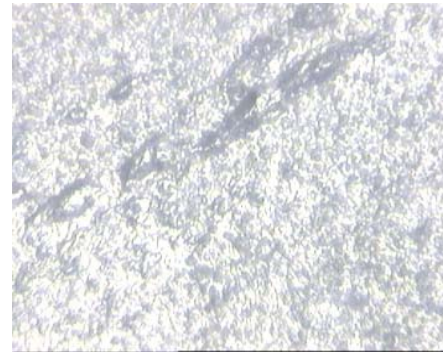


Figure 4.64: Microstructure of sample E12

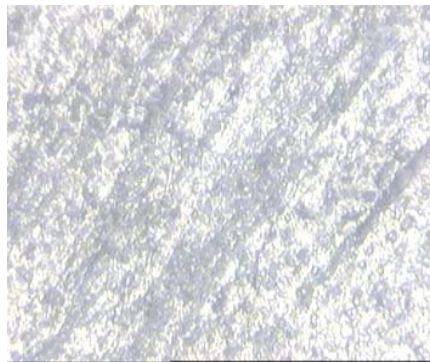
**4.5.13b      Microstructure analysis of sample E12, 250x**



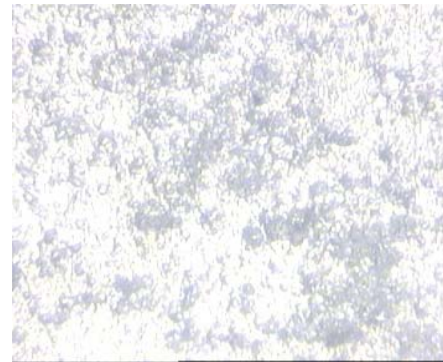
(a) HAZ at AS



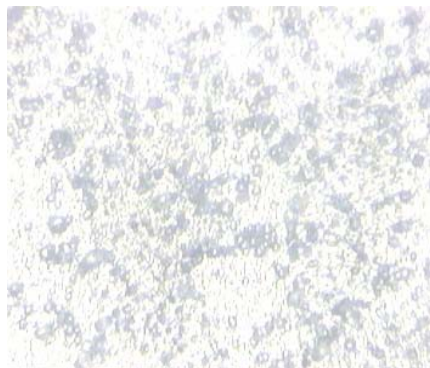
(b) TMAZ at AS



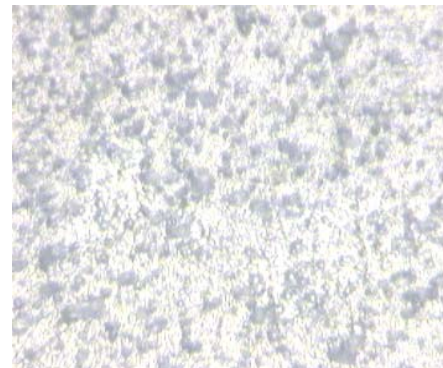
(c) Nugget



(d) Weld center



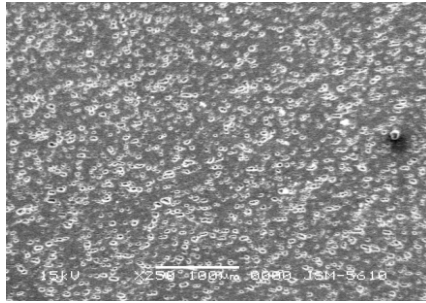
(e) TMAZ at RS



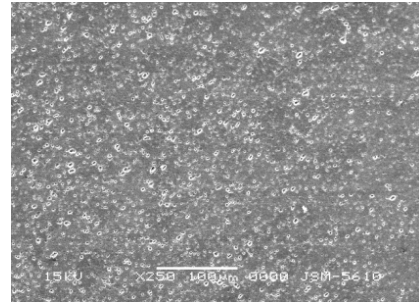
(f) HAZ at RS

Figure 4.65: Microstructure analysis of sample E12. (a) HAZ at AS, (b) TMAZ at AS, (c) Nugget, (d) Weld center, (e) TMAZ at RS, (f) HAZ at RS

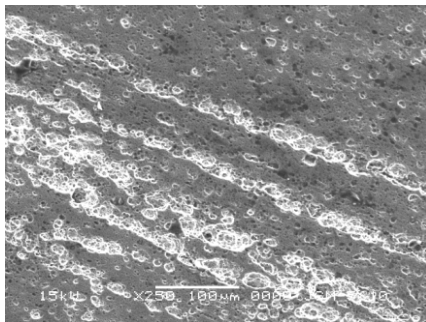
**4.5.13c SEM Analysis of sample E12, 250x**



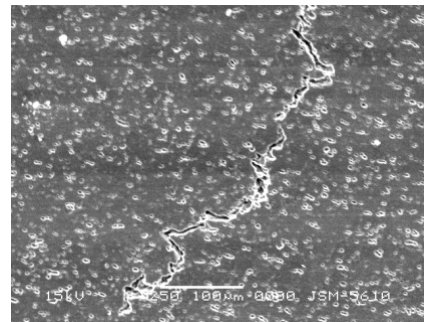
(a) HAZ at AS



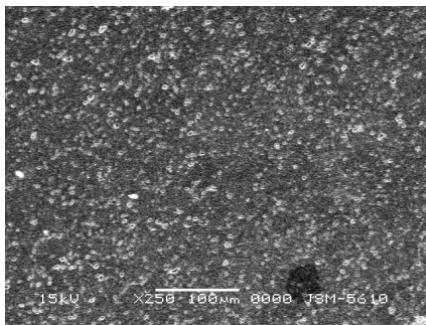
(b) TMAZ at AS



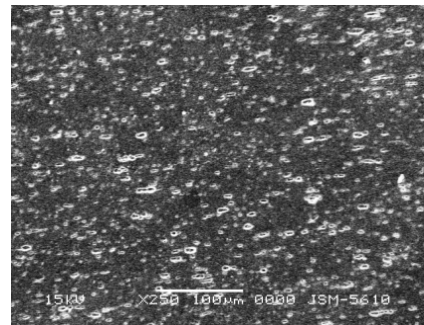
(c) Nugget



(d) Weld center



(e) TMAZ at RS



(f) HAZ at RS

Figure 4.66: SEM analysis of sample E12. (a) HAZ at AS, (b) TMAZ at AS, (c) Nugget, (d) Weld center, (e) TMAZ at RS, (f) HAZ at RS

#### **4.5.13d            Observation of sample E12**

The figure 4.64 and 4.65 shows the microstructure of sample E12 at 100x and 250x magnification while figure 4.66 shows the SEM analysis for the sample E12.

In the weld center region, the microstructure consists of the fine, recrystallized grains of Al with presence of broken precipitates of  $Mg_2Si$ . The thermal dissolution of the precipitates and reprecipitation was also observed. The distribution of precipitates was uniform.

There was also formation of oxide layer in the weld center region. It may be the oxide of aluminum.

The TMAZ possess the fine grain structure with presence of the ripen precipitates. It also comprised of the precipitates free zones.

The nuggets consist of the alternate layers of the fine and coarse grains. The dark bands indicated the fine and equiaxed grains of aluminum with the heavy density of precipitates while lighter band indicates the coarse grains with the lower precipitates density. The amount of dark bands is higher than that of the lighter bands.

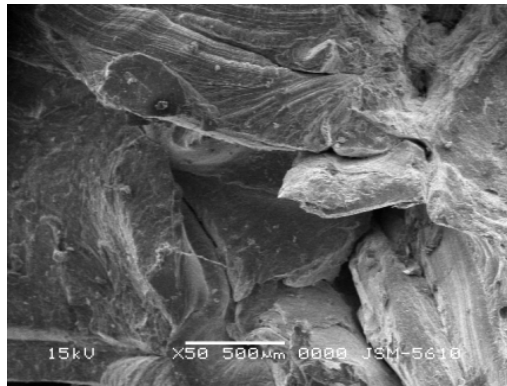
In the HAZ at advancing as well as retreating side possess the coarse grains of Al with presence of  $Mg_2Si$  precipitates. The amount of precipitates free zone is less.

## **4.6 FRACTOGRAPHY OF TENSILE SPECIMEN FOR CFSW SAMPLES**

Fractography is understood to mean "the study of fracture surfaces". In failure analysis, fractography is a vital tool used to determine a failure mode. The Scanning Electron Microscope (SEM) is often the choice instrument used to examine the surface of a failed material. When materials break in a brittle manner, they usually exhibit a crystalline or brittle appearing fracture. Likewise, when a ductile material is fractured, the fracture surface usually exhibits elongated dimples. Materials fail for different reasons, but they fracture by four principal modes: fatigue, cleavage, dimple rupture, and de-cohesive rupture. Each of these modes has its own characteristic fracture appearance.

Examination of the tensile fracture surfaces of the base and FSWAA6101 was done at low magnification as well as at higher magnification in order to identify the fracture mechanisms.

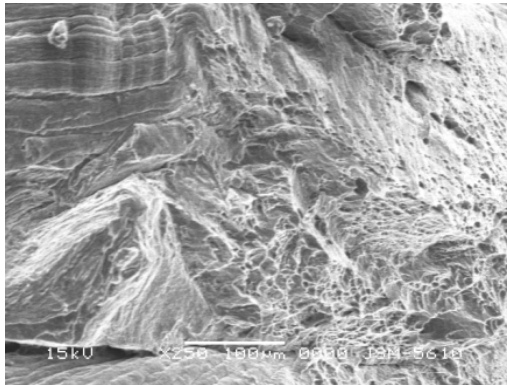
#### 4.6.1 Fractography of Tensile specimen E1A



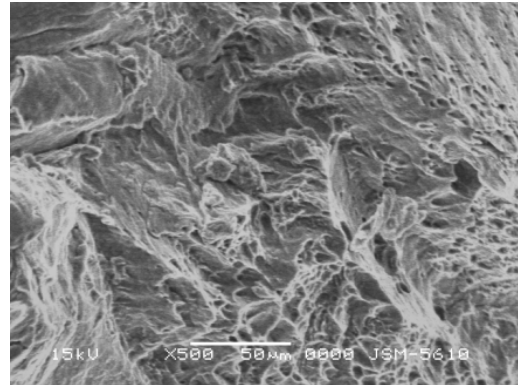
(a) 50x



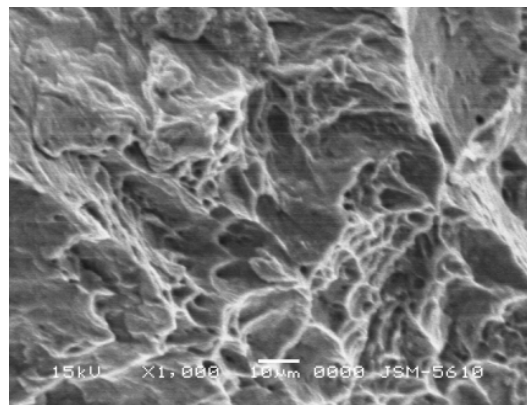
(b) 100x



(c) 250x



(d) 500x



(e) 1000x

Figure 4.67: SEM images of tensile fracture surface of AA6101 T6, hexagonal pin, and concave shoulder tool, at 545 rpm, 50mm/min, and welded parallel to rolling direction (E1A)

**Observation:** The fracture surface indicates the mixed mode fracture of ductile and brittle. In some of the region fibrous structure appears.

## 4.6.2 Fractography of Tensile specimen E6

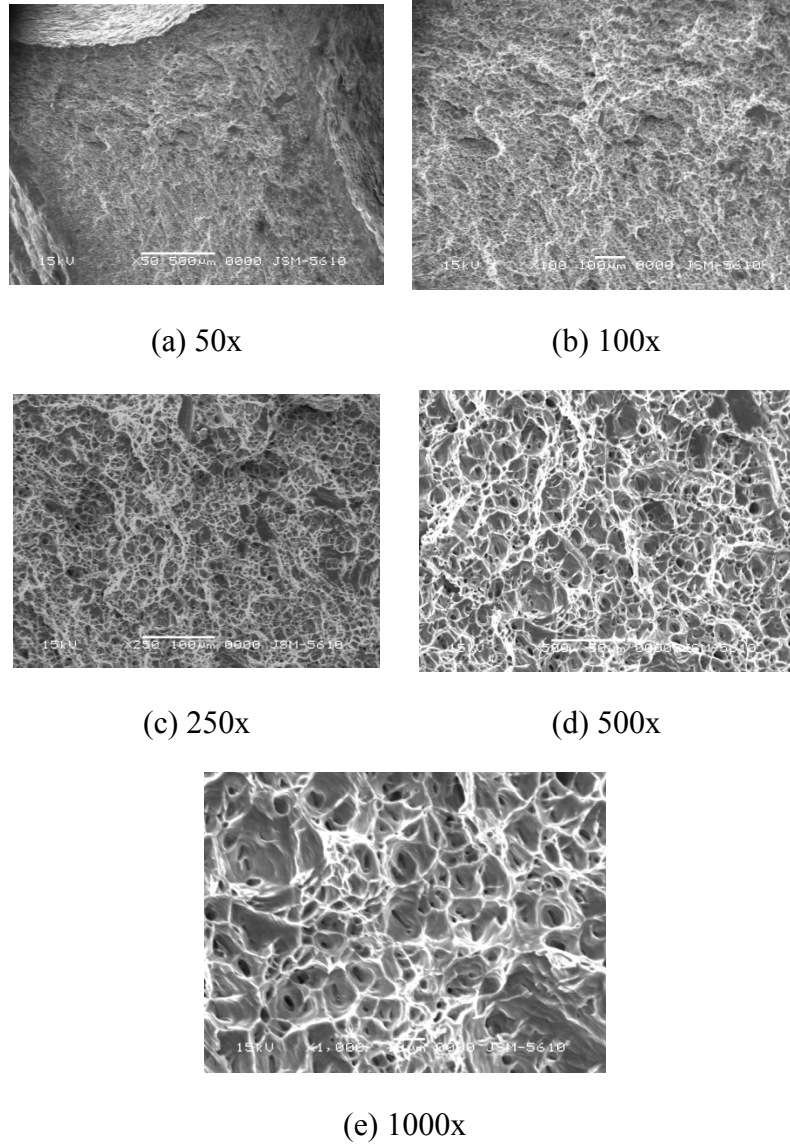


Figure 4.68: SEM images of tensile fracture surface of AA6101 T6, hexagonal pin, concave shoulder tool, at 765 rpm, 120mm/min (E6)

**Observation:** The fracture surface indicated the pure ductile failure of the weld sample. The fracture surfaces consist of the pure dimple structure in the elongated form.

### 4.6.3 Fractography of Tensile specimen E8

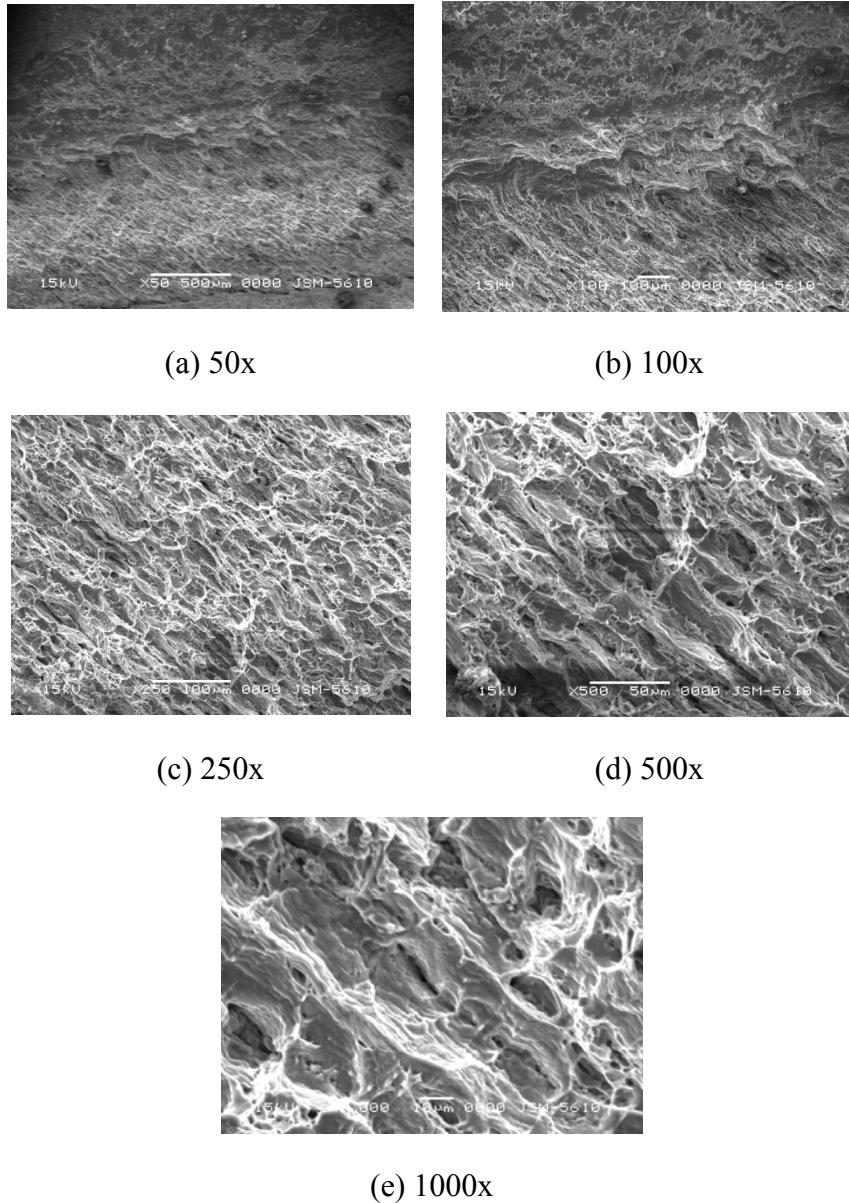
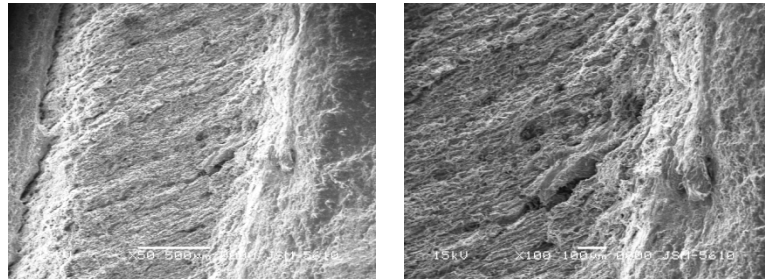


Figure 4.69: SEM images of tensile fracture surface of AA6101 T6, hexagonal pin, concave shoulder tool, at 1070 rpm, 120mm/min (E8)

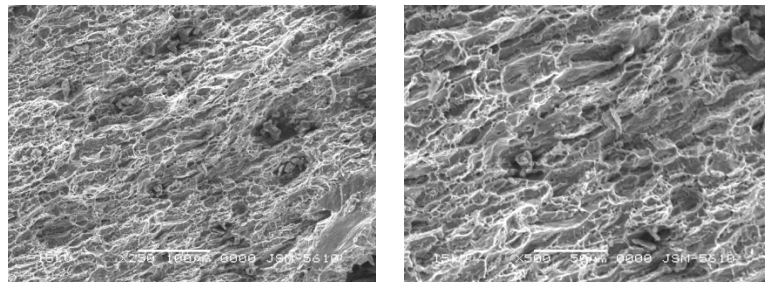
**Observation:** The fracture surface indicated the mix mode fracture of ductile and brittle behavior. The observation was carried out that there is a presence of the some cleavage and steps. There is also presence of wide and long micro cracks.

#### 4.6.4 Fractography of Tensile specimen E9



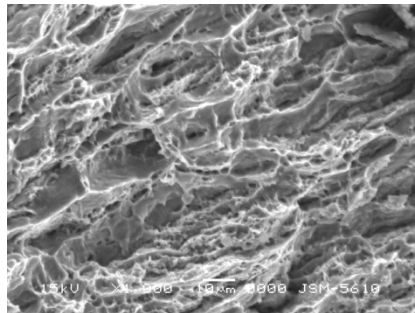
(a) 50x

(b) 100x



(c) 250x

(d) 500x



(e) 1000x

Figure 4.70: SEM images of tensile fracture surface of AA6101 T6, hexagonal pin, concave shoulder tool, at 1070 rpm, 120mm/min (E9)

**Observation:** The fracture surface reveals the mix mode failure of ductile and brittle behavior. There is presence of the elongated and equiaxed dimple in the fracture surface. There are fine micro cracks and voids are present which reveals the no time for proper agglomeration.

## 4.7 ELECTRICAL CONDUCTIVITY MEASUREMENT

The material used for welding in this section is AA6101 alloy. The primary application of this material is bus bar where electrical conductivity required to be maintained after joining. The results are mentioned in Table 4.18.

Table 4.18: Result for Electrical conductivity measurement

Experiment No	Electrical conductivity %IACS
Base Metal	56.0
E1A	52.0
E1B	52.0
E2	52.6
E3	54.0
E4	53.0
E5	53.6
E6	53.0
E7	52.4
E8	52.1
E9	52.2
E10	51.8
E11	52.8
E12	52.0

[**Note:** % IACS – International Annealed copper Standard]

From the Table 4.18 it is observed that there are little variations in the measured electrical conductivity, which indicates that the joint formed by both hexagonal pin and square pin

profiled tool are good and this difference is negligible. Hence, FSW the process of material joining can be adopted for bus bar without much loss of conductivity. Hexagonal pin tool gives better output.

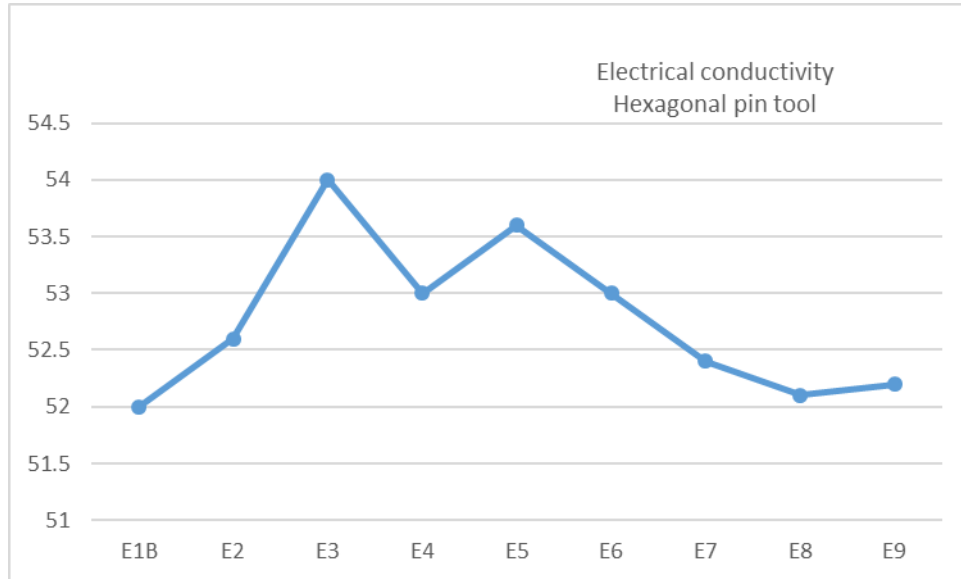


Figure 4.71: Electrical conductivity test of samples welded by Hexagonal pin tool

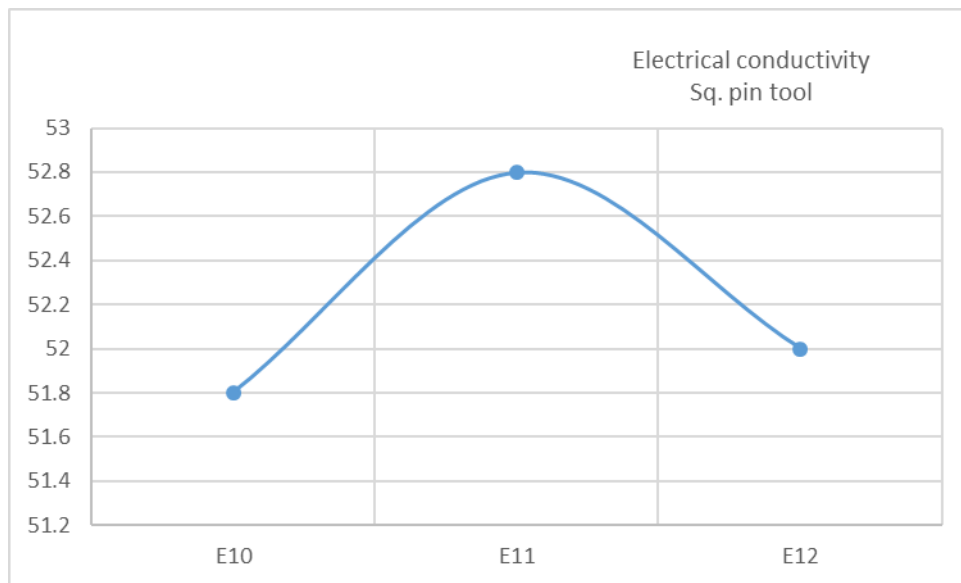


Figure 4.72: Electrical conductivity test of samples welded by Square pin tool

From figure 4.71 and 4.72, it is observed that in sample E3 and E5 conductivity is maximum compare to other samples in case of hexagonal pin tool. While sample E11 has maximum value in its group welded by square pin tool.

#### **4.8 CORROSION TEST RESULTS OF AA6101 T6 ALLOY WELDED BY HEXAGONAL PIN PROFILE**

Generally a passive oxide film can be readily formed on the surface of aluminum alloys, when exposed to air or water. However the corrosion rate could be very high due to the presence of chloride ions. Further the corrosion behavior of aluminium alloys largely depends on heterogeneity of their microstructures. In this study, cyclic polarization test was carried out on base metal and welded samples at TMAZ & HAZ regions to understand the characteristics of pitting corrosion of FSW samples in solution of 3.5%NaCl to determine corrosion parameters such as corrosion potential ( $E_{corr}$  in mV), pitting potential ( $E_{pit}$  in mV), corrosion current ( $I_{corr}$  in  $\mu A$ ) and corrosion rate (mpy) as shown in table 4.19 to 4.30. In this test, FSW samples were used as working electrode (WE), a saturated calomel electrode immersed in the salt solution was used as reference electrode (RE), and a graphite electrode was used as an auxiliary electrode (AE).

The potentiostatic polarization curves for the base alloy AA6082, AA6061 and FSW samples in 3.5%NaCl at room temperature are given in figure 4.73 to 4.85. It is shown that the corrosion behavior of base alloy AA6061 and AA6082 significantly varies from that of welded joints and the friction stir welds. The pitting potentials of corrosion tested samples (table 4.19 to 4.30) at various process parameters clearly indicated a greater corrosion resistance of weld metal than base metal. This is attributed to the precipitates present in the alloy promote matrix dissolution through selective dissolution of aluminium from the particle. These precipitate deposits are highly cathodic compared to the metallic matrix, which initiates pitting at the surrounding matrix and also enhances pit growth. During FSW process only coarser precipitates could nucleate and grow but not finer ones. This aids in formation of passive film, which remained more intact on surface of the sample. Aging produces a microstructure of uniform distribution of precipitates in aluminium matrix. This condition creates inhomogeneity on a microscopic scale. The

precipitates are noble and promote anodic dissolution of the matrix. The higher pitting corrosion resistance of the weld nugget can be attributed to the dissolution of the precipitates. Population of the precipitates is quite low compared to the other areas of the high temperature generation.

The poor pitting corrosion resistance of the weld joints is due to difference in pitting potentials across the weld region or stir nugget because of inhomogeneity of microstructures in those regions. It can be seen that the localized corrosion area of FSW depends on the welding parameters, especially tool rotation speed. At the low rotation speed, the area of anodic attack is located in the nugget region and continuously extends into the HAZ, whereas at higher rotation speeds, the corrosion area is located predominantly in the HAZ and the nugget shows predominantly cathodic reactivity. The width of the anodically-active region depends both on the rotation speed and welding speed. At a given rotation speed, the width of the reactive region decreases with increasing welding speed whereas at a given welding speed, the width of the reactive region increases with increasing rotation speed. Moreover, there is significant difference in corrosion rate as a function of welding parameters from test.

The effects of rotational speed and welding speed on corrosion behavior of all FSW samples are discussed below separately.

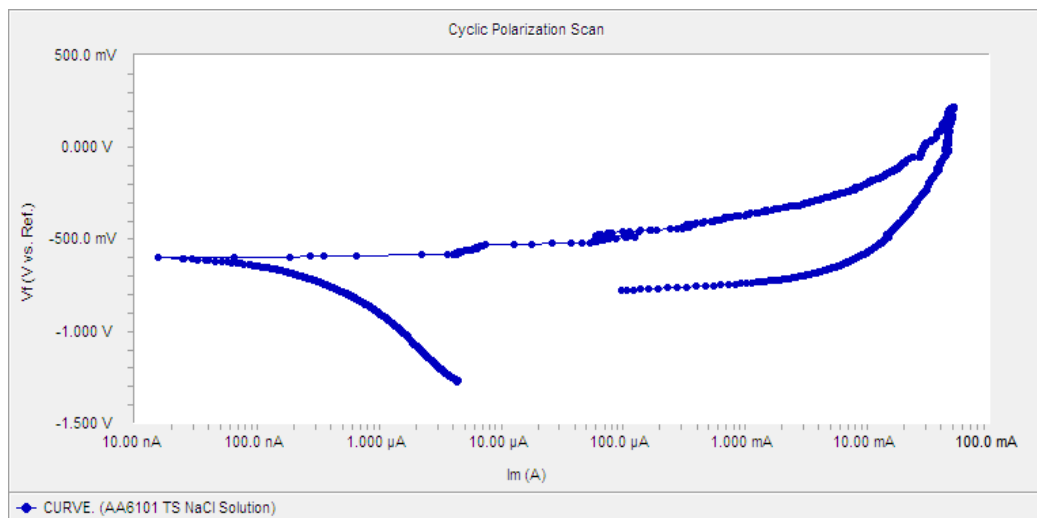


Figure 4.73: Cyclic polarization curve for base metal in 3.5% NaCl.

The cyclic polarization curve of base metal having grade AA 6101 T6 aluminum alloy was obtained by performing cyclic polarization test on given base metal in 3.5% NaCl as environment. The above obtain curve shows positive hysteresis.

Also here  $E_{pit} < E_{corr}$  which indicate that pitting will occur and damage passive film which is not repairable and it will further corroded under pitting manner.

#### 4.8.1 Cyclic polarization studies at TMAZ region with constant tool rotational speed

Table 4.19: Corrosion analysis at TMAZ region of CFSW joint using hexagonal pin tool

Sample code	Tool rotation speed RPM	Welding speed mm/min	$I_{corr}$ ( $\mu$ A)	$E_{corr}$ (mV)	$E_{pit}$ (mV)	Corrosion rate (mpy)
E1-T1	545	50	0.156	-804.0	-866.9	267.2e-3
E2-T2	545	78	1.090	-762.0	-861.9	1.877
E3-T3	545	120	0.933	-724.0	-827.9	1.704

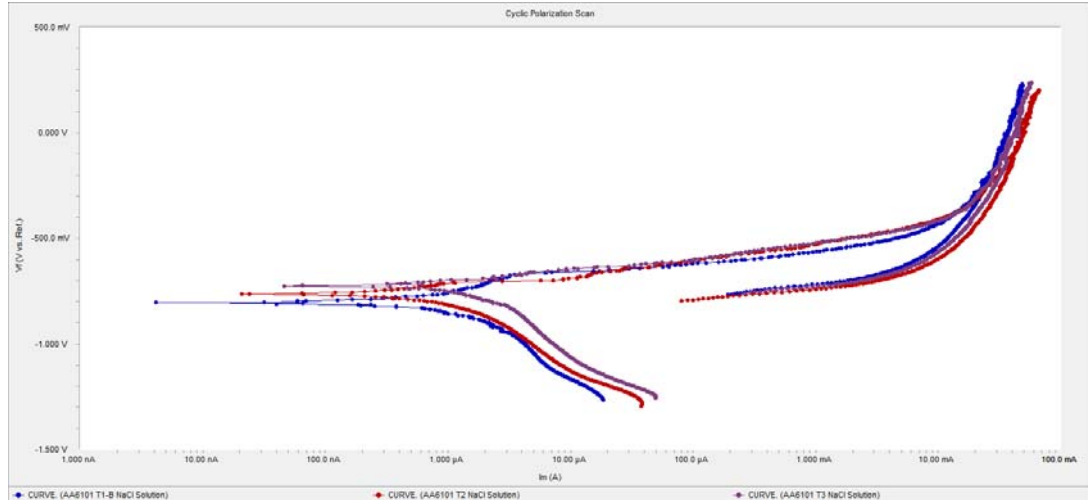


Figure 4.74: Effect of welding speed on corrosion at rotational speed of 545 rpm at TMAZ

- The cyclic polarization curve of FSW welded AA 6101 aluminum alloy at TMAZ shows positive hysteresis for different welding speeds.

- At constant rotational speed of 545 rpm, in all the samples,  $E_{pit} < E_{corr}$  which indicates that pitting will occur and damage passive film which is not repairable and it will further corrode under pitting manner.
- The corrosion rate is very low at 50 mm/min, and high at 78 and 120 mm/min welding speed.
- E1-T1 has best corrosion resistance.
- All sample show passivation after longer time of exposure to corrosion media (Figure 4.74).

Table 4.20: Corrosion analysis at TMAZ region of CFSW joint using hexagonal pin tool

Sample code	Tool rotation speed RPM	Welding speed mm/min	$I_{corr}$ ( $\mu$ A)	$E_{corr}$ (mV)	$E_{pit}$ (mV)	Corrosion rate (mpy)
E4-T4	765	50	0.639	-1.180V	-821.2	1.097
E5-T5	765	78	75.20	-710.0	-944.3	129.1
E6-T6	765	120	0.128	-723.0	-820.4	219.2e-3

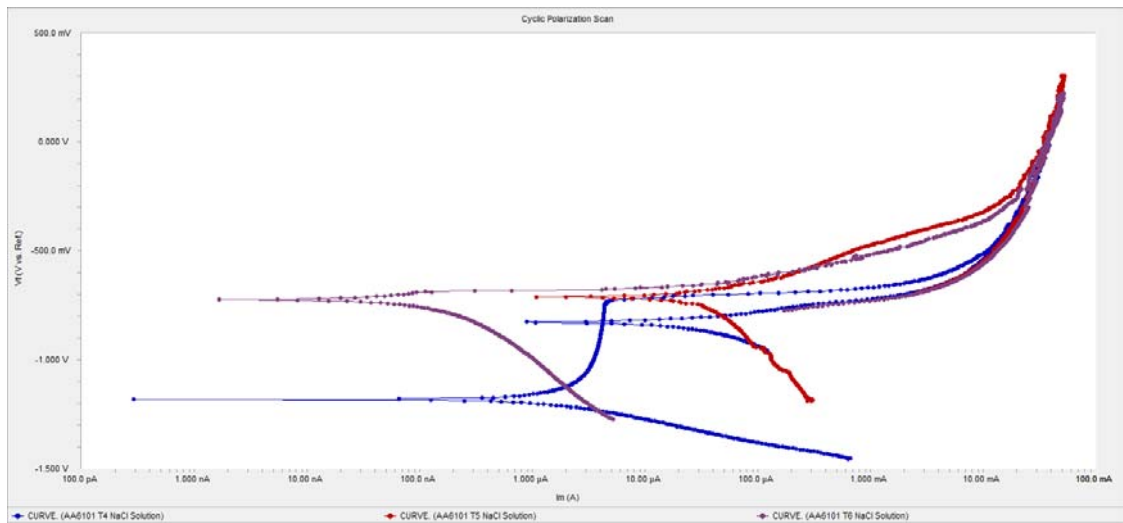


Figure 4.75: Effect of welding speed on corrosion at rotational speed of 765 rpm at TMAZ

- E4-T4 has highest active potential (-1.180V) among all.

- Also here  $E_{pit} > E_{corr}$  which indicate that pitting will occur but in passive zone and damage passive film can be repaired and it will prevent further corrosion.
- The corrosion rate is very low at 120 mm/min, at rotational speed of 765 rpm.

Table 4.21: Corrosion analysis at TMAZ region of CFSW joint using hexagonal pin tool

Sample code	Tool rotation speed RPM	Welding speed mm/min	$I_{corr}$ ( $\mu$ A)	$E_{corr}$ (mV)	$E_{pit}$ (mV)	Corrosion rate (mpy)
E7-T7	1070	50	0.0858	-767.0	-934.4	147.1e-3
E8-T8	1070	78	0.255	-737.0	-917.2	437.8e-3
E9-T9	1070	120	1.080	-768.0	-848.4	1.852

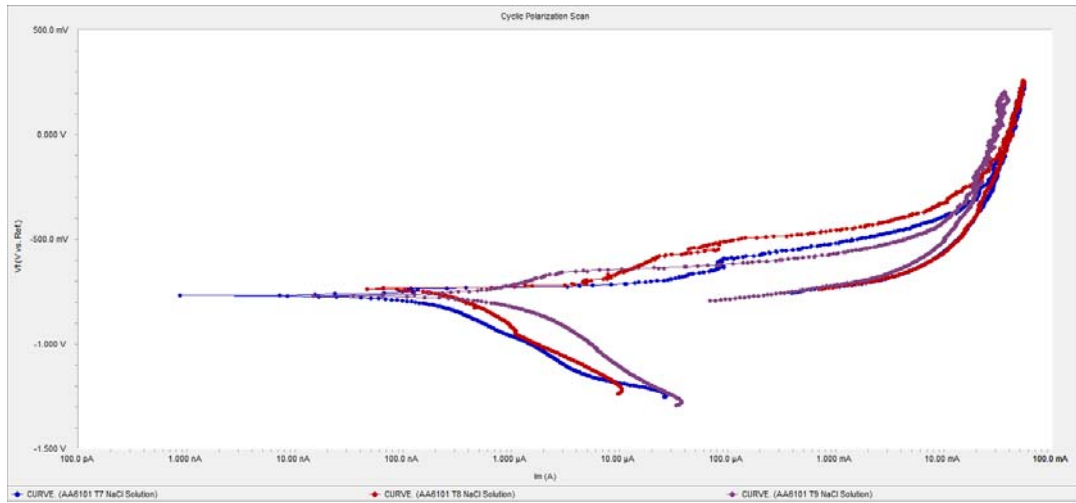


Figure 4.76: Effect of welding speed on corrosion at rotational speed of 1070 rpm at TMAZ

- All sample show passivation after longer time of exposure to corrosion media (Figure 4.76).
- The corrosion rate increases with increase in the welding speed.

#### 4.8.2 Cyclic polarization studies at HAZ region with constant tool rotational speed

Table 4.22: Corrosion analysis at HAZ region of CFSW joint using hexagonal pin tool

Sample code	Tool rotation speed RPM	Welding speed mm/min	$I_{corr}$ ( $\mu$ A)	$E_{corr}$ (mV)	$E_{pit}$ (mV)	Corrosion rate (mpy)
E1-H1	545	50	0.430	-1.040V	-838.7	737.7e-3
E2-H2	545	78	2.060	-822.0	-883.3	3.538
E3-H3	545	120	3.610	-783.0	-829.6	6.198

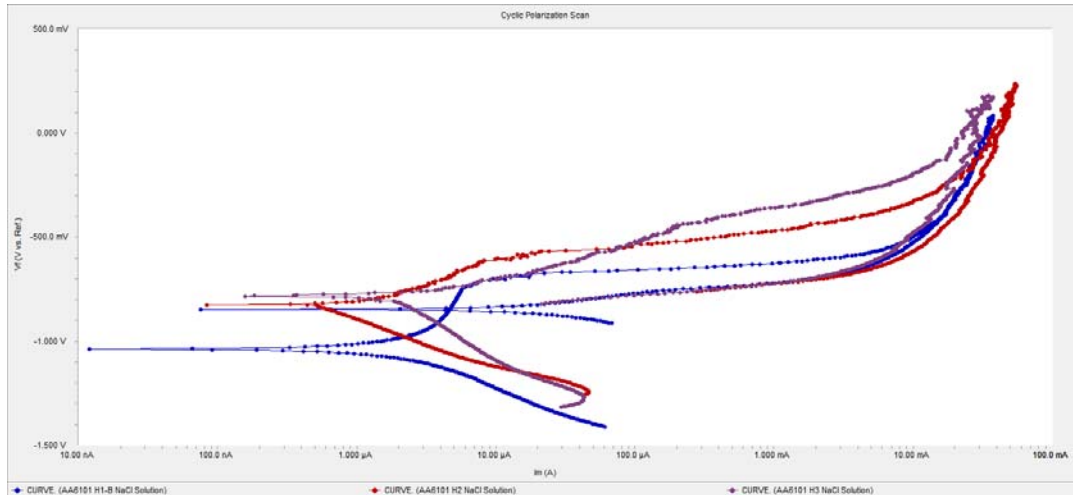


Figure 4.77: Effect of welding speed on corrosion at rotational speed of 545 rpm at HAZ

- All sample show passivation after longer time of exposure to corrosion media (Figure 4.77).
- The corrosion rate increases with increase in the welding speed in HAZ region.
- E1-H1 has highest active potential (-1.040V) among all.
- Also  $E_{pit} > E_{corr}$  which indicate that pitting will occur but in passive zone and damage passive film can be repaired and it will prevent further corrosion.

Table 4.23: Corrosion analysis at HAZ region of CFSW joint using hexagonal pin tool

Sample code	Tool rotation speed RPM	Welding speed mm/min	$I_{corr}$ ( $\mu A$ )	$E_{corr}$ (mV)	$E_{pit}$ (mV)	Corrosion rate (mpy)
E4-H4	765	50	0.461	-830.0	-931.9	790.2e-3
E5-H5	765	78	0.605	-1.010V	-865.1	1.038
E6-H6	765	120	1.300	-733.0	-813.9	2.238

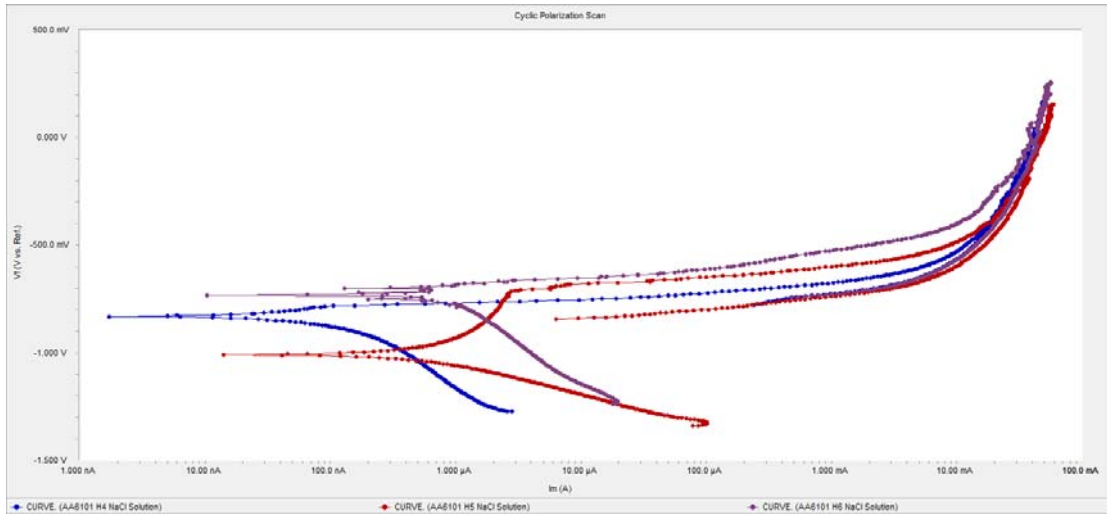


Figure 4.78: Effect of welding speed on corrosion at rotational speed of 765 rpm at HAZ

- All sample show passivation after longer time of exposure to corrosion media (Figure 4.78).
- The corrosion rate increases with increase in the welding speed.
- E5-H5 has highest active potential (-1.010V) among all.
- Also here  $E_{pit} > E_{corr}$  which indicate that pitting will occur but in passive zone and damage passive film can be repaired and it will prevent further corrosion.

Table 4.24: Corrosion analysis at HAZ region of CFSW joint using hexagonal pin tool

Sample code	Tool rotation speed RPM	Welding speed mm/min	$I_{corr}$ ( $\mu$ A)	$E_{corr}$ ( mV)	$E_{pit}$ ( mV)	Corrosion rate (mpy)
E7-H7	1070	50	0.214	-858.0	-831.1	366.4e-3
E8-H8	1070	78	0.227	-932.0	-880.6	390.0e-3
E9-H9	1070	120	0.411	-1.000V	-854.0	705.7e-3

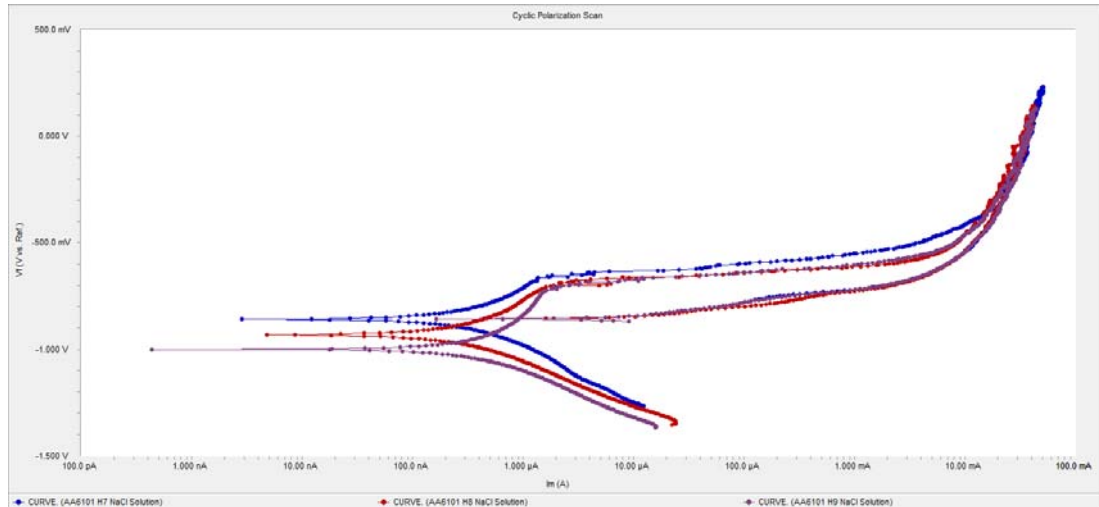


Figure 4.79: Effect of welding speed on corrosion at rotational speed of 1070 rpm at HAZ

- All sample show passivation after longer time of exposure to corrosion media (Figure 4.79).
- The corrosion rate increases with increase in the welding speed.
- E9-H9 has highest active potential (-1.000V) among all.
- In this case at all the welding speeds a similar trend of curve is observed. It has good corrosion resistance at HAZ region in all conditions at constant speed of 1070 rpm.
- $E_{pit} > E_{corr}$  which indicate that pitting will occur but in passive zone and damage passive film can be repaired and it will prevent further corrosion.

#### 4.8.3 Cyclic polarization studies at TMAZ region at constant welding speed at constant welding speed

Table 4.25: Corrosion analysis at TMAZ region of CFSW joint using hexagonal pin tool at constant welding speed 50 mm/min

Sample code	Tool rotation speed RPM	Welding speed mm/min	$I_{corr}$ ( $\mu$ A)	$E_{corr}$ (mV)	$E_{pit}$ (mV)	Corrosion rate (mpy)
E1-T1	545	50	0.156	-804.0	-866.9	267.2e-3
E4-T4	765	50	0.639	-1.180V	-821.2	1.097
E7-T7	1070	50	0.0858	-767.0	-934.4	147.1e-3

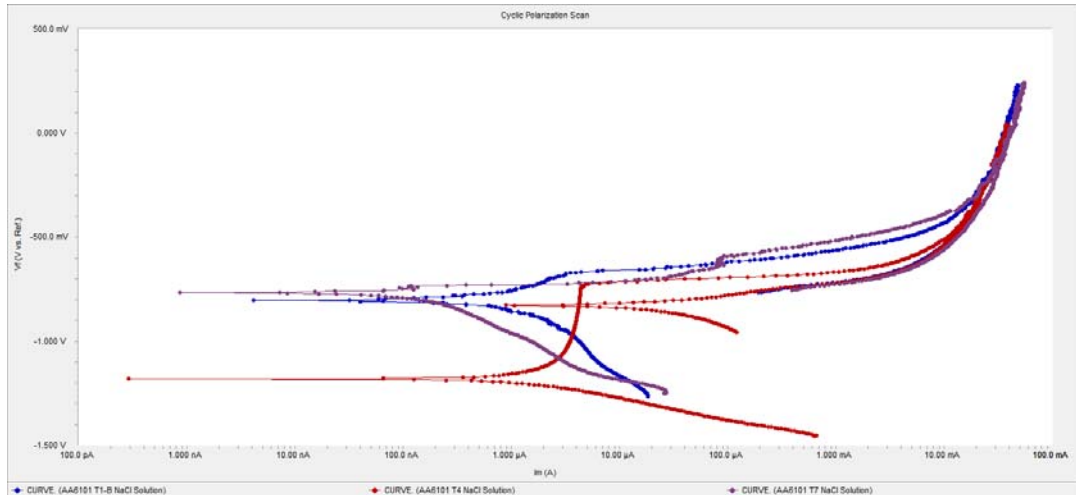


Figure 4.80: Effect of rotational speed on corrosion at 50mm/min welding speed at TMAZ

- Corrosion rate increases with increase in rotational speed and then decreases with further increase in spindle speed in TMAZ region.

Table 4.26: Corrosion analysis at TMAZ region of CFSW joint using hexagonal pin tool at constant welding speed 78 mm/min

Sample code	Tool rotation speed RPM	Welding speed mm/min	$I_{corr}$ ( $\mu A$ )	$E_{corr}$ (mV)	$E_{pit}$ (mV)	Corrosion rate (mpy)
E2-T2	545	78	1.090	-762.0	-861.9	1.877
E5-T5	765	78	75.20	-710.0	-944.3	129.1
E8-T8	1070	78	0.255	-737.0	-917.2	437.8e-3

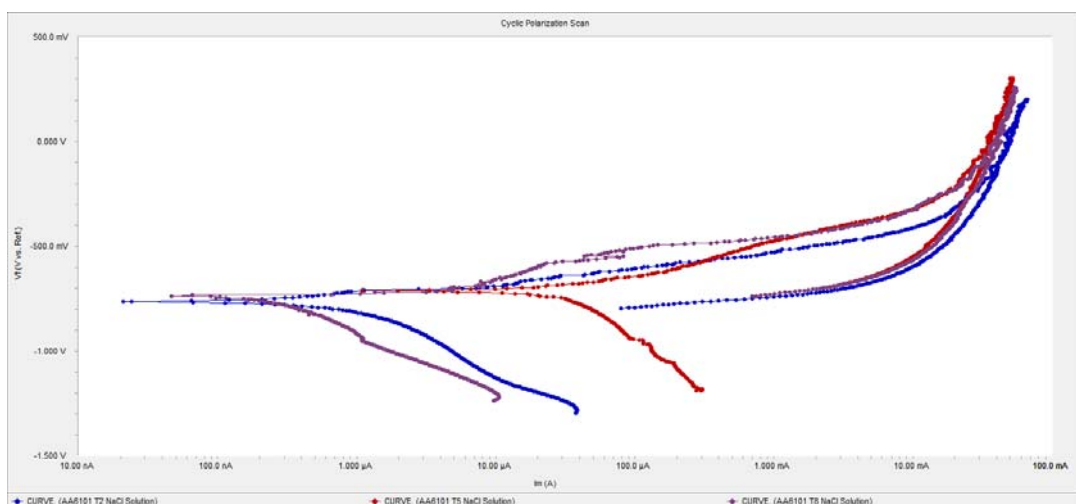


Figure 4.81: Effect of rotational speed on corrosion at 78mm/min welding speed at TMAZ

- All sample show passivation after longer time of exposure to corrosion media (Figure 4.81).
- At constant welding speed 78 mm/min  $E_{pit} < E_{corr}$  at all rotational speeds.

Table 4.27: Corrosion analysis at TMAZ region of CFSW joint using hexagonal pin tool at constant welding speed 120 mm/min

Sample code	Tool rotation speed RPM	Welding speed mm/min	$I_{corr}$ ( $\mu$ A)	$E_{corr}$ (mV)	$E_{pit}$ (mV)	Corrosion rate (mpy)
E3-T3	545	120	0.933	-724.0	-827.9	1.704
E6-T6	765	120	0.128	-723.0	-820.4	219.2e-3
E9-T9	1070	120	1.080	-768.0	-848.4	1.852

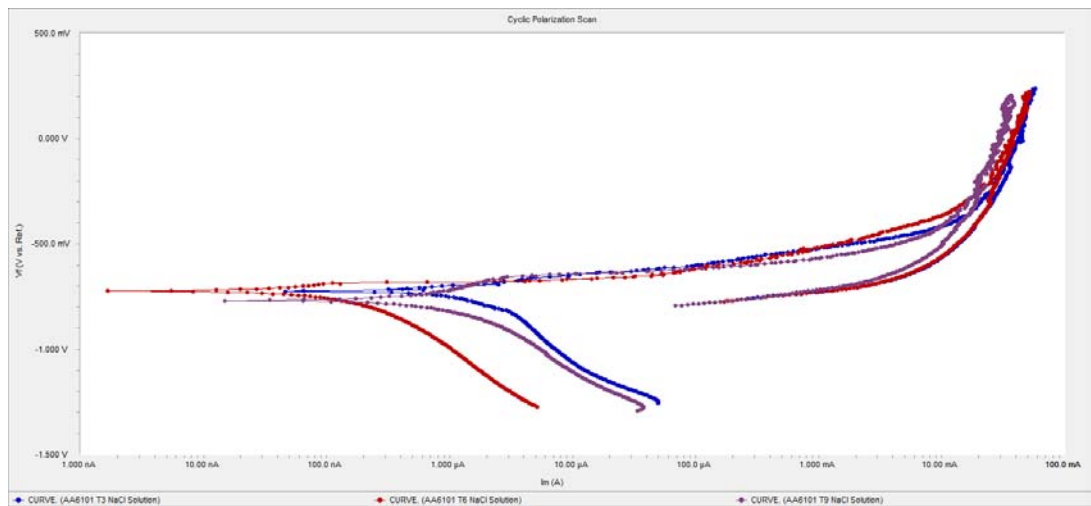


Figure 4.82: Effect of rotational speed on corrosion at 120mm/min welding speed at TMAZ

- All sample show passivation after longer time of exposure to corrosion media (Figure 4.82).
- In this case a drastic change in corrosion rate is observed. With increase in rotational speed from 545 rpm to 765 rpm corrosion rate decreased and then with further increase in speed to 1070 rpm the corrosion rate was increased, at constant welding speed of 120 mm/min.

#### 4.8.4 Cyclic polarization studies at HAZ region at constant welding speed

Table 4.28: Corrosion analysis at HAZ region of CFSW joint using hexagonal pin tool at constant welding speed 50 mm/min

Sample code	Tool rotation speed RPM	Welding speed mm/min	$I_{corr}$ ( $\mu$ A)	$E_{corr}$ (mV)	$E_{pit}$ (mV)	Corrosion rate (mpy)
E1-H1	545	50	0.430	-1.040V	-838.7	737.7e-3
E4-H4	765	50	0.461	-830.0	-931.9	790.2e-3
E7-H7	1070	50	0.214	-858.0	-831.1	366.4e-3

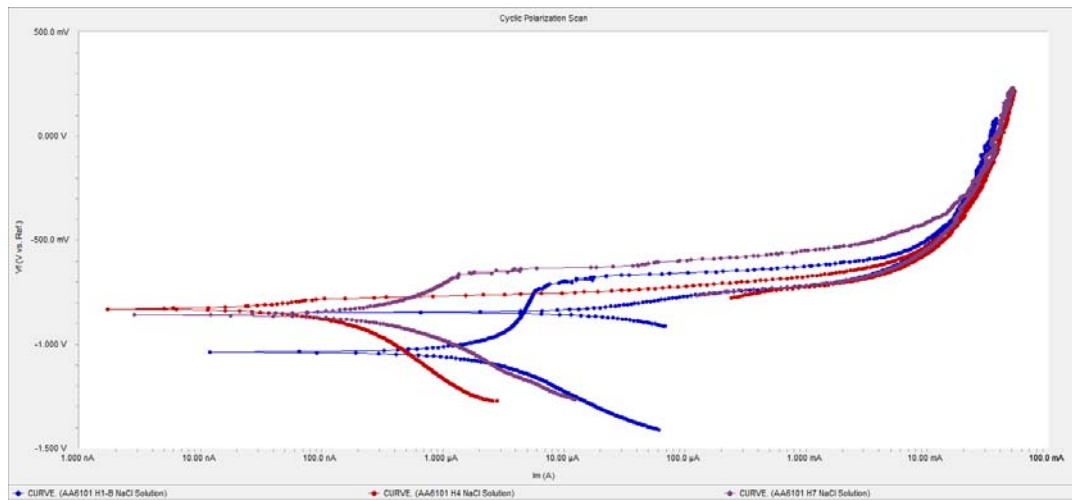


Figure 4.83: Effect of rotational speed on corrosion at 50mm/min welding speed at HAZ

- Corrosion rate increases with increase in rotational speed and then decrease with further increase in speed.

Table 4.29: Corrosion analysis at HAZ region of CFSW joint using hexagonal pin tool at constant welding speed 78 mm/min

Sample code	Tool rotation speed RPM	Welding speed mm/min	$I_{corr}$ ( $\mu$ A)	$E_{corr}$ (mV)	$E_{pit}$ (mV)	Corrosion rate (mpy)
E2-H2	545	78	2.060	-822.0	-883.3	3.538
E5-H5	765	78	0.605	-1010.0	-865.1	1.038
E8-H8	1070	78	0.227	-932.0	-880.6	390.0e-3

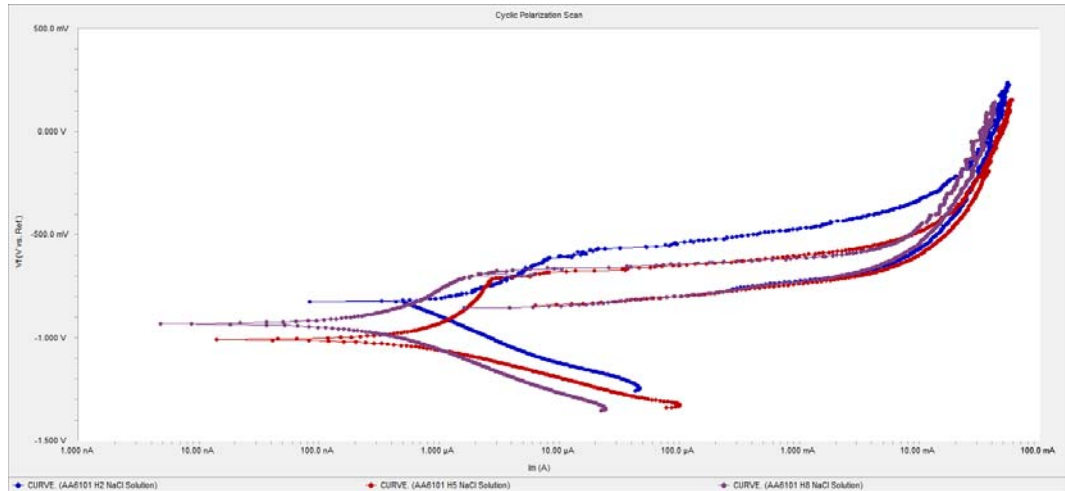


Figure 4.84: Effect of rotational speed on corrosion at 78mm/min welding speed at HAZ

- At welding speed of 78 mm/min, with increase in rotational speed, corrosion rate is decreased at HAZ region.

Table 4.30: Corrosion analysis at HAZ region of CFSW joint using hexagonal pin tool at constant welding speed 120 mm/min

Sample code	Tool rotation speed RPM	Welding speed mm/min	$I_{corr}$ ( $\mu A$ )	$E_{corr}$ (mV)	$E_{pit}$ (mV)	Corrosion rate (mpy)
E3-H3	545	120	3.610	-783.0	-829.6	6.198
E6-H6	765	120	1.300	-733.0	-813.9	2.238
E9-H9	1070	120	0.411	-1.000V	-854.0	705.7e-3

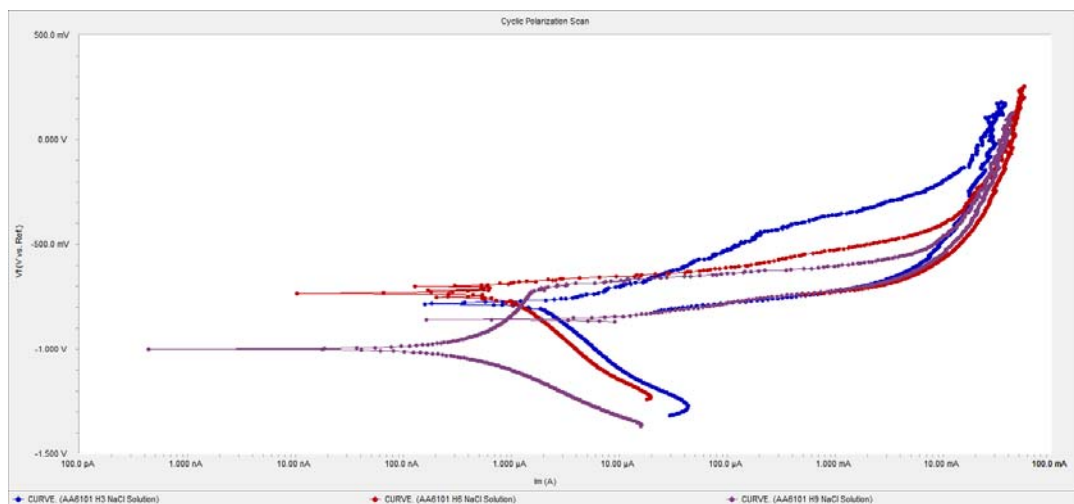


Figure 4.85: Effect of rotational speed on corrosion at 120mm/min welding speed at HAZ

- At welding speed of 120 mm/min, with increase in rotational speed, corrosion rate is decreased at HAZ region.

#### **4.8.5 Concluding remarks of cyclic polarization studies**

From the results obtained by Performing the cyclic polarization test on AA 6101 FSW welded aluminum alloy in 3.5% NaCl as environment & from the cyclic polarization curve study, it can be finally concluded that sample code E4-T4, E1-H1, E5-H5, E7-H7, E8-H8 and E9-H9 shows good pitting resistance than all other sample.

The main reason here was that the curve obtained by performing cyclic polarization test on the sample code E4-T4, E1-H1, E5-H5, E3-H3, E8-H8, & E9-H9 shows Negative hysteresis. Also here  $E_{pit} > E_{corr}$  which indicate that pitting will occur but in passive zone while rest of the sample code shows positive hysteresis which indicate that pitting will occur in active zone & damage the passive film which will not be repaired.

From the analysis it can be concluded that the corrosion resistance is increased compared to base metal; with the help of friction stir welding through property improvement taking place due to welding.

## 4.9 MICROSTRUCTURE ANALYSIS OF BFSW

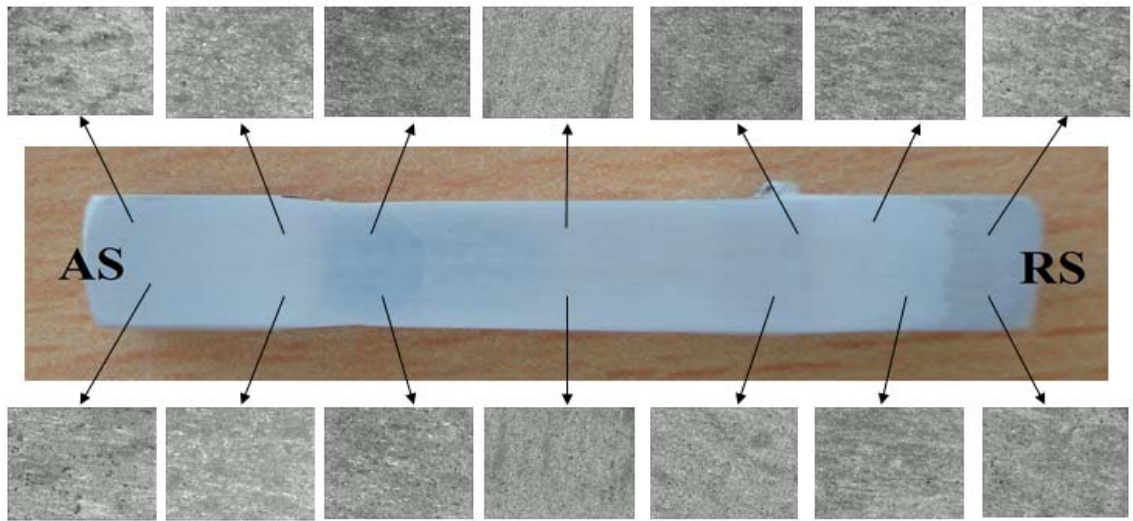


Figure 4.86: Microstructure of AA 6082 T6 alloy welded with fixed gap bobbin tool BT2 at 1000 rpm spindle speed and 24 mm/min traversing speed (At 100X magnification at different zones)

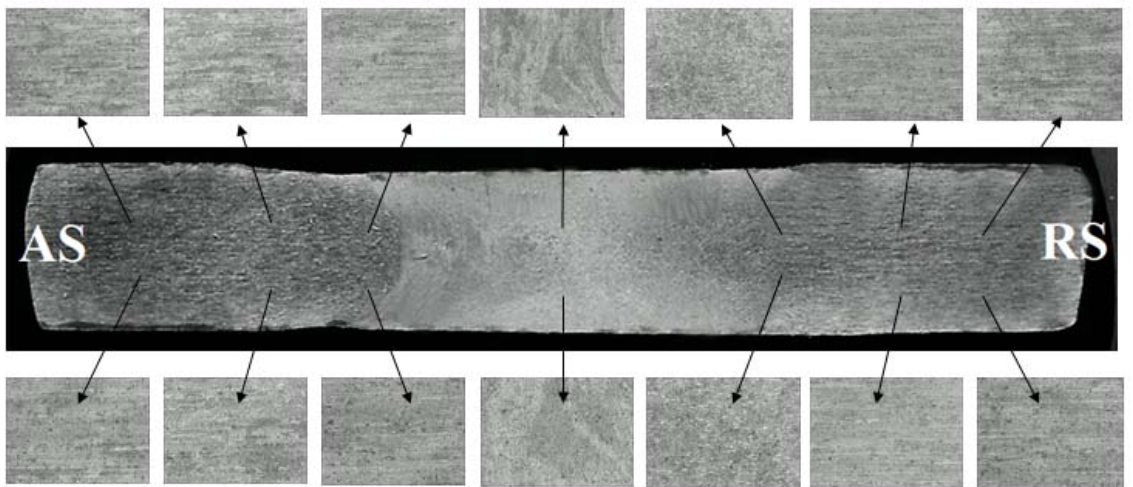


Figure 4.87: Microstructure of AA 6082 T6 alloy welded with fixed gap bobbin tool BT2 at 800 rpm spindle speed and 24 mm/min traversing speed (At 100X (upper) and 200X (lower) magnification)

Optical microstructures show the base metal contain solid solution of aluminium matrix  $Mg_2Si$  and silicon particles. HAZ contain of Al solid solution of aluminium matrix  $Mg_2Si$  and silicon particles. TMAZ contain solid solution of aluminium matrix  $Mg_2Si$  (slightly large) and silicon particles. Nugget contain fine grain solid solution of aluminium matrix  $Mg_2Si$  and fine silicon particles (Figure 4.86 and 4.88).

SEM microstructures show the soundness in the all zones of BFS Weld joint. X-Ray radiography was also carried out. There was no observation of any type of defects.



Figure 4.88: Image of sample welded by BFSW at 1000rpm and 24mm/min (as polished)

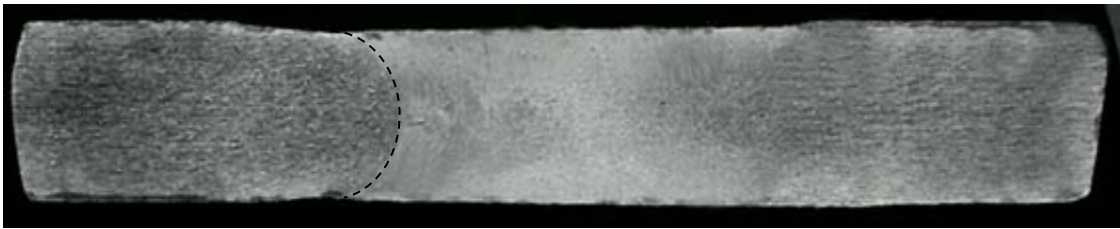


Figure 4.89: Image of sample welded by BFSW at 800rpm and 24mm/min (as polished)

Figure 4.88 and 4.89 show the macrostructure of the samples welded by square pin convex shoulder bobbin tool. It shows a clear picture of an hour glass in both the samples. The sample was polished again after etching and microanalysis, to get the clear image to distinguish the different zones.

It is also observed from the figure that curvature of the hour glass increase with the rotational speed and protruding away from the advancing side towards stir zone, as shown by dotted line.

## 4.10 IR THERMOGRAPHY RESULTS

IR Thermography was carried out online during the welding. Different process parameters were selected and IR images were stored along with the actual welding spot (situation). An attempt was made to understand the utility of thermography in this experiment. It is the new area to be discovered in depth to know quality of weld.

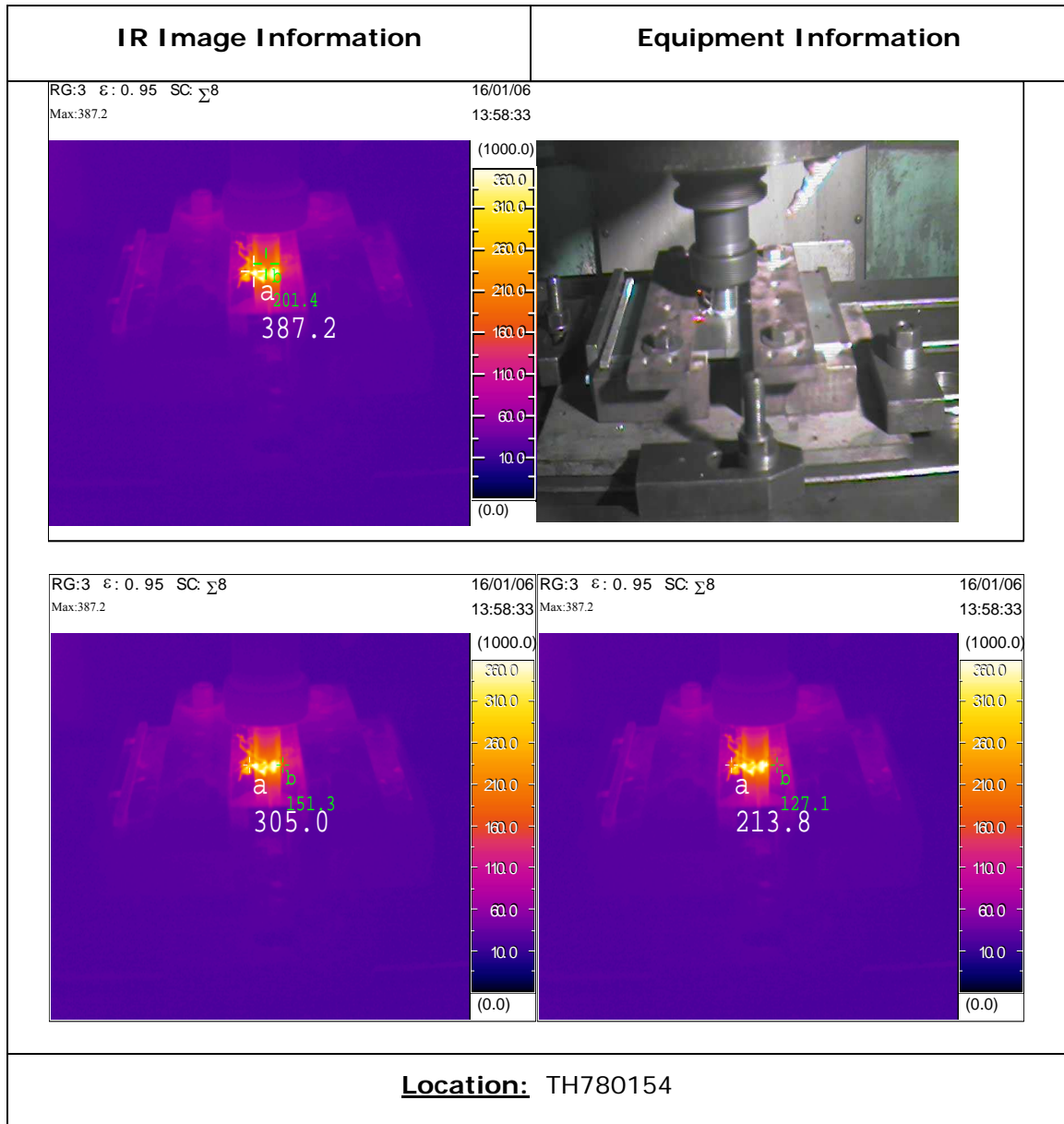


Figure 4.90: IR image for welding AA6082 T6 alloy with spindle speed 600 rpm and welding speed 48mm/min, (BT1) [RHS= Advancing side, LHS=Retreating side]

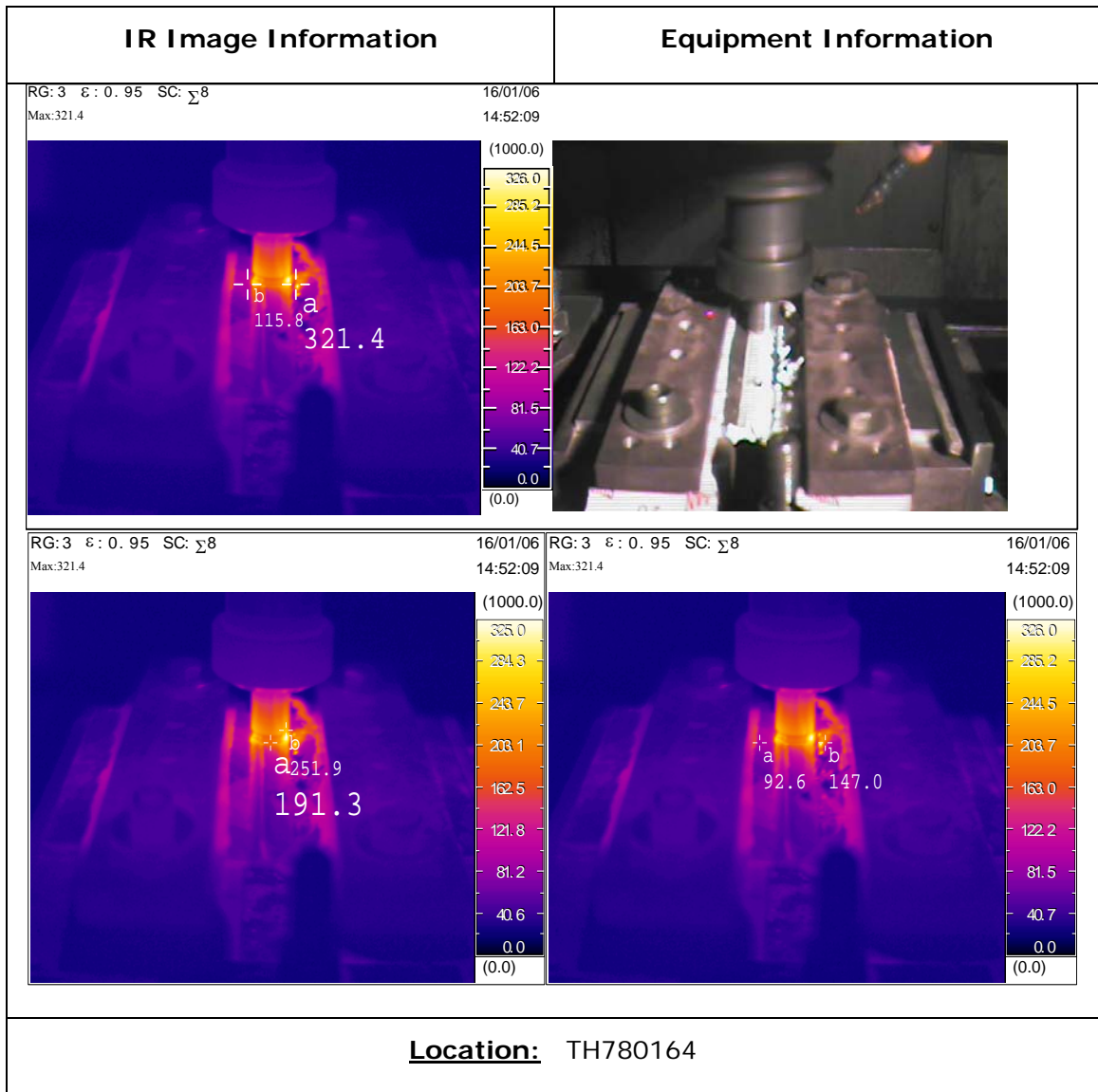


Figure 4.91: IR image for welding AA6082 T6 alloy with spindle speed 1000 rpm and welding speed 24mm/min, using BT2 tool (LHS= Advancing side, RHS=Retreating side)

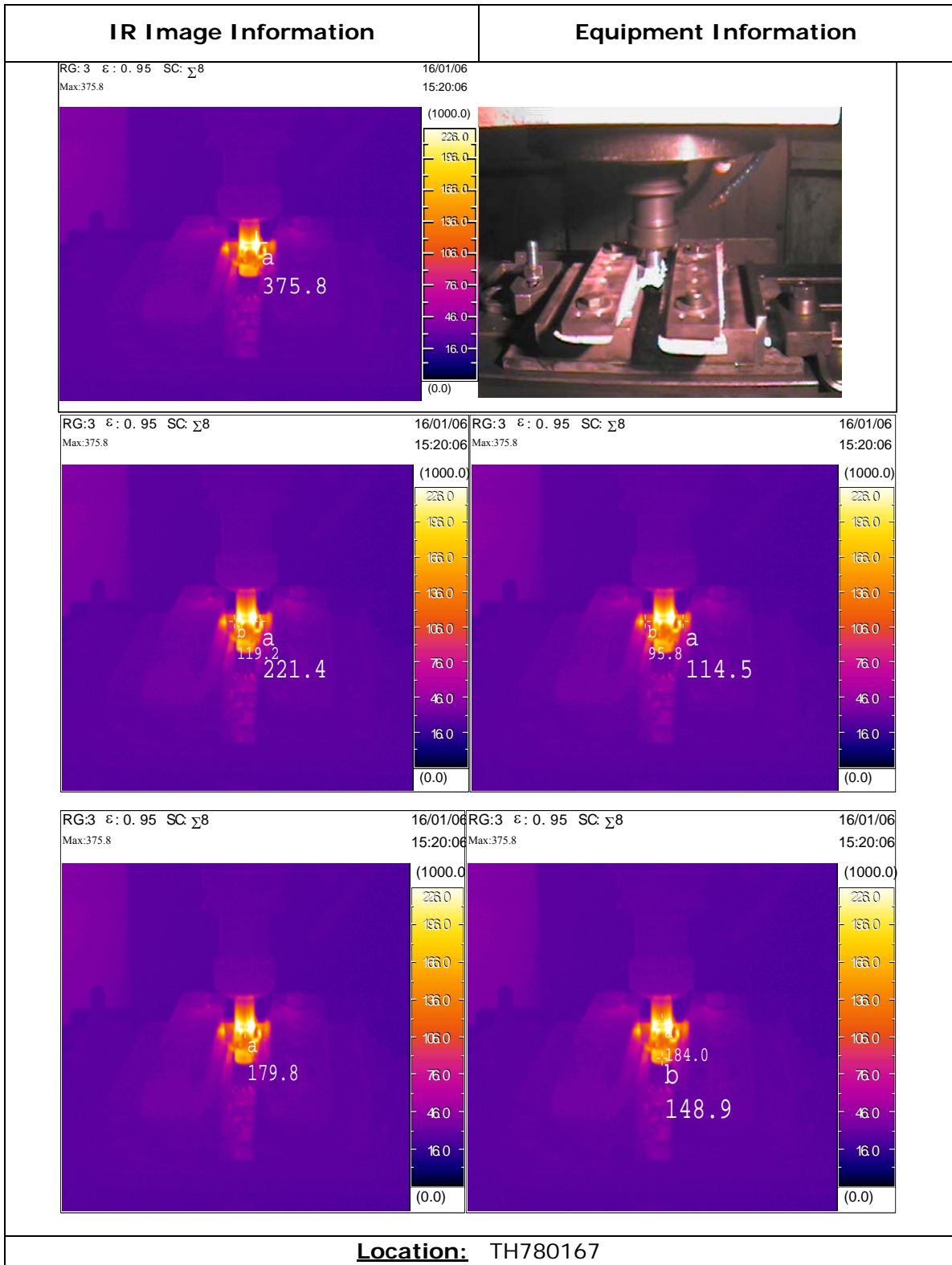


Figure 4.92: IR image for BFSW of AA6082 T6 alloy with spindle speed 800 rpm and welding speed 24mm/min, using BT2 (LHS= Advancing side, RHS=Retreating side)

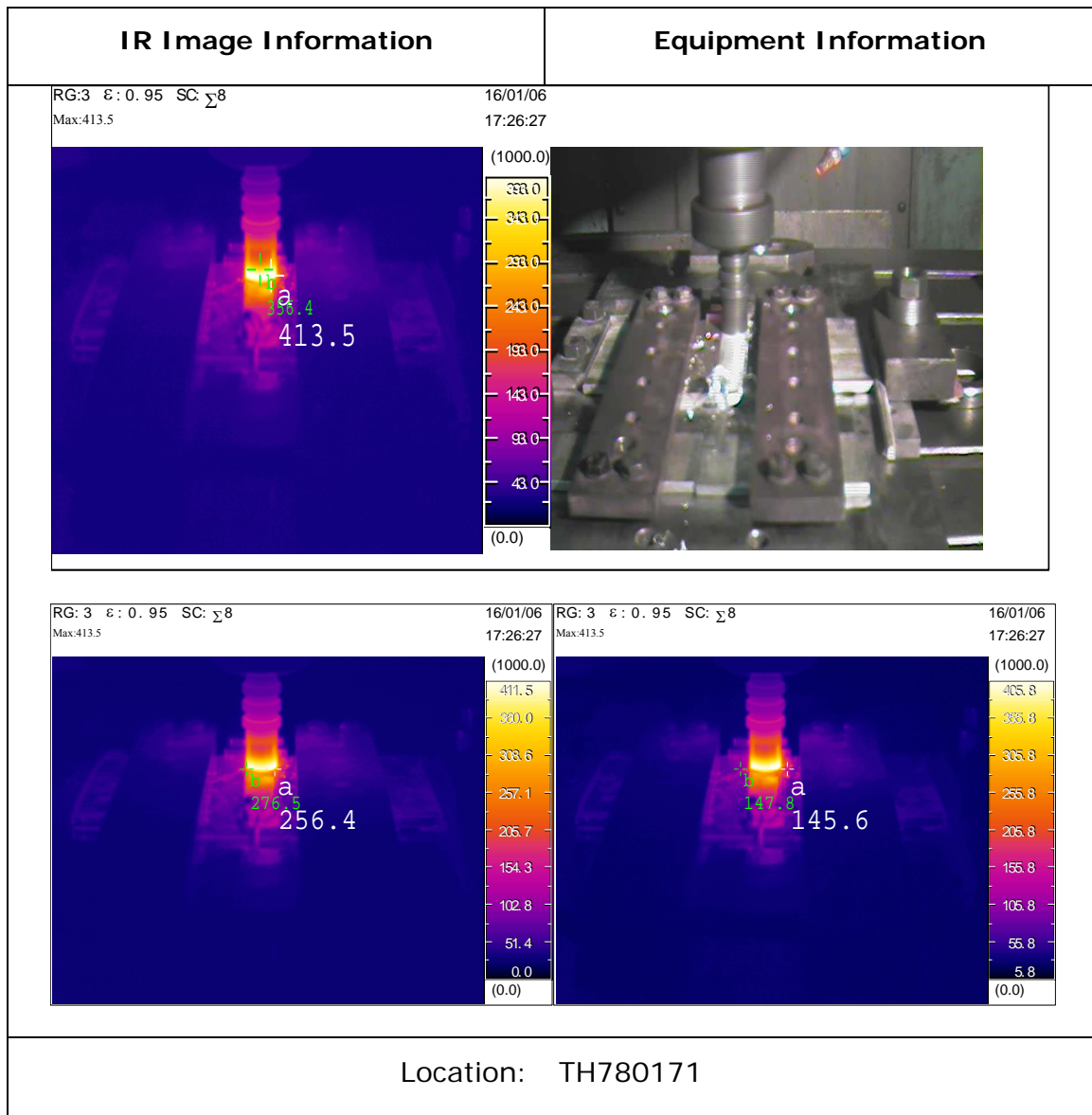


Figure 4.93: IR image for CFSW of AA6082 T6 alloy with spindle speed 1000 rpm and welding speed 48mm/min, using C4 tool (LHS= Advancing side, RHS=Retreating side)

From the IR thermography results (figure 4.90 – 4.93), it is observed that with BFSW tool, temperatures either in HAZ or TMAZ are having higher values at retreating side than advancing side. While in case of CFSW the phenomenon is giving the opposite results. The temperature zones in TMAZ are always on higher side than HAZ. Which means as tool distance increases temperature gradient is reduced. It is said that in bobbin tool; temperature is higher because of two shoulders, but it is not found always true. In

this experiment, it is observed that CFSW tool has higher temperature range than BFSW tool though the pin cross section is same in both the cases i.e. square pin (four flats).

Table 4.31 Temperature distribution zones for BFSW and CFSW weld

Fig. No.	Tool No.	Process variables	Max. temp. at tool (° C)	TMAZ (° C)		$\Delta T_{TMAZ}$ Between AS and RS (° C)	HAZ (° C)		$\Delta T_{HAZ}$ Between AS and RS (° C)
				AS	RS		AS	RS	
Fig. 4.86	BT 1	N=600 rpm f=48mm/min	387.2	151	305	154	127.1	213.8	86.7
Fig. 4.87	BT 2	N=1000 rpm f= 24mm/min	347.2	115.8	321.4	205.6	92.6	147.0	54.4
Fig. 4.88	BT 2	N=800 rpm f=24mm/min	375.8	119.2	221.4	102.2	95.8	148.9	53.1
Fig. 4.89	C4	N=1000 rpm f=48mm/min	413.5	276.5	256.4	20.1	147.8	145.6	2.2

With same bobbin tool it is found that there is little impact of process variables on temperature on advancing side, while a great difference is observed on retreating side. The temperature difference  $\Delta T$  (between AS and RS) increases with increase in tool rotational speed in TMAZ region, but in HAZ region  $\Delta T$  is nearly same. It shows that the tool rotational speed has direct impact on temperature generation and hence the quality of weld. For different tool design the values of temperatures are different in both HAZ and TMAZ regions. It means the tool design plays a vital role in temperature distribution and ultimately in development of fine grains, which will give a defect free weld.

In case of CFSW;  $\Delta T$  is not much affected. The temperatures on advancing and retreating side are more or less same in the same regions.